



Fabrication of a hydrogel-based fluidic system with integrated sensors capable of simulating physiological barriers

Author: Maria Luisa Marini



Supervisors:

prof. Matteo Cocuzza

prof. Martin Dufva

Department of Applied Science and Technology

Politecnico di Torino

Master course in Nanotechnologies for ICT

February 13, 2018

Fabrication of a hydrogel-based fluidic system with integrated sensors capable of simulating physiological barriers

Written by: Maria Luisa Marini (222127)

Home University Supervisor: External Professor DISAT, M.Sc, Ph.D., Matteo Cocuzza, Researcher III Level at IMEM-CNR.

Host University Supervisor: Associate Professor, M.Sc., Ph.D., Martin Duftva, Department of Micro- and Nanotechnology, Technical University of Denmark.

DISAT - Department of Applied Science and Technology

Politecnico di Torino
Corso Duca degli Abruzzi, 24
10129 Torino (TO)
Italia

DTU Nanotech

Technical University of Denmark
2800 Kgs. Lyngby
Denmark

Project period: 22.09.2016 - 28.04.2017

ECTS: 30

Education: Master of Science

Field: Nanotechnology

Remarks: This thesis is submitted as partial fulfillment of the requirements for graduation in the above education at the Politecnico di Torino.

Copyrights: © Maria Luisa Marini 2018

Fabrication of a hydrogel-based fluidic system with integrated sensors capable of simulating physiological barriers

Author: Maria Luisa Marini

Abstract

Hereby it is studied a specific organ-on-a-chip used to model a gastro-intestinal barrier. The gut-on-a-chip under focus is based on a gelatin hydrogel core equipped with two inner and almost parallel channels. The distance between those two channels is $\sim 370\mu m$, comparable with the physiological distance between capillaries and tissues. The use of the gel and such channel distance allow to simulate in a quite accurate way the in vivo gastro-intestinal behavior. Are going to be clarified these design choices with the comparison of other systems and methodologies at the state of art an not. Moreover, the procedures for the fabrication and characterization of this gut-on-a-chip will be showed.

The improvement of the accuracy of such organ models will allow less time-expensive and cheaper studies for the development of drugs, and, moreover, the construction of more complex systems like body-on-a-chip.

Contents

Abstract	iii
List of Figures	vi
List of Tables	viii
List of acronyms	x
1 Introduction	1
1.1 Barriers Physiology	2
1.2 In vitro barrier models	4
1.3 Methods to assess barrier integrity	4
1.4 Scope of the thesis	5
2 Overview on biological barrier models	6
2.1 Barrier models	6
2.1.1 Traditional permeability studies	6
2.1.2 Blood-Brain Barrier	10
2.1.3 Kidney-on-a-Chip	13
2.1.4 Lung-on-a-Chip	15
2.1.5 Gut-on-a-Chip	17
2.2 Methods to assess barrier integrity	18
2.2.1 Traditional permeability methods	18
2.2.2 TEER	20
3 Fabrication techniques in Tissue Engineering	22
3.1 Cell scaffold and ECM	22
3.2 Etching and Directwrite Techniques	23
3.3 CAD-based rapid prototyping methods	24
3.3.1 Fused deposition modeling (FDM)	24
3.3.2 Laser sintering	25
3.3.3 Stereolithography	26
3.3.4 Microsterolithography	26
3.3.5 Inkjet based techniques	27
3.3.6 Direct bioprinting	28
3.4 Replica Molding	30
3.5 Scaffold materials	30
3.5.1 Hydrogels	31

4	Impedance Spectroscopy	34
4.1	Ohm’s Law Method, DC versus AC TEER measurements	34
4.2	The measurement procedure and model	37
4.3	Resolving TEER from Circuit Model	40
4.4	Factors influencing TEER	40
4.5	Comparison between 2 points measurements and 4 points measurements	44
5	Materials and Methods	46
5.1	Hydrogel Preparation	46
5.2	Fluidic mold design and fabrication	48
5.3	Fluidic platform	49
5.4	Device fabrication, sensor integration and testing	57
5.5	Electrical characterization	59
5.6	Cell culture and seeding	60
5.7	Fluorescence staining	64
5.8	Imaging and analysis	64
6	Results and Discussion	66
6.1	3D printing and fabrication of the barrier fluidic device	66
6.2	Cell seeding optimization	68
6.3	System characterization	74
7	Conclusions and Outlook	82

List of Figures

1.1	The potential of organ-on-a-chip systems	1
1.2	Some of the mechanisms of transport of molecules between cytoplasm and extracellular space.	3
1.3	Summarizing scheme to explain the transcellular pathway and paracellular one.	4
1.4	The gut-on-a-chip developed during the thesis. The channels are highlighted by dyes.	5
2.1	Evolution of 3D culture models. Overview of 2D and 3D tissue culture models, including advantages and disadvantages. For HTS is meant high throughput screening	7
2.2	Scheme of a Tranwell chamber.	8
2.3	Zigmond Chamber	9
2.4	Dunn chamber	9
2.5	The blood-brain barrier in the neurovascular unit.	10
2.6	A BBB simulated on a chip	12
2.7	Scheme of a BBB simulated on a chip.	13
2.8	Bioengineered proximal tubule, part of the kidney's duct system, on a chip.	14
2.9	A lung on a chip designed to stimulate cells with mechanical stress.	16
2.10	Gut-on-a-chip.	17
2.11	FITC method used for study the diffusion in our hydrogel-based 2D model.	19
4.1	TEER measurement with chopstick electrodes	35
4.2	TEER measurement concept based on impedance spectroscopy.	36
4.3	Equivalent circuit diagram and a typical impedance spectrum.	38
4.4	Endothelial cell layer forming a barrier.	39
4.5	TEER dependence on the cell coverage.	43
4.6	Effect of TritonX-100 on the TEER measurement.	43
4.7	Comparison between 2-point probe method and 4-point probe one.	45
5.1	Hydrogel core.	46
5.2	Fluidic mold.	50
5.3	The three different designs implemented.	51
5.4	Result of the first part of the calibration.	52
5.5	Bland and Altman plot for comparing the results of the pump calibration	53
5.6	Fluidic apparatus.	54
5.7	Scheme of the velocity profile of a laminar flow.	55

5.8	Fluidic platform connected with the device during a microfluidic test.	56
5.9	Fabrication steps of the channels within the gelatin hydrogel	58
5.10	The effect of the use of the potentiostatic mode. In this case both the electrode and gelatin are burned.	60
5.11	Caco-2 image acquired with transmission microscope.	61
6.1	Quantification of the dimensions of the designed channels, 3D printed templates, and embedded channels fabricated within the gelatin/TG hydrogel.	67
6.2	Dark-field image of the hydrogel-base fluidic system integrating the needle electrodes, indicated by the yellow arrows, (Scale bar: 2 mm) and fluorescence micrograph of the cross-section of the fluidic device. It shows the the gelatin barrier separating the two channels separated, the scale bar corresponds to, $500\mu m$	67
6.3	Hydrogel-based fluidic system with detail of electrode insertion	68
6.4	An example of a not successful seeding. The cell coverage is too low.	69
6.5	Not successful seeding. In this case cells are stacked one onto each other.	69
6.6	Seeding result investigated with confocal microscopy with $8 \cdot 10^5 cells/cm^2$.	70
6.7	Comparison of seedings by rotating vs not rotating the device.	70
6.8	Seeding result investigated with confocal microscopy, comparison with flushed vs not flushed channel.	71
6.9	Seeding with $8 \cdot 10^5 cells/cm^2$. The result of this seeding could not be verified.	72
6.10	Confocal microscopy images of nuclei (blue) and F-actin (red) of the hydrogel-based fluidic system cross-section, depicting the barrier and Caco-2 cells after 24 hours of the seeding of $8 \cdot 10^5 cells/cm^2$	73
6.11	Examples of formation of mold.	73
6.12	Schemes of the four-terminal sensing.	74
6.13	Measurements in hydrogel	75
6.15	Electrode positions	76
6.14	Bode plot defining the device sensibility.	77
6.16	Effect of the electrode distance in the impedance spectra measurements.	78
6.17	Effect of the electrode distance in the phase spectra measurements. .	78
6.18	Bode plot, defying the correct assembling of the device.	80
6.19	Bode plot, follow up of dynamic and static devices for 48h.	81

List of Tables

4.1	Examples of TEER values for gastrointestinal cell lines.	44
5.1	Summary of the data acquired during the first part of the calibration. The mean of flow rates computed for each channel "ch" is reported. It is also showed the mean of the flow rates of those channels and the respective standard deviation.	51
5.2	Summary of the data acquired during the second part of the calibration. For theoretical flow is meant the flux imposed to the pumps using the regression line computed previously.	52

List of acronyms

The next list describes several acronyms that will be later used within the body of the document.

μ COB Microscale continuous optical bioprinting

AC Alternating current

BBB Blood-brain barrier

CAD Computed-aided design

CE Counter electrode

ChNC Chitinous nanocrystal

CSF Cerebrospinal fluid

DC Direct current

dChNC Deacetylated nanocrystal

DEF Diethyl fumarate

DMEM Dulbecco's Modified Eagle Medium

EBL Electron beam lithography

ECM Extra cellular matrix

FDM Fused deposition modeling

FIBL Focused ion beam lithography

FITC Fluorescein isothiocyanate

hBMVEC Microvascular endothelial cells

HRP Horseradish peroxidase

HTS High throughput screening

IMCD Inner medullary collecting duct

ITOP Integrated tissue-organ printer

LAF Laminar flow bench

LS Laser sintering
MJS Multi-phase jet solidification
MJS Multi-phase jet solidification
MSLT Micro-stereolithography
MSTL Micro-stereolithography
mTrans Transgluteminase
NC Nanocrystal
NSCs Neural stem cells
NVU Neurovascular unit
OPU Optical pickup unit
PBS Phosphatebuffered saline
PC Polycarbonate
PCL Poly(ϵ -caprolactone
PDL Poly(D-lysine)
PDLLA Poly (DL-lactic acid)
PDMS Polydimethylsiloxane
PEG Poly(ethylene glycol)
PEGTA Poly(ethylene glycol)-tetra-acrylate
PET Polyester
PGA Polyglycolic Acid
PLA Poly(l-actinic acid)
PLGA Poly(l-lactic-co-glycolic acid)
PNIPAM Poly(N-isopropylacrylamide)
PPF Poly(propylene fumarate)
PPF Propylene fumarate
PTEC Proximal Tubular Epithelial cells
PTFE Polytetrafluoroethylene
PVA Poly-vinyl alcohol
RE Reference electrode

RM Replica molding
RP Rapid prototyping
S Sensing electrode
SL Stereolithography
SLA Stereolithography
SLS Selective laser sintering
tcTEER Temperature-corrected TEER
TEER Transepithelial/transendothelial Electrical Resistance
UV Ultraviolet
WE Working electrode

Chapter 1

Introduction

Drugs require to be characterized by several studies, in the most accurate and safe way, in order to be commercialized. Therefore, clinical studies are preceded by non-clinical ones. This first step of such characterization includes *in vivo* or *in situ* intestinal perfusion studies (in an animal model) and *in vitro* permeability methods, using excised intestinal tissues or monolayers of suitable epithelial cells [1]. However, more accurate and less time-consuming *in vitro* techniques for testing and analysis are demanded, allowing an increased drug efficiency. With this purpose, organ-on-a-chip are systems developed to model human organs, recreating the physiological micro-environment using micro-fabrication techniques.

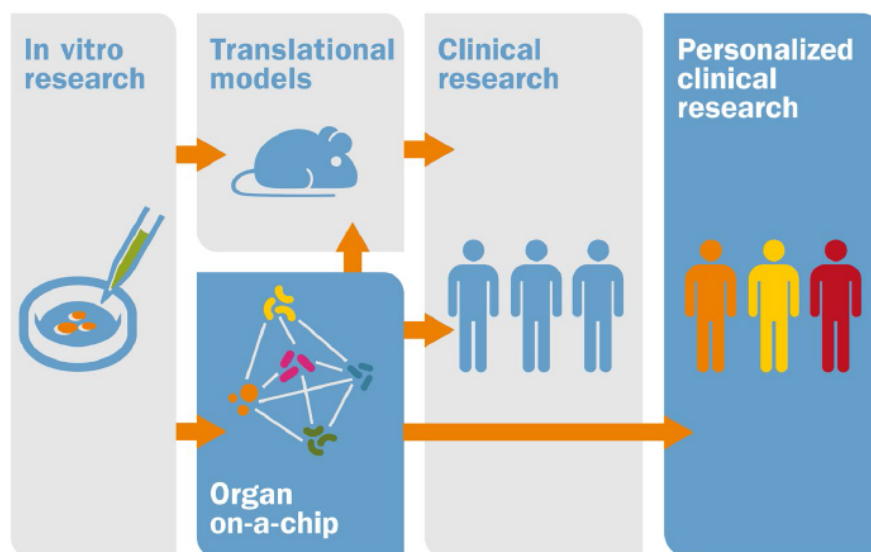


Figure 1.1: The potential of organ-on-a-chip systems. The conventional drug development pathway involves preclinical *in vitro* research, preclinical *in vivo* research in animal models, followed by various phases of clinical trial studies in humans. Organ-on-a-chip technology has the potential to make animals studies redundant prior to clinical testing. By including patient-derived stem cells, the promise of stratification takes organ-on-a-chip technology to an entirely new level of personalized clinical research [2].

The bioavailability, i.e. the proportion of a drug or nutrients which enters the circulation, depends on the quality of the function of the gastrointestinal tract bar-

rier [3]. As a matter of fact the intestinal epithelium represents the major barrier to absorption of orally administered drugs: oral bioavailability is mainly dependent on three general processes: the fraction of dose absorbed, the fraction of drug escaped from metabolism in the gut wall, and the fraction of drug escaped from hepatic metabolism [1, 4, 5]. This is why it is particularly important to study this biological barrier.

1.1 Barriers Physiology

It is possible to define a barrier as the interfaces between epithelial tissues. The gastro intestinal barrier, in particular, is composed of a single layer of columnar epithelial cells, primarily enterocytes and goblet cells, joined at their apical surfaces by tight junctions [5].

Tight junctions are intercellular connections, consisting of transmembrane proteins, cytoplasmic accessory proteins [3] and circumscribing epithelial cells forming a seal between neighboring epithelial cells. Those junctions act as a fence that separate components of the apical and basolateral domains of the epithelial plasma membrane, allowing actively or passively the passage of molecules. In transmission electron microscopy, the tight junction appears approximately 80 nm long at the apical boundary of neighboring cells [5]. Thus, those intercellular connections link adjacent cells, regulate diffusion and facilitate transport processes along the paracellular and intracellular pathways, respectively, to maintain homeostasis [6]. They actually occlude diffusion of molecules with molecular radii larger than 11 Å, restrict passage of small molecules in a charge specific manner [5] and passive substance diffusion through the paracellular spaces between epithelial cells, a process that can be compromised in diseased epithelial tissue [3]. The tight junction complex resembles a dynamic and elaborate protein signaling complex. They can be disrupted by peptide hormones, cytoskeletal perturbing agents, oxidants, Ca⁺⁺ chelators and ionophore, altering paracellular permeability. Moreover, their formation verifies in the late state of barrier formation, approximately after 20 days from the seeding. The presence of disrupting agents and the same formation of tight junctions produces noticeable variations in Transepithelial/transendothelial Electrical Resistance (TEER), making this measure a powerful instrument [5].

Cells communicate, one to the other and with the environment, in different ways and it is possible to distinguish two main categories:

- Passive process
- Active process

In passive processes, the passage of molecules through a cell membrane is regulated just by diffusion. Diffusion may verify both through transport proteins and trough cellular membrane (diffusion and facilitated diffusion respectively) as shown in Figure 1.2 A-B. The difference lays in the fact that in the diffusion process just small and non-polar molecules can pass through the membrane.

In active processes, instead, a specific external stimuli modulate the opening, or closing, of a specific transport protein. This kind of transport involves the use of energy to move specific substrates across barriers, even against the concentration

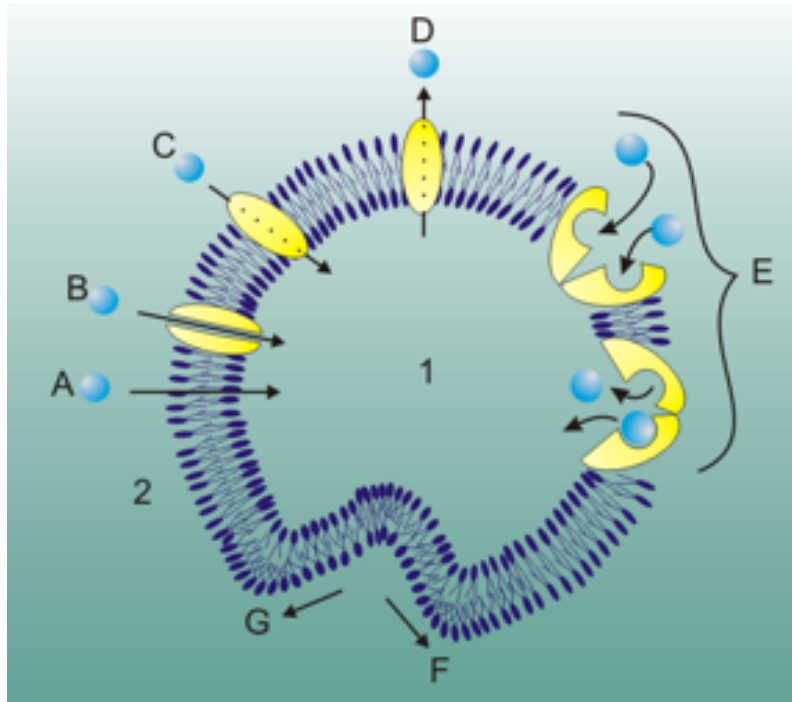


Figure 1.2: Some of the mechanisms of transport of molecules between cytoplasm (1) and extracellular space (2). Passive Transport: (A) Diffusion (B) Facilitated Diffusion (C-D) Uniport (E) Symport (F-G) Exocytosis [7].

gradient [8]. The cited mechanisms in Figure 1.2, C to G, are some of the active processes. Moreover, active transport mechanisms enable the transport of substances also through the cell bodies of epithelial cells [3].

The transport mechanisms in a barrier verify through two pathways:

- Transcellular transport pathway, which includes lipophilic, receptor-mediated, adsorptive and protein transport
- Paracellular transport pathway, that involves transport through cell junctions and the intercellular space.

Transcellular transport occurs through active processes such as ion transport by membrane ion pumps and receptor mediated endocytosis and exocytosis. The transcellular pathway of transport include transcellular diffusion, active carrier mediated transportation, and transcytosis, a way to transport macromolecules. The transcellular diffusion simply involves the movement of solutes based on a diffusion gradient moving from an area of high concentration to an area of low concentration, however, the cell membrane is a hydrophobic environment and will not allow the passive diffusion of charged or hydrophilic molecules [8].

Transport across the paracellular pathway is primarily regulated by the permeability of tight junctions at cell-to-cell contacts [8]. Paracellular transport refers to the transfer of substances across an epithelium by passing through the intercellular space between the cells. It is therefore in contrast to transcellular transport [1, 3, 4, 5]. To summarize, transcellular transport often involves energy expenditure whereas paracellular transport is unmediated and passive down a concentration gradient [10].

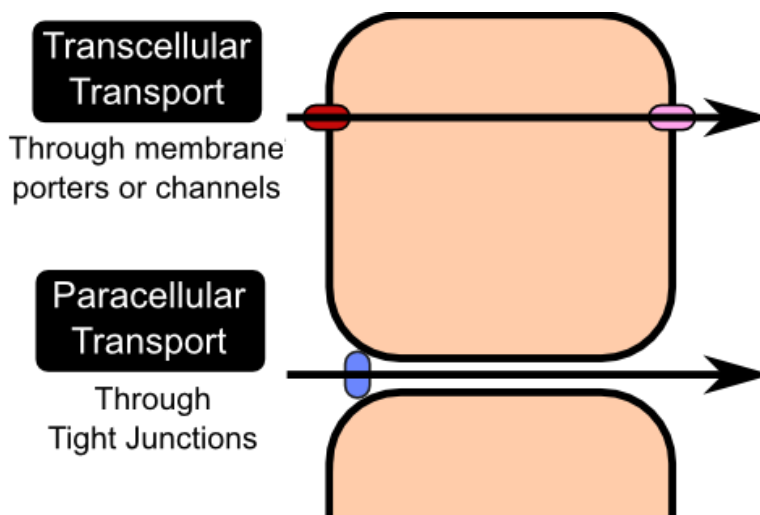


Figure 1.3: Summarizing scheme to explain the transcellular pathway and paracellular one [9].

Transport mechanisms determine the absorption of drugs. Anyway, to better investigate them in *in vitro* studies, the barrier function has to be established in order to mimic either healthy or diseased conditions in the human body[3]. This leads to the development of instruments capable of recreating the physiological micro-environment.

1.2 In vitro barrier models

Nowadays several systems analyze *in vitro* barriers in order to make permeability studies. With traditional devices are starting to be available also organs-on-a-chip. All of those systems usually consist of cell culture monolayers grown on permeable porous membranes designed to define both apical and basolateral compartments [11]. May be mentioned several models of barriers, like blood-brain barrier systems [12], intestinal mucosal [13] and lung alveolar-capillary interface [14]. However, often such systems lack of extracellular matrix [15], making critical the modeling of the tissue-tissue interfaces [16].

Transwell plates are the most commonly available systems and most of the devices on the market and techniques are well integrated with such system.

1.3 Methods to assess barrier integrity

In order to analyze barrier integrity *in vitro*, conventional techniques, based on chemicals, have been adopted. However, aside from being labor intensive and resource consuming, they require also the use of chemicals and labeling steps that may interfere with the transport process or disrupt cellular functions, therefore, the barrier integrity itself. An alternative is the measurement of TEER (previously mentioned): such technique consists on the measurement of the resistance of a certain tissue as a voltage or a current is applied on it. Further will be better analyzed and explained such technique.

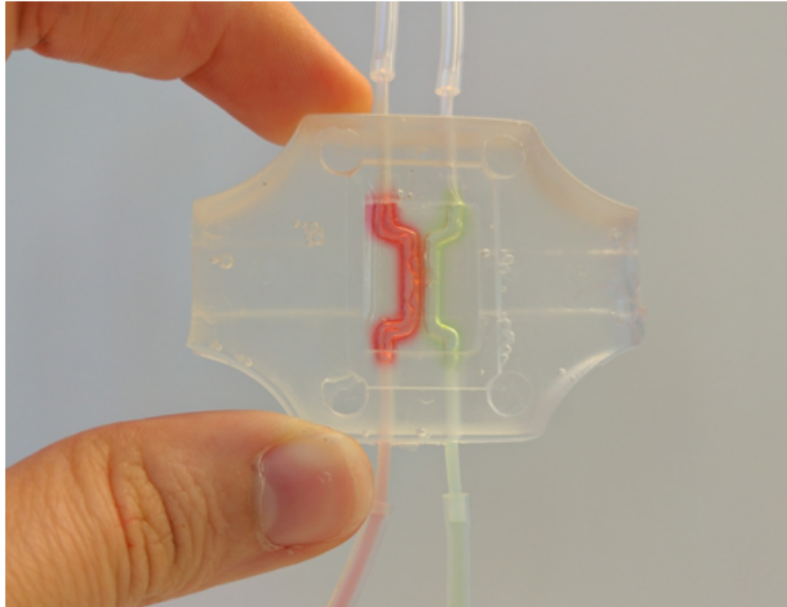


Figure 1.4: The gut-on-a-chip developed during the thesis. The channels are highlighted by dyes.

1.4 Scope of the thesis

Due to the increasing interest in developing system for studying the metabolism, transport, and oral absorption of drugs and nutrients it is here analyzed a microfluidic device recreating an intestinal barrier. Electrical and biological analysis are combined, providing a handling system that can support both diffusion analysis of drugs through an intestinal barrier, and also a TEER analysis, needed to verify the integrity of the barrier.

The systems is composed by a gelatin hydrogel (5% w/v) bulk that is provided of two internal channels. The bulk is fabricated with 3D molding technique, using a PDMS chamber. The use of 3D molding technique gave the chance to have a better control of the parameters of the device, like the distances, the position and the size of the channels. The internal channels are created thanks to sacrificial technique. Caco-2 cells were used to model the actual behavior of the intestine barrier and they were seeded in one of the two channels, performing traditional and TEER measurements in order to assess its integrity.

Therefore the thesis has the intent of investigating the fabrication, the barrier integrity measurement and, more in general, the characterization of a gastrointestinal model, that could actually represent a physiological barrier for drug diffusion studies and permeability. Unluckily there was not the chance to include microfluidics in the system, although there was the intent.

The presence of two parallel channels of almost a cm in length would allow the formation of complex chemical gradients in both directions and it is to make comparisons with capillaries using the same order of magnitude observed *in vivo* [15].

Chapter 2

Overview on biological barrier models

In this chapter are analyzed organ-on-a-chip systems to model biological barrier physiology and some of the method to verify barriers integrity. In particular, are shown systems and methods, both at the state of art and not.

2.1 Barrier models

2.1.1 Traditional permeability studies

2D cultures have been used to study physiology, pharmacology and pathology for over 50 years. Such 2D models have the advantage to be relatively simple and low in cost, and they formed the basis of our current knowledge in cellular mechanisms(Figure 2.1)[17]

To be clear, a spheroid is a heterogeneous aggregate of proliferating, quiescent and necrotic cells in culture that retain 3D architecture and tissue-specific functions. Thus, it is a 3D model that closely resembles small avascular tumors. It has been utilized as an intermediate between monolayer culture and in vivo studies for the screening of small-molecule drugs [18]. A disadvantage of most spheroid and micro engineered cultures is that they rely on ECM, with varying composition of different batches (Figure 2.1). In addition, sizes and distribution through the gel are not uniform and the luminal fluid is not easily accessible for sampling or control ([19]). Traditionally in drug and permeability studies are commonly used Transwell Plates (Figure 2.2).

They are commercially available in different shapes and sizes but they are all composed by a batch and a porous membrane inside it. Transwell permeable supports are available in three membrane materials: polycarbonate, polyester (PET), and collagen-coated polytetrafluoroethylene (PTFE). Polycarbonate Transwell inserts feature thin, translucent membranes, available in four pore sizes ranging from 0.4 μm to 8.0 μm . Most are treated for cell attachment. Moreover, the polycarbonate membrane is compatible with most organic fixatives and stains. PET Transwell-Clear inserts have microscopically transparent polyester membranes that are tissue culture-treated for cell attachment and growth [21]. Such system allows to grow easily cell cultures. Moreover there are many devices designed for such apparatuses to do TEER measurements (those measurements will be further explained in

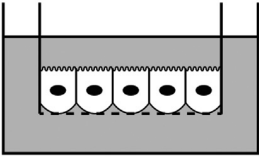
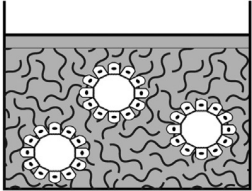
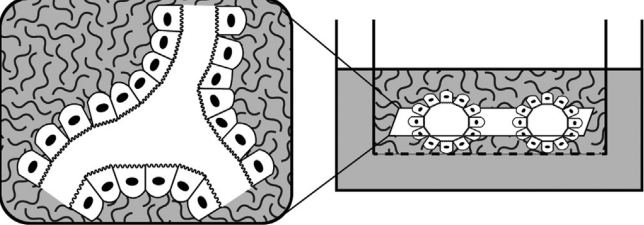
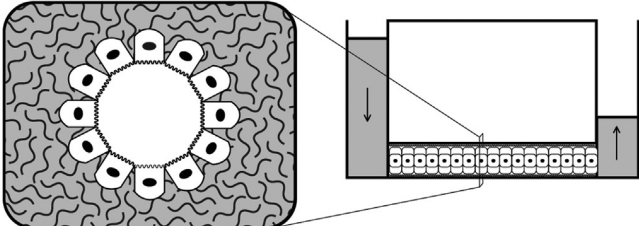
Tissue culture model	Advantages	Disadvantages
Two-dimensional monolayer 	<ul style="list-style-type: none"> • Coating with ECM • Easily accessible • Low in cost • Compatible with HTS 	<ul style="list-style-type: none"> • 2D • No transepithelial transport • No fluid shear stress • No polarization
Two-dimensional monolayer on Transwell™ insert 	<ul style="list-style-type: none"> • Easily accessible • Cell polarization • Transepithelial transport studies • Coating with ECM 	<ul style="list-style-type: none"> • 2D • No fluid shear stress
ECM-embedded spheroid 	<ul style="list-style-type: none"> • Cell polarization • ECM signaling • Compatible with HTS 	<ul style="list-style-type: none"> • No fluid shear stress • Lumen is not easily accessible • Non-uniform spheroid size • Non-uniform distribution
Bioengineered (rudimentary) organs 	<ul style="list-style-type: none"> • Cell polarization • 3D tubule formation • ECM signaling • Multiple cell types 	<ul style="list-style-type: none"> • No fluid shear stress • Lumen is not easily accessible • Low throughput • Relatively high cost
Organ-on-a-chip (microfluidic devices) 	<ul style="list-style-type: none"> • Cell polarization • ECM signaling • 3D tubule formation • Multiple cell types • Fluid shear stress • Perfusate analysis 	<ul style="list-style-type: none"> • No standardization • High-throughput screening may be possible in the future • Relatively high cost • Laborious

Figure 2.1: Evolution of 3D culture models. Overview of 2D and 3D tissue culture models, including advantages and disadvantages. For HTS is meant high throughput screening

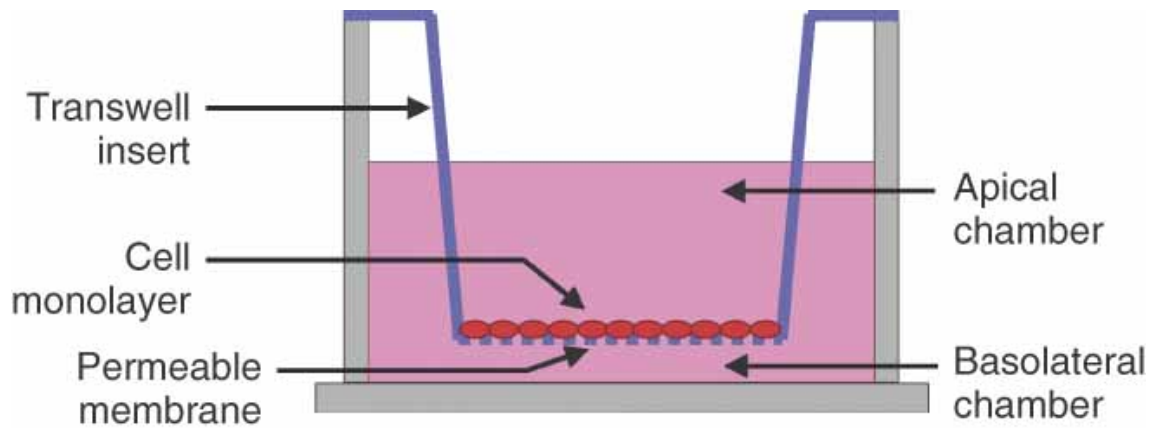


Figure 2.2: Scheme of a Transwell chamber [20].

chapter 4). The drawback of this design is the difference with the physiological morphology.

Boyden Chamber is the precursor of such system and was mostly used for our understanding of chemotaxis. In 1962, Stephen Boyden developed this gradient-generating method that consists in placing a chemoattractant solution in the lower compartment of a culture well; another culture well with a porous membrane bottom is seeded with cells, and placed in the lower compartment causing the chemoattractant contained in there to diffuse across the membrane into the upper compartment. The cells seeded on the top side of the membrane are affected by the resulting gradient, that induces them to migrate through the transmembrane holes to the lower compartment. As the Transwell plates, the advantages of the Boyden Chamber are that it is easy to use, readily elicits chemotactic responses from cells, and provides a quantitative measure of the level of transmembrane migration induced by chemotaxis. However the presence of the membrane makes it difficult to visualize cells. This characteristic, in combination with the inability to control and quantify the gradient, precludes the correlation of observed cell responses with specific gradient characteristics [22].

In 1977, Sally Zigmond developed a device for characterizing the migration of individual neutrophils in response to well defined gradients of various chemotactic factors. The Zigmond Chamber was the first to allow direct visualization of cell behavior in the presence of a biomolecule gradient. The device consists of two parallel channels etched into a glass slide. A glass ridge lies between the etched channels and is below the top surface of the slide. A glass coverslip covers the etched channels forming a thin gap between the coverslip and the glass ridge and it comes along as support for cell seeding. Changes in cell growth, differentiation, or migration of individual cells can be viewed with a microscope in the glass ridge region. A schematic example can be seen in Figure 2.3. The geometry and precise dimensions of the Zigmond Chamber produce a gradient that is reproducible, mathematically predictable, and can be indirectly estimated using fluorimetric dyes [22].

Another traditional system is the Dunn Chamber, designed in 1991 by Graham Dunn. This chamber is actually very similar to the Zigmond Chamber (Figure 2.4) but it is characterized by a concentric arrangement of the source and sink chambers. The rings that can be filled with the appropriate solutions prior to affixing the glass

coverslip seeded with cells. When the coverslip is inverted and clamped, it seals both chambers and eliminates the air-liquid interfaces that contribute to evaporative losses [22].

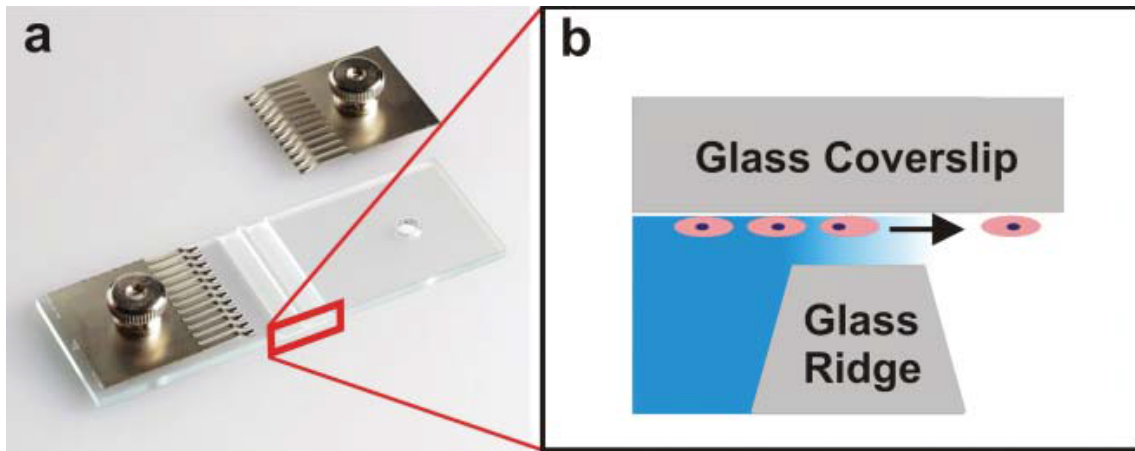


Figure 2.3: Zigmond Chamber. (a) Actual device. (b) Cross-section schematic of the device showing migrating cells on the inverted coverslip [22].

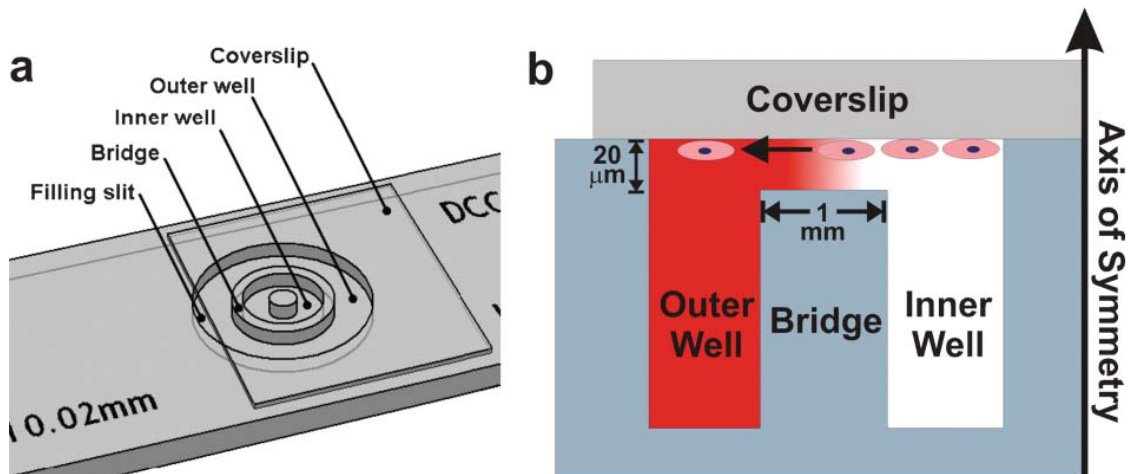


Figure 2.4: (a) Scheme of Dunn chamber. (b) A gradient forms in the 20 μm gap between the cell-seeded inverted coverslip and the glass bridge. Cell responses can be directly visualized in the bridge region [22].

However, more reliable devices, that could in addition accelerate pharmaceutical developments are needed. Indeed, one of the major lacks of systems like spheroid, organoid and engineered cultures, showed in Figure 2.1, are that they are not exposed to fluid shear stress and poorly reassemble the physiological environment [17]. Organs-on-a-chip are devices with more degrees of freedom with respect to traditional devices. An organ-on-a-chip is a microfluidic devices that allow 3D cultures of living cells thanks to the perfusion of channels on a micro scale. Due to the channels micrometer size, fluid flow in microfluidic systems is exclusively laminar: turbulence

is minimal or absent. They are capable of replicating several physiological conditions, allowing to better analyze the parameters the influence the expression of one phenotype or another: shear stresses, superficial and mechanical structures, designs and degree of vascularization are some examples. Those systems give space to interesting developments, leading to the determination of predictive end points in vitro thanks to the combination of high-throughput organ-on-chips with established analysis techniques. The current golden standard to study transepithelial transport of drugs and their metabolites via influx and efflux transporters is to culture epithelial cells on semi-permeable membrane supports[17]. In the following are listed a few examples of strategies at the state of the art to study barrier using organs-on-a-chip.

2.1.2 Blood-Brain Barrier

There are several studies and microfluidic devices designed in order to study the blood-brain barrier (BBB). The BBB is metabolic and biochemical barrier provided by the neurovascular unit (NVU), showed in Figure 2.5. This complex biological structure acts as a restrictive membrane from blood to the cerebrospinal liquid: it selectively permeates essential compounds, such as selected sugar, amino acids, electrolytes, and water [23]. The BBB is made primarily of three different cell types, i.e. with endothelial cells lined by pericytes and astrocytes, [24] forming the communicating module known as the neurovascular unit (NVU) [25]. The NVU is used to examine the role of the BBB and the blood-cerebrospinal fluid (CSF) barrier in modulating chemical body-brain interactions and assess the effect of a wide range of chemicals, drugs, and xenobiotics on the brain.

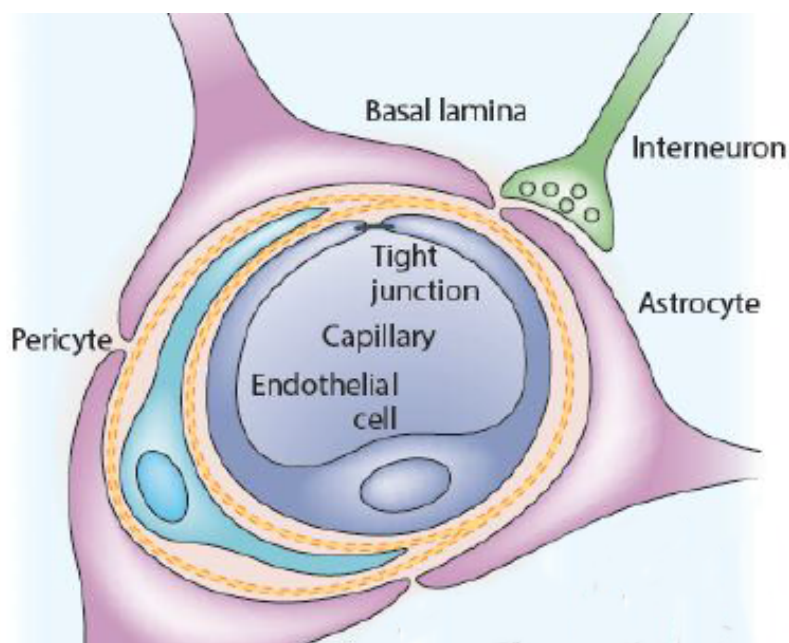


Figure 2.5: The blood-brain barrier (BBB) in the neurovascular unit (NVU) [26].

Several are the solutions developed, controlling firstly the sustaining structure pore size, pore arrangement, and porosity, but also the TEER measurement apparatus, the fluid shear stress and the extra cellular matrix (ECM). In some cases

endothelial cells and astrocytes are respectively cultured on the luminal and abluminal sides of the enclosed porous membrane together to form the neurovascular unit [27].

One of such developed device consists of polydimethylsiloxane (PDMS) parts with two channels -2 mm (luminal) or 5 mm (abluminal) wide, 200 μm deep- that are separated by a porous polycarbonate (PC) membrane (10 μm thick, 0.4 μm pores). The PDMS parts are sandwiched between two glass slides with sputtered thin-film silver chloride (AgCl) electrodes in a four-point sensing structure to measure TEER at near-direct current (DC) conditions. Mouse endothelial cell line (b.End3) were exploited and co-cultured with a murine astrocytic cell line (C8D1A) on the opposite side of the membrane, which was coated with fibronectin, an ECM protein. Both channels were perfused at 2.6 $\mu\text{l}/\text{min}$, that corresponds to a shear on the endothelial cells of approximately 2 mPa, which is low compared to the physiologically found shear of 0.3-2 Pa in brain capillaries [28, 29]. The small height-to-width ratio ensured a mostly uniform shear stress across the channel width.

Another solution consists of a PDMS part with channel imprints on a glass-bottomed well plate. An acrylic well plate with reservoirs for culture medium was glued to the top of the device. In the PDMS there are an endothelial channel and a brain channel (both 50 μm high) and an array of small perpendicular side channels (5 μm high) connecting the two main channels. The channels were filled with a collagen I gel and then replaced again by cell culturing medium in the endothelial chambers, resulting in a thin collagen gel on the walls. RBE4 rat endothelial cells were seeded in the device and allowed to attach to both the top and bottom surface [30].

An example of 3D model of brain vasculature was reported in 2015 by Kim et al shown in Figure 2.6 [31]. Their device is comprised of tubes in a collagen I gel (235-360 μm diameter), resulting from pouring collagen I around microneedles in a 3D printed frame to which fluidic connectors can be coupled.

After the microneedles were removed, the resulting tubes were coated with fibronectin. Endothelial cells from the bEnd.3 mouse cell line were cultured in these tubes to replicate the BBB.

Brown et al. published on the NVU chip in 2015, which is shown in Figure 2.7 [32]. Their chip consists of three PDMS layers: a vascular chamber with inlet channels (100 μm high and 6.2 mm wide), a brain chamber (4.75 mm x and 6.2 mm x 500 μm) and a layer with brain perfusion channels (several parallel channels, 100 μm high). The vascular and brain chambers are separated by a PC membrane (0.2 μm pores). Primary human brain-derived microvascular endothelial cells (hBMVEC) were cultured on the membrane in the vascular chamber, which was held upside down and under a constant flow of 2 $\mu\text{l}/\text{min}$. This corresponds to a shear stress of 2 mPa, which is also low compared to the physiologically found shear of 0.3-2 Pa in capillaries. After 12 days the device was flipped right-side up and pericytes and astrocytes were loaded in the brain chamber. After two days of culture under flow, the brain chamber was filled with a collagen I matrix with suspended human induced pluripotent stem cell (hiPSC)-derived neurons. The gel was allowed to set for 2 hours and subsequently the device was perfused for three days before testing the BBB. The cells remained viable up to 21 days, as was shown with live/dead staining resulting in more than 80% of cell viability.

In 2016, Walter et al. published about their barrier-on-a-chip device [33]. Their

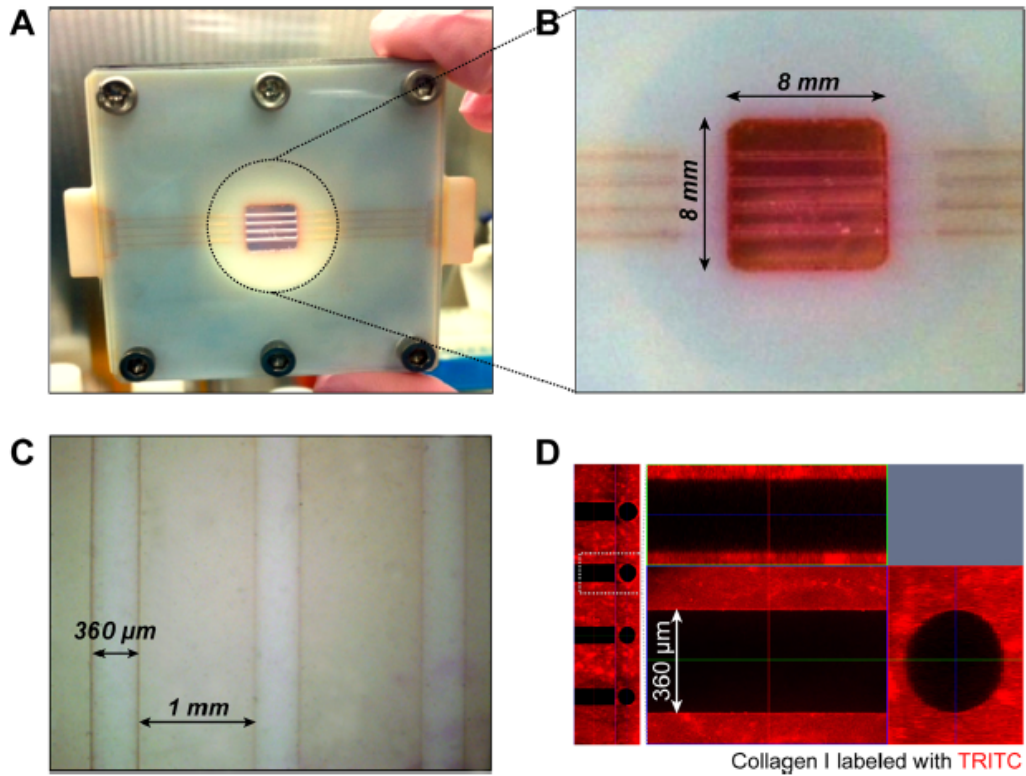


Figure 2.6: A BBB simulated on a chip (a) Photograph of our brain microvasculature system after fabrication. (b) Enlarged view of collagen microchannels. (c) Microscopic image showing multiple collagen microchannels. (d) Confocal fluorescence micrographs (z-stacked and orthogonal views) presenting fidelity of collagen microchannels [31].

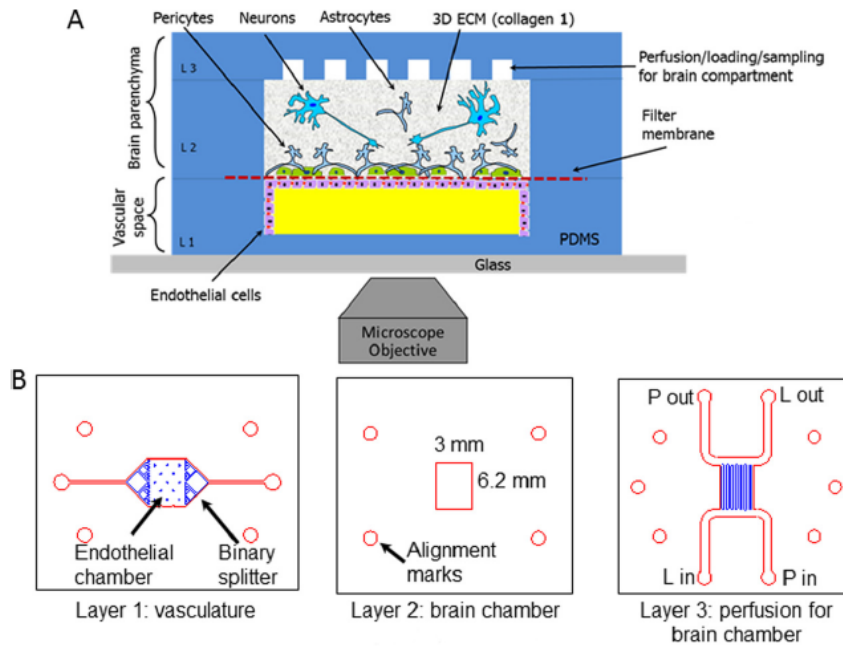


Figure 2.7: Scheme of a BBB simulated on a chip [32].

device was used to recreate the BBB, of which the results are summarized here, as well as intestinal and lung epithelial barriers. Their device consists of two PDMS parts with channels (both $200\ \mu\text{m}$ wide and $200\ \mu\text{m}$ high), that are separated by a porous PET membrane ($23\ \mu\text{m}$ thick, $0.45\ \mu\text{m}$ pores), fixated with a silicone sealant. The PDMS parts are sandwiched between two glass slides with sputter-coated $25\ \text{nm}$ thick transparent gold electrodes and fixated with a silicon sealant. Moreover, the two PDMS blocks with reservoirs are plasma-bonded to the top glass slide. One of the channels was defined "blood channel" and it was coated with collagen I, while the compartment representing the brain was coated with collagen IV. Two different cell models were used: hCMEC/D3 cells and primary rat endothelial cells co-cultured with primary astrocytes and pericytes. The endothelial cells were cultured on top of the membrane in the top channel. If present, the pericytes were cultured on the bottom of the membrane and the astrocytes on the bottom of the bottom channel. The cells were maintained under static conditions for 3 days, after which a peristaltic pump provided dynamic culture conditions at low shear stress. The electrodes are positioned in a four-point probe sensing configuration to measure TEER at near-DC conditions.

Despite the remarkable interest, there are still challenges ahead for developing BBB-on-chip models that can become widely available for BBB-related research applications. One of them is to arrive at commonly accepted standards for quantitative evaluation of the functionality of a BBB-on-chip model [26].

2.1.3 Kidney-on-a-Chip

The kidney contains more than 10 renal cell types, which are highly organized in a 3D network surrounded by ECM and complex vasculature [34]. The functional unit of the kidney is the nephron, which is intricate in geometry and function. The three main components of a nephron are: the glomerulus, proximal convoluted tubule,

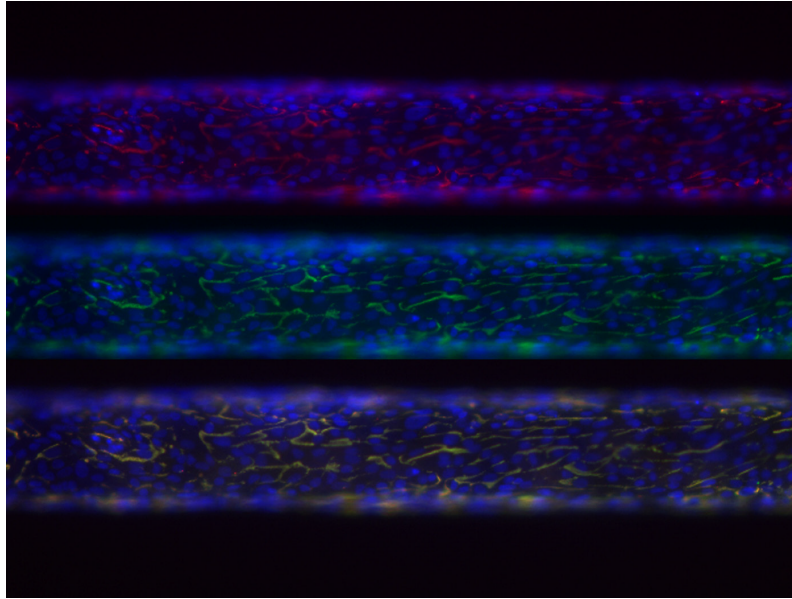


Figure 2.8: Bioengineered proximal tubule, part of the kidney’s duct system, on a chip [43].

and loop of Henle [35]. Their aim is to perform the full filtration and reabsorption of the urine. Kidney toxicity is one of the most frequent adverse events reported during drug development [36]. Exogenous drugs and toxins are often cleared via filtration and reabsorption mechanisms in the kidney, making it susceptible to drug-induced aberrations [17]. Moreover, a high fraction of cardiac output directed to the kidneys increasing the renal exposure to potential drug-induced toxicity [37].

Proximal Tubular Epithelial cells (PTEC) *in vivo* are subject to continuous luminal fluid shear stress and a trans-epithelial osmotic gradient. *In vivo*, accurate values of shear stress on tubules are lacking because urinary flow decreases along the proximal tubule as a result of tubular reabsorption. In humans, the shear stress is estimated to vary between 0.7 dyne/cm^2 and 1.2 dyne/cm^2 .

Microfluidic devices are promising for studying drug-induced toxicity and drug interaction studies [38, 39, 40, 41]. It has been shown that cells, primary rat inner medullary collecting duct (IMCD) cells for example, if they are cultured on fibronectin-coated membranes and exposed to fluid shear stress of 1 dyne/cm^2 , renal epithelial polarization improves. In addition, also a reorganization of the cytoskeleton was stimulated and a relocalization of transmembrane proteins, which was restricted under fluid shear stress to narrow areas where cells interact [17, 42]. Similar results were obtained when primary human kidney proximal tubule cells were cultured on collagen IV-coated membranes in the same microfluidic device and fluid shear stress was adjusted to 0.2 /cm^2 [40]. While tight junction protein ZO1 was expressed under both static and fluidic conditions, fluid shear stress increased cell height by 2-fold, the expression of other specific transmembrane proteins was restricted and significant increase in the amount of ciliated cells was observed [17]. Kidney-on-a-chip devices improve the physiological relevance of culture conditions, allowing evaluation of disease processes that develop within 4-6 weeks, the time-frame in which the recapitulated tissue remains viable [40].

Recent work was done using PDMS microfluidic channels with a porous mem-

brane substrate to culture and analyze renal cells of the tubule.[44] Primary rat IMCD cells were cultured inside the microfluidic channels with an applied fluidic shear stress, to simulate an *in vivo* tubular environment. Under these microfluidic conditions the cultured cells demonstrated enhanced cell polarization, cytoskeletal reorganization, and molecular transport by hormonal stimulation in comparison to the same cell type cultured statically. More recently, sub-micron topography control and flow-induced shear stress were investigated, using cells from the human renal proximal tubule cell line HK-2, to gauge their influence on cell functions such as alignment, migration, differentiation and phenotypic expression [45]. The results of this second Kidney-on-a-chip generally supported those of the other chip in the creation of a more physiologically-representative *in vitro* model of kidney tissue by eliciting better cell alignment and influencing tight cell junction formation.

2.1.4 Lung-on-a-Chip

Lung is a dynamic organ and continuously subjected to a variety of physical forces, therefore represents one of the most challenging organs to model. Simplifying the system as much as possible to the elementary tissue unit, the alveoli, the lung can be represented by a layer of epithelial and endothelial cells. In particular the interfaces in play are: epithelial-endothelial one, epithelium-air and endothelium-blood ones [46]. The gas exchange at alveolar structures occurs across the air-blood barrier of the lung [47, 48].

One of the systems to simulate such barrier consists of two PDMS chambers separated by a thin polyester membrane with 400 nm pores. The upper chamber corresponds to airway lumen and lower chamber relates to basal compartment of airway epithelium, respectively. Fluid and solid mechanical stresses play a key role in alveolar with significantly different environmental features compared to airways. This system included two compartments: an alveolar chamber and an actuation channel. These two compartments are separated by a PDMS membrane to create both cyclic stretch and fluid mechanical stresses. The alveolar chamber provides a robust microenvironment for alveolar epithelial cells culture, while the actuation channel easily interfaces with a syringe pump to control the breathing profile. They demonstrated that alveolar epithelial cells exposed to combination of solid mechanical and surface-tension stresses (cyclic propagation of air-liquid interface and wall stretch) shows significant morphological differences compared to cells exposed solely to cyclic stretch. Flexibility and permeability of the membranes to mimic alveolar-capillary interface are tremendously facilitated to reproduce their key structural, functional, and mechanical properties. These PDMS membranes are flexible substrate without the porous duo to keep sealing to meet the need of providing breathing mechanical movement [27].

Another similar strategy addressed to model the human alveolar epithelial cells and human pulmonary microvascular endothelial was achieved by culturing cells were on opposite sides of the intervening membrane coated with ECM (fibronectin or collagen) [49]. Introducing air into the upper epithelial compartment can create an air-liquid interface to precisely mimic the alveolar air space. The compartmentalized channels are benefit to manipulate fluid flow, as well as independently delivery nutrients to the epithelium and endothelium. Mechanical strain as it was said above demonstrated to enhanced epithelial and endothelial cells absorption of nanopar-

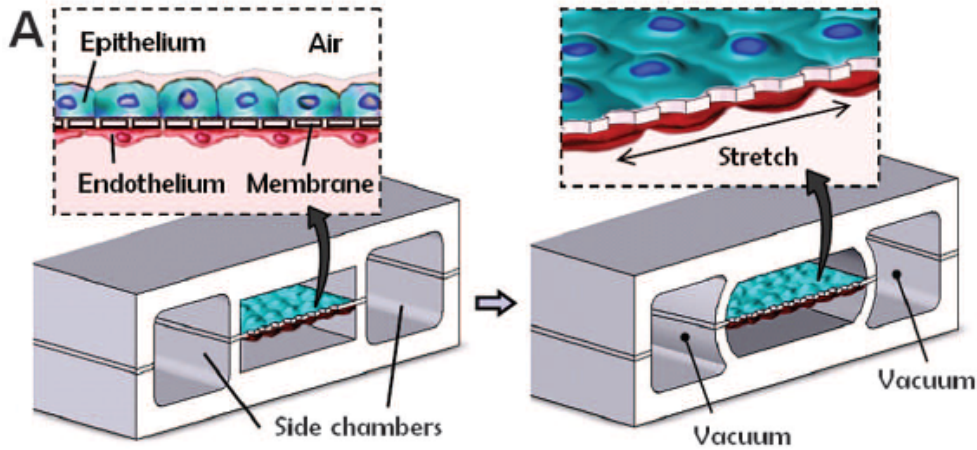


Figure 2.9: A lung on a chip designed to stimulate cells with mechanical stress [56].

ticulates and stimulates their transport across the alveolar-capillary interface into the underlying microvascular channel. This bioinspired microdevice, simultaneously reconstituting mechanically active and tissue-tissue interfaces critical to lung function, may act as a surrogate for in vivo models and potentially allowing for drug screening and toxicology applications [49].

More recently, primary adult human lung tissue has been cultured in 3D environments, which leads to self-assembly of the tissue into a variety of forms that partially reflect the structure of the lung [50, 51]. The generation of human "bronchospheres", 3D spheres derived from primary human bronchiolar epithelial cells grown in a 3D matrix, is a fairly recent innovation in the field [51]. This method involves isolating basal stem cells from mouse or human epithelial tissue. When these cells are embedded in a 3D ECM gel, spherical clonal colonies form after a short time in culture. These initial experiments provided a platform to conduct functional experiments in human tissue to show that human basal stem cells are able to self-renew and give rise to proximal secretory and ciliated cells [51].

To obtain the sophisticated matrix of lung tissue characteristics the process of recellularization of acellular natural tissue scaffolds is used [52]. This process will provide gas exchange, mechanical properties and growth of endothelial and epithelial cells, overcoming difficulties of scaffold preparation [53, 54, 52]. This method is based on decellularization of the native lung as a suitable bio-scaffold. As a matter of fact, cell contents and DNA of the organ remain and consequently the 3D structure of the matrix is retained. The Wyss Institute at Harvard, for instance, have fabricated a lung-on-a-chip, which is mainly made of microfluidic channels, with a porous PDMS membrane on which alveolar epithelial and vascular endothelial cells are grown on either side of the membrane. Research on lung-on-a-chip indeed provides biomimetic microsystems that assist to assess the fundamental function of the lungs, especially the alveolar-capillary interface [55].

In addition to studies on natural based scaffolds, as an appropriate cultivation substrate for pulmonary cell growth, other investigations focused on artificial or synthetic based (polymeric) scaffolds. Culture of murine and human lung epithelial cells on Poly (DL-lactic acid) (PDLA) scaffolds have been studied by Lin et al.

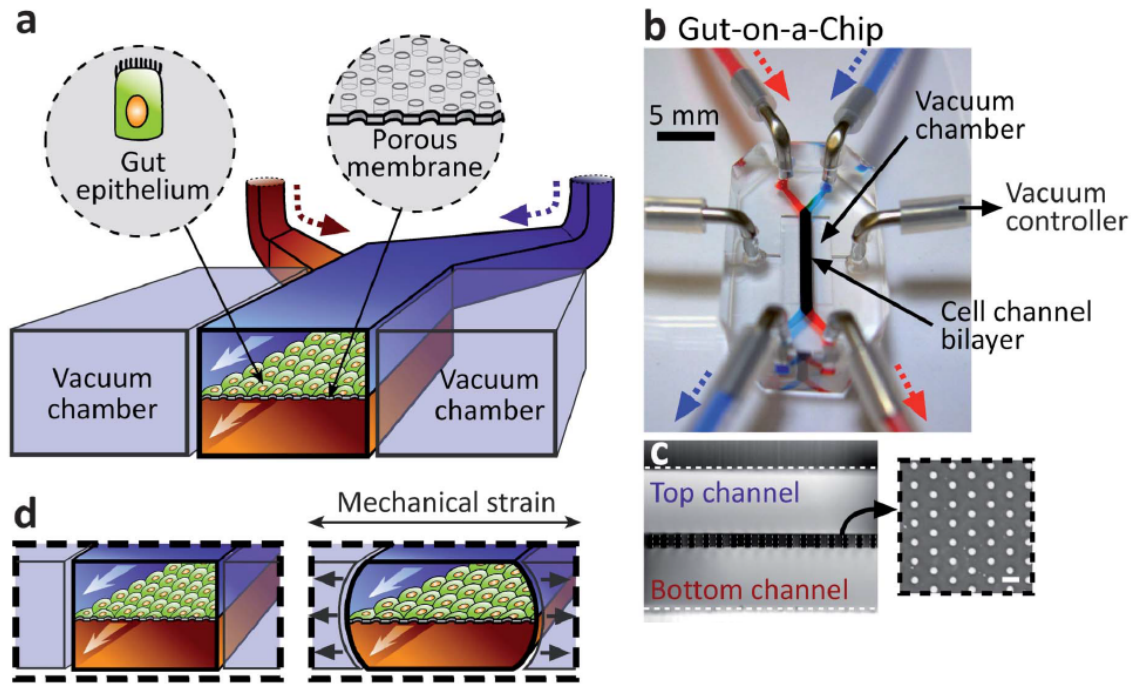


Figure 2.10: Gut-on-a-chip [64].

[57]. Other investigations on Polyglycolic Acid (PGA) scaffold showed that vascular and alveolar regeneration are supported by PGA scaffold [58]. However, synthetic scaffolds for lung tissue engineering were not able to create a network branching or produce ECM components which lie between the capillary endothelium and the alveolar epithelium. In addition, native lung ECM contains a variety of proteins such as collagen, elastin, and fibronectin which do not exist in synthetic materials to provide structural and biochemical supports to the supporting cells [59].

2.1.5 Gut-on-a-Chip

Gastrointestinal elementary unit substantially a barrier composed by mucosa, sub-mucosa, muscular layer and adventitia. Among the *in vitro* models of the human intestine available, Transwell filter inserts allow the formation of a transepithelial barrier and this enables studies on transport [60, 61]. Miniaturized microfluidic models and hydrogel substrates are also utilized to culture human intestinal epithelial cells in mimicking the shape, size, and density of human intestinal villi. Kim et al. have developed a human gut-on-a-chip system to study and perturb critical gut functions associated with physiological cues, including cyclic mechanical strain, fluid flow, and the coexistence of microbial flora (Figure 2.10) [62, 63].

This microdevice is composed of a central microchannel, separated into two microfluidic channels to mimic the complex structure and physiology of the living intestine by using a porous flexible membrane. The full-height vacuum chambers on both sides provide mechanical strain to the intestinal monolayer, mimicking normal peristaltic motions. The membrane is coated with ECM and is lined with human intestinal epithelial (Caco-2) cells. They have demonstrated that this model can promote intestinal epithelial cell differentiation, increased intestinal barrier function,

and can form 3D villus-like structures by recapitulating the low levels ($30\mu L/h^1$) of fluid flow and shear stress ($0.02 /cm^2$) experienced in the living intestine. In addition, cyclic mechanical strain could enhance these responses better than cells cultured in static Transwell models [62]. Moreover, a normal intestinal microbial flora could be cocultured successfully on the luminal surface of the cultured epithelium for extended periods without compromising epithelial cell viability. Thus, this gut-on-a-chip system recapitulates multiple dynamic physical and functional features of the human intestine and will allow further studies on transepithelial transport, absorption, and drug toxicity [27]. Compared with conventional Caco-2 cell monolayers cultured in a static Transwell system, the model gives increased intestinal surface area and absorptive efficiency similar to the normal human intestine [27]. It has been developed also a gut-on-a-chip based on a membrane, which apical and basolateral sides are accessible via microfluidic streams [60]. There are also some attempts to use multiple cell types to develop gastrointestinal tract models and combine them with models of liver tissue [3].

2.2 Methods to assess barrier integrity

The improved complexity of such culture devices could further improve prediction and reduce animal experiments upon careful validation in the future. In addition, microfluidic devices have the potential for high-throughput and multiplex biomarker screening, using both traditional techniques like live cell fluorescent imaging or analysis of the perfusion medium [17] and less invasive and relative new ones, like TEER measurements. Conventional techniques are based on chemicals and, aside from being labor intensive and resource consuming, they require also the use of chemicals and labeling steps that may interfere with the transport process or disrupt cellular functions, therefore, the barrier integrity itself. An alternative is the measurement of TEER.

2.2.1 Traditional permeability methods

Among conventional quantitative measurements of the permeability of the barrier there are hydrophilic compounds of various molecular weights like radioactively labeled markers (i.e., sucrose, inulin, mannitol, albumin), nonradioactive fluorescence-labeled marker proteins (i.e., fluorescein isothiocyanate (FITC)- labeled dextrans), or enzymatic markers (i.e., as horseradish peroxidase, known also as HRP) [3]. It is possible to obtain in these ways actual images of the systems under focus and most of them are used for studies *in vivo*, *in vitro* and *in situ*. Many of these assays do not provide real-time insight about the barrier quality during cell proliferation and growth.

An ideal marker should be:

- metabolically inert,
- non-toxic,
- not bound to other molecules such as proteins in plasma or tissues,
- available in a range of molecular sizes,

- visible in the range from the naked eye to the electron microscopical level,
- reliably quantifiable.

The use of radiolabeled sucrose and inulin have an important advantage of these markers is that they allow a quantitative determination of BBB permeability. Sucrose is a small water-soluble molecule that is not metabolized to a significant extent if injected parenterally. It distributes in the extracellular space of most tissues and organs of the body. Because sucrose is excreted via the kidneys, a single injection causes a rapid rise in blood level, followed by a rapid decline with mixing and distribution into the extracellular fluid and then a slower but steady decline due to loss in the urine [65].

The immunohistochemical methods involve the process of selectively imaging antigens in cells of a tissue section by exploiting the principle of antibodies binding specifically to antigens in biological tissues. They are reliable and useful for double labeling [66] because it is often difficult to detect vascular antigens without special treatments [67]. In brain sections of proteins in plasma, such as albumin [68, 69] immunoglobulin [69, 70] and fibrinogen, immunohistochemical detection has been used to visualize breaches in the blood-brain barrier. Endogenous proteins have the advantage that they are already present in situ and do not need to be injected, thus avoiding potentially un-physiological conditions. Their limitation is that once they have entered the extracellular space of the brain they will continue to diffuse and therefore are not a reliable index of the duration or progression of the leak across brain barriers [71].

Sodium fluorescein (376 Da) is a low molecular weight marker and it appears to be considerably less toxic than HRP. It shows only weak binding to proteins in plasma, which gives some justification for it being the second (with HRP) most commonly used marker for BBB integrity. Dextrans are complex branched polysaccharides made of many glucose molecules. They consist of chains of lengths varying from 3 to 2000 kDa. The biotin and fluorophor labeled dextrans are highly purified and, because of the sensitivity of the techniques applied to visualize the labels, only small amounts are required. Labeled dextrans are valuable markers of barrier integrity, and in the small concentrations they appear to be non-toxic. The biotin labeled form is particularly valuable as it can be visualized at both the light and electron microscopical level [65].

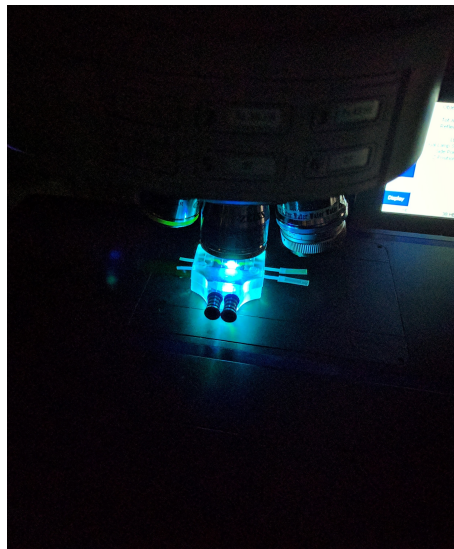


Figure 2.11: FITC method used for study the diffusion in our hydrogel-based 2D model.

HRP is an enzyme used extensively in biochemistry applications. Alone is of

little value: its presence must be made visible using a substrate that, when oxidized by HRP, yields a characteristic change that is detectable by spectrophotometric methods [72, 73]. It produces a coloured, fluorimetric, or luminescent derivative of the labeled molecule when incubated with a proper substrate, allowing it to be detected and quantified. HRP is often used in conjugates to determine the presence of a molecular target. For example, an antibody conjugated to HRP may be used to detect a small amount of a specific protein in a western blot.

Fluorescein isothiocyanate (FITC) method is efficient and low-cost, reliable and stable. FITC, indeed, binds covalently to amine group on cellular components of tissues and therefore dislocations of fluorescent dye could not occur [74]. General advantages of FITC-inulin method include that it is a non-radioactive technique, it is possible to repeat measurements multiple times in the same mouse, the assay can be performed in conscious mice, no urine collection is required, and a high-throughput option can be utilized. Disadvantages for the single bolus injection include the need for dialysis of FITC-inulin, which can be overcome by using a better FITC-marker, FITC-sinistrin, which is available now and can be measured transcutaneously using a special miniaturized device [75].

2.2.2 TEER

Transepithelial/transendothelial electrical resistance (TEER) is a widely accepted quantitative technique to measure the integrity of a cellular monolayer and the presence of tight junction. TEER measurement is a very sensitive and reliable method to confirm the integrity and permeability of the monolayer before they are evaluated for transport of drugs or chemicals. It has also been used to evaluate various cell types as in vitro drug transport model [76].

TEER is particularly useful for dynamic microfluidic experiments because it can investigate the dynamics in cell culture models of endothelial and epithelial tissue. Measurements can be performed in real time without cell damage and generally are based on measuring ohmic resistance or measuring impedance across a wide spectrum of frequencies. Although there are other techniques to assure the integrity of the tight junctions and of the cell monolayer, TEER determines different experimental parameters. TEER, indeed, reflects the ionic conductance of the paracellular pathway in the epithelial monolayer, whereas the flux of nonelectrolyte tracers indicates the paracellular water flow, as well as the pore size of the tight junctions [3]. Existing systems for measuring TEER, however, are limited to static or macroscopic cell environments and difficult to adapt to microchannels. The challenge in organ-on-a-chip systems arises because of :

1. the small cell culture area for TEER measurement,
2. the high electrical resistance along the length of the microchannel, dictating electrode placement in immediate proximity of the cell culture area,
3. measurement to measurement variances if the recording electrodes are not secured within the channel.

Embedding and immobilizing TEER recording electrodes directly within the microfluidic channel, in close proximity to the cell monolayer, eliminates the systemic

electrical resistance of growth media within the microchannel and reduces signal noise resulting from electrode motion [77].

TEER values may be obtained from microfluidic system, but also from classical Transwell plates. Actually, most of the commercially available apparatuses for these measurements are designed for such kind of structures. Anyway, more studies are needed to prove that those measurements are directly comparable, both between similar devices and cell type. Nevertheless, such systems allows to characterize systems in different ways and may make it possible to investigate the influence that shear stress has on the barrier function [3]. In chapter 4 it is going to be studied in deep how data are acquired, analyzed and the factors influencing the acquisitions.

Chapter 3

Fabrication techniques in Tissue Engineering

This chapter is dedicated to a review of the fabrication techniques applied to tissue engineering. Apart from the well-established techniques derived from the micro-electronic engineering, are listed CAD-based rapid prototyping methods, that are: fused deposition modeling (FDM), laser sintering, stereolithography, inkjet based techniques, direct bioprinting and replica molding. For biocompatibility and physiological accuracy have been exploited several material, with natural or syntetic origin. Beside all these materials, it was chosen the hydrogel for the construction of our gut-on-a-chip.

3.1 Cell scaffold and ECM

The previous chapter several solutions were investigated in order to study barrier physiology and organs-on-a-chip systems. The first important request, that has to be addressed in the fabrication of such structures, is the problem of the cells scaffold [78]. The scaffold materials should have some basic characteristics, for example it should be non-antigenic, non carcinogenic, nontoxic, non teratogenic, and be biocompatible. Besides material issues, the macro and microstructural properties of the scaffold are also very important, from the biological point of view. The designed matrix indeed should [79, 80]:

- serve as an immobilization site for transplanted cells;
- form a protective space to prevent unwanted tissue growth;
- direct migration or growth of cells via surface properties of the scaffold;
- direct migration or growth of cells via release of soluble molecules such as growth factors, hormones, and/or cytokines [81].

Biocompatible scaffolds and surfaces should mimic the macro, micro and nano structure of systems, in order to success in modeling organs, cells and biomolecules physiological behavior [82].

For example, researchers have found that the pore sizes of the scaffold has a significant influence on gene regulation. Cultures of endothelial cells on the honeycomb scaffolds, specifically with 5 mm pore size, indeed, showed to provide high levels of

proliferation [83]. Similarly neural stem cells were cultured on 3D honeycomb materials with a pore size of 3 mm, and were found to undergo accelerated proliferation while such a 3D structure did not support differentiation of NSCs into neurons [84]. In addition, the pore size of the honeycomb pattern demonstrated also to affect the function of mesenteric-visceral adipocyte (cells that primarily compose adipose tissue, specialized in storing energy), with the result that a honeycomb film with a pore size of 20 mm had the highest cell functions [84].

Cells are bound to each other through binding sites located on the cell membrane and are connected to surrounding cells by the ECM [85]. The ECM, as well the internal structure of each cell, or rather cytoskeleton, is a continuous framework, formed by protein and polysaccharide filaments. Considering the nature of the ECM, it represents a natural choice for a scaffold. This is why researchers are developing methods for decellularizing rodent and human lungs or lung sections and reseeded human lung cells onto the ECM in order to better understand disease, modeling cell-ECM interactions [49].

In order to create a mold for the ECM may be exploit conventional fabrication techniques [81]. Microfabrication techniques, such as micromachining, photolithography, metal deposition, electrospinning, wet and dry etching, thin-film growth and 3D printing, allow the realization of features on the micron and submicron scale on several types of materials and surfaces. Moreover other techniques such as electron beam lithography (EBL) and focused ion beam (FIBL) lithography assure the fabrication of structures with nanometer details [86, 87, 82]. However techniques such as solvent casting, fiber bonding, and membrane lamination are dangerous for biological applications because of the use of toxic solvents, difficult to remove. Moreover, solvent casting and fiber bonding do not allow a multiple layer design, and membrane lamination allows only a limited number of interconnected pore networks. On the other hand, rapid prototyping technologies, such as 3D printing and 3D plotting, can produce scaffolds with differentiated 3D structures by joining together liquid, powder, and sheet materials layer by layer according to a computer-generated model [81].

3.2 Etching and Directwrite Techniques

Such techniques are well established for silicon-based chips. The two approaches adopted, by means of different nanotechnology techniques, are the bottom-up and top-down in order to realize micro- and nanostructured materials.

Supramolecular chemistry and surface science are techniques of the bottom-up approaches. They indeed enable the combination of various layers, made from different materials or incorporating different biochemical compound. Biocompatible nanostructured surfaces have been fabricated also with a top-down approach, via etching away bulk material to achieve the required smaller structural architectures [82] or through electrospinning by directly shaping the materials into the desired structure. The electrospinning and 3D electrospinning technique, for example, enable the production structures, in the micro or nano scale, such as continuous, self-aligned, fiber-by-fiber, and template-free manner fibers. Those structures show growing potential in tissue engineering applications.

Anyway, also plasma etching is becoming more common for tissue engineering application as surface treatment technique. Using plasma surface modification technique

make possible to change the surface properties of different biomaterial by enhancing their biocompatibility without altering their bulk properties. Dry etching represents a nanolithographic process assisted by plasma that, in conjunction with soft lithography, nanoimprint lithography, and dip-pen lithography, as well as EBL and FIBL has been utilized for patterning surfaces with nanometer resolution. Such techniques allow to fabricate nano featured substrates that can enhance the expression of a phenotype. E.g., nano patterned substrates fabricated using nickel electroforming against a nanoporous anodic aluminum oxide, followed by nanoinjection molding or hot embossing process, showed to enhance neural differentiation [82, 88].

Photolithographic patterns can be generated in polymer films and in monolayers. The 3D patterned structures are created by a two-step method. In the first step, a particular area of a surface, coated with a photoresist, is exposed to UV irradiation. This allows photopolymerisation, photocrosslinking or other chemical reactions such as functionalization and decomposition reactions, or induces phase separation in the exposed areas. In the next step of the process, the remaining polymer surface area which was not exposed to UV radiation remains unreacted and when removed by dissolving in an appropriate solvent it creates a 3D pattern surface. Photolithography is a high-throughput technique, and is suitable for a large-area of 3D surface pattern generation with good alignment and topography [84]. The combination of such techniques represent a way to produce directly the final product. However, because of the expensive and delicate tools and the need of a clean room, such techniques are exploited just to fabricate molds to generate the final product with cheaper materials (usually polymers) and techniques (e.g. replica molding).

Anyway a drawback of such traditional scaffold fabrication methods is the limited control of pore size and shape and lack the sensitivity to precisely determine scaffold architecture [89]. Moreover standard microfabrication processing methods such as optical lithography, deposition, and etching, optimized for materials such as silicon and glass, are usually not suitable for natural and synthetic biomaterials without being coupled with other techniques [82].

3.3 CAD-based rapid prototyping methods

Until now, various 3D printing technologies such as stereolithography (SLA), fused deposition modeling (FDM), inkjet-based printing and selective laser sintering (SLS) have been developed. These technologies show high reproducibility of a final product because of the use of Computer Aided Design and of highly accurate Computer aided manufacturing systems [90]. Moreover, these methods may use medical data having the acces to computed tomography and magnetic resonance images, therefore they can supply a scaffold that is customized for a patient [91].

In contrast with traditional techniques, CAD-based rapid prototyping methods provide excellent spatial control over polymer architecture and have successfully been applied to the fabrication of 3D tissue engineering scaffolds.

3.3.1 Fused deposition modeling (FDM)

FDM combines heat and extrusion techniques to create 3D scaffolds layer by layer. A nozzle directs a stream of molten plastic or ceramic onto a previously deposited layer of material. Controlling the direction of material deposition, layer by layer,

scaffolds with complex internal organization can be fabricated, also with the help of sacrificial structures. This approach was used to produce biodegradable poly(ϵ -caprolactone) (PCL) scaffolds exhibiting various honeycomb geometries with finely tuned pore and channel dimensions of 250-700 μm [92]. Primary human fibroblasts cultured in these scaffolds proliferated and produced extracellular matrix [93]. Scaffolds composed of other biocompatible polymers and composites have demonstrated utility for various tissue engineering applications [94, 95]. While FDM exhibits high pattern resolution in the xy-plane, it is instead limited in the z-direction by the diameter of the extruded polymer filament that defines layer thickness and corresponding pore height. Further, high processing temperatures, usually higher than 100°C, limit the biomaterials that are compatible with the method. However, FDM capabilities are expanding with new developments such as multi-phase jet solidification (MJS), a technique that allows simultaneous extrusion of multiple melted materials [93]. Light-Mediated Fabrication Light energy can also be used to fabricate structured 3D polymer scaffolds through photopolymerization process: it uses light to initiate a chain reaction that solidifies a liquid polymer solution [89].

Often there is the need with FDM of structural materials to obtain the final design, therefore it is used a sacrificial technique [96, 97, 98]. 3D sacrificial molding required the use of processing conditions, for either removing the sacrificial filaments or casting the surrounding material, that could not be accomplished with aqueous-based ECMs or in the presence of living cells. By the contrary, Miller et al. were the first ones that coupled the 3D sacrificial molding with ECMs and living cells. They used FDM to fabricate 3D sacrificial lattice like templates using a glass carbohydrate material. The peculiarity of their 3D printed templates was that the glass carbohydrate material used to fabricate the 3D templates were water soluble. Such technique can be actually applied in other several fabrication techniques, such as molding [99, 100], bioprinting [101], and stereolithography [102, 103], using materials like carbohydrate glass, sodium alginate and PVA. In some cases the sacrificial templates employed to fabricate the constructs were rather simple, e.g. based on single or parallel planar microchannels [96, 100, 98]. In others, the complex sacrificial templates were achieved by several fabrication steps [97, 102, 103] and the final constructs did not have a clear strategy of active perfusion [96, 98, 99, 104]. The fabrication method can also be applied to other synthetic or natural polymers as demonstrated by fabricating scaffolds in different hydrogel [49].

For example such technique was employed for fabricating scaffolds by 3D printing using a sacrificial water dissolvable PVA mould [49]. Different designs of PDMS scaffolds were successfully prepared, and the fabrication technique allowed the tuning of physical and mechanical properties by controlling the 3D printing parameter. After 12 days of cell culturing it was observed a very high density of cells, homogeneously distribution across the scaffold due to good mass and oxygen transport into the scaffold. Furthermore, the fabricated scaffold can be scaled up to sizes relevant for bioartificial organs. In conclusion, the described process is scalable, compatible with cell culture, rapid, and inexpensive [49].

3.3.2 Laser sintering

Laser sintering (LS), also referred to as selective laser sintering (SLS), is a rapid prototyping and manufacturing technique utilising a laser to fuse or sinter powder

particles to form solid objects. Complex shapes can be produced with LS technique, like other rapid prototyping (RP) techniques, such as stereolithography, fused deposition modelling, 3D printing, etc. It is possible to create closed volumes, however unsintered powder will be trapped in the volume. At first it is designed a volumetric model, as with the other rapid prototyping methods, that is afterwards divided into slices with thicknesses, determined by the sintering process and that are typically in the region of 0.10-0.15 mm, and then transferred to the scanner unit of the machine. Based on the cross sectional image of the sliced part, the laser scans selective areas of the preheated powder bed, where the powder particles melt and solidify quickly to form a dense part. To establish fusion with the current layer, the laser energy also partially liquefies the previous layer.

The minimum feature size, which directly depends on the laser spot diameter, slightly limits the usability of the machines for tissue engineering scaffolds, where in general highly porous constructs are desired. However, a significant advantage of the SLS process over some other rapid prototyping techniques is that no toxic solvents or binders are needed. A drawback related to such technique is not suitable for massive production because it is not possible to parallelize the process [105].

3.3.3 Stereolithography

SLA is a photopolymerization method that utilizes a deflected UV laser beam to irradiate and solidify exposed polymer regions at the surface of a tank of photosensitive polymer. Multiple layers are formed sequentially by lowering the stage and repeating the laser illumination. While SLA machines are traditionally used to build prototypes and molds for implants, it is however possible to use to directly fabricate 3D scaffolds with appropriate resins. For example in some studies was exploited a photocurable ceramic acrylate suspension formed cancellous bone [106] and hydroxyapatite bone tissue scaffolds [107], with overall dimensions suitable for healing critical-sized (4 mm thickness, 50 mm diameter) bone defects. As with SLS, SLA is limited in resolution by laser beam diameter to approximately 250 μm , although small-spot laser systems exist and have demonstrated the production of smaller (70 μm) features [89].

3.3.4 Microstereolithography

Micro-stereolithography (MSTL) is a 3D printing technique based on SLA: it produces a 3D structure by stacking solidified layers fabricated using UV laser and UV curable polymer. MSTL is a relatively new approach which shares the same principle with SLA. However, to get a better resolution, the laser beam is focused more precisely in order to reduce the spot size to a few micrometers of diameter to solidify a thin layer of 1-10 μm in thickness [108]. MSTL can make a scaffolds with micro-level pores due to the high resolution of the focused laser beam that it uses [109, 110]. However, the main components of MSTL are bulky and expensive. Furthermore, because most photo-curable polymers do not guarantee cell safety and biodegradability, the materials used to construct the scaffold have their own demerits. Therefore, studies related to the use of MSTL to fabricate scaffolds for application to tissue engineering are rare [92].

Lee et al. [111] evaluated the mechanical properties and cell proliferation based on internal pore size and 3D architecture of scaffolds fabricated by MSTL and poly (propylene fumarate) (PPF) based materials. The authors pointed out that cell proliferation on the MSTL scaffold was clearly superior and indicated that MSTL would be a good replacement for conventional scaffolds fabrication methods. Moreover to improve the bioactivity of scaffolds, structures containing hydroxyapatite composites have been fabricated by MSTL and resins containing dispersed hydroxyapatite particles. By mixing PPF and hydroxyapatite particles in diethyl fumarate (DEF) as reactive diluent, a photopolymerisable composite resin was obtained and scaffolds containing nano/microscale structures of PPF -HA photopolymer were successfully fabricated [112]. It was reported that the developed MSTL system and the use of PPF is promising in fabricating complex microscaffolds with prescribed micro-architectures [108].

The basic concept of Blu-ray MSTL is to replace a UV laser source and complex optical systems with a Blu-ray Optical pickup unit (OPU) and to reduce the size of the system. A laser of wave length λ of 450 nm is emitted from the OPU; this laser can cure the photopolymer. The maximum power of 990 μ W is high enough to facilitate photo-crosslinking among various photopolymers. For use as a 3D printing system, the Blu-ray system was modified in several ways. The objective lens of the original OPU has a focal length < 1 mm. In such a scaffold cells were seeded. It was thus showed that Blu-ray based MSTL could fabricate a precise biodegradable 3D scaffold using a UV curable polymer as designed. It was also fabricated a 3D scaffold using PPF/DEF biodegradable photopolymer and a Blu-ray MSTL which is simpler and more compact than the conventional MSTL. To evaluate the cytotoxicity of the PPF/DEF 3D scaffold, pre- osteoblasts were cultured for 7 days. It was also developed a multi-stimulus bioreactor system which mimics the in-vivo perfusion environment and supplies the magnetic field to improve cell proliferation. A cell culture result showed the superiority of our multi-stimuli bioreactor system on the PPF/DEF 3D scaffold, indicating that the combination of the Blu-ray based MSTL to fabricate 3D scaffolds, and the multi-stimulus bioreactor system to stimulated growth of cells, has potential to reduce the cost of surgery for bone replacement [91].

3.3.5 Inkjet based techniques

The solid free-form method is an ink-jet printing technique. This has been utilised to generate 3D patterns of polymers onto a substrate by either drop-on-demand or continuous mode, a solution based writing process onto substrates. In the case former types, signals are used to control the ejection of an individual droplet. While in latter systems, ink emerges continuously from a nozzle under pressure, and the jet breaks up into a line of continuous droplets, and the electric signals play a role in controlling the direction of the jet. In a study [113] neuron-adhesive patterns were generated using biodegradable polymers, namely the collagen and PDL mixture via selectively ink-jet printing on the PEG surface. In these patterns PEG acts as the cell-repulsive material, while the collagen/PDL mixture acts as the cell-adhesive material.

The inkjet printing technique is used for the construction of synthetic biodegradable scaffolds via printing of crosslinkers onto liquid alginate/gelatin solutions, which

formed 3D hydrogel scaffolds. Furthermore, this method does not use UV radiation for curing and causes no damage to light-sensitive molecules. This allows the use of light sensitive bioactive molecules in the fabrication of devices. Several research groups have demonstrated in their published literature reports [114] that this method can be used to fabricate suitable devices in photonics, microfluidics, bio-mineralization [81]. The most promising application is the fabrication of the scaffold-matrix for cellular attachment, proliferation and differentiation for tissue regeneration [84].

Structural polysaccharide nanocrystals (NCs), including cellulosic one, have recently attracted considerable attention because of their well defined dimensions (~ 10 nm diameter and ~ 100 nm length), excellent mechanical properties [115] and aqueous mesophase formability. For formulating commercial inkjet inks, in general, pigments have to be dispersed and the dispersion needs to be made colloidally stable, whereas the NCs are essentially suspended in water without any other additives [116]. Even though the inkjet process requires suitable ranges of viscosity and surface tension for inks, these can be satisfied for diluted aqueous systems of NCs. In order to fabricate a biocompatible scaffold and focus on its potential bioactivity it was created chitinous NCs (ChNCs). In particular it was developed an ink based on chitinous ChNCs to study the cell adhesiveness and aim to utilize it for micropatterning of animal cells. It was provided for the following inkjet printing as the ChNC ink. Even though the printing was successfully performed, these substrates themselves exhibited a considerable cell adhesionability. To improve ink characteristics it was prepared chitin NC and its deacetylated ones (dChNC) under alkaline conditions. The series of aqueous suspensions of NCs were successfully discharged by a research inkjet printer, and the deposit form of microstructures could be controlled by printing conditions. The dChNC fine moldings printed on a cellophane substrate were good scaffolds for mouse fibroblasts and the cell micropatterning was accomplished. Micropatterning cell scaffolds permit fruitful applications such as controlling of cellular shapes, precise monitoring molecular events in biochemistry, and drug screening [117]. Accurate processes for fabricating such scaffolds have been performed mainly by photolithography and fine laser-ablation. In fact, such micro-processing concept can be acquired by the inkjet printing technology, which is further attractive from the viewpoints of simple contactless procedure, flexibility of choosing inks and substrates, no necessity of using harmful chemicals and suitability for wide-ranging on-demand productions [118].

3.3.6 Direct bioprinting

Current 3D bioprinting technologies can be divided into indirect and direct fabrications. The indirect 3D bioprinting is defined by firstly creating negative sacrificial molds, followed by casting with desired positive biomaterial and a subsequential selective removal of the molds [101, 119, 120]. Direct 3D bioprinting techniques, instead, generate 3D structures in a point-by-point or layer-by-layer manner, offering feasibility in depositing multiple cell types but also biomaterials to achieve tissue constructs with improved reproducibility and heterogeneity to mimic in vivo systems.

In order to afford a spectrum of properties, such as biocompatibility and appropriate physical assets, to ensure printability and long-term functionality following

deposition, different bioinks have been developed [121, 122]. They are based on both naturally derived and synthetic biomaterials. One of the most important properties for the bioprinting, for example, is the viscosity of the bioink which determines indeed the flexibility in deposition of freestanding structures and maintenance of architectural integrity immediately after bioprinting [122]. Shear-thinning biomaterials such as those based on Pluronic, gelatin, PEG, or their combinations with other hydrogels, are often utilized as bioinks, which possess a liquid-like behavior under high shear stress during the extrusion process, but can quickly recover their gel state once bioprinted and thus prevent the structure from collapsing [123, 124]. Longterm stability of the bioprinted tissue constructs, however, typically depends on a secondary crosslinking mechanism to further stabilize the bioprinted structures. The bioinks may be crosslinked physically and chemically. Gels crosslinked physically are typically unstable over an extended period of time and they are subject to dissolution, thus they can function effectively as fugitive templates where only temporal stability is required, such as in cases of fabricating sacrificial bioprinted constructs like the vasculature systems [96, 119]. On the other hand, chemically crosslinked gels possess better long-term stability and are suitable for constructive bioprinting to function as the biomimetic ECM. Possible bioinks are hydrogels (collagen, gelatin or others) but also decellularized ECMs, with all the challenges that each material brings. Despite these challenges, it is expected that 3D bioprinting will eventually become one of the most efficient, reliable, and convenient methods to biofabricate tissue constructs in the near future, with new niches for technological developments on the instrumentation with improved spatial and temporal resolutions as well as optimized bioinks and cell sources for specific organs. Combination with the stem cell technologies and advanced materials engineering approaches, featuring stimuli-responsiveness, will further allow temporal evolution of bioprinted tissue constructs, potentially meeting the requirements of dynamic tissue remodeling during developmental processes [125].

The direct bioprinting fabrication technique was employed to fabricate vascular tissue constructs by a layer by layer deposition of hydrogels and cells at the same time [121, 126, 127]. 3D bioprinted construct using an engineered blend ink based three different hydrogels for example can be created. In one study the hydrogel enrolled were gelatin methacryloyl, sodium alginate, and 4-arm poly(ethylene glycol)-tetraacrylate (PEGTA). The ink was bioprinted using a tri-layered coaxial nozzle to generate perfusable structures with cells encapsulated on it. It has also been showed that the spatial deposition control of the ink can be obtained creating 2D structures with different shapes, and by creating also 3D lattice-like structures with encapsulated cells on it [128].

Vascularize tissues, having therefore the possibility of creating effective 3D tissue models, is one of the challenges related to organs-on-a-chip. Therefore there are great efforts in that sense. Zhu et al. for example, using a microscale continuous optical bioprinting (μ COB), could develop a pre-vascularized construct. The encapsulation of different cell lines was reached with a mixture of gelatin methacryloyl and LAP. They have showed that their fabrication technique was fast (~ 1 min) and was able to have good cell viability ($\sim 80\%$).

In another study, Pluronic F127 was exploited as fugitive ink to fabricate microchannels. It has been developed a fabrication technique, called integrated tissue-organ printer (ITOP), that basically consists on printing several materials at the same

time with different purposes: bioinks made by ECMs with cells encapsulated are used to define the location of the cells whereas pluronic F127 is used to create a network of microchannels with the purpose to enhance the transport of oxygen and nutrients. To increase the mechanical properties of the final fabricated tissue construct, PCL was also printed together with the other inks. They showed that they could fabricate large constructs with different sizes and morphologies. Moreover, they demonstrated that the different fabricated engineer constructs were able to be implanted in vivo regenerating the damaged tissue without any host immune response [104, 129].

In the future, this organ-printing technology may allow for precise 3D cell positioning that could be scaled up to larger tissue engineered constructs [130]. One disadvantage of direct cellular assembly is that constructs may not possess adequate mechanical stability for tissue engineering applications. Conversely, acellular scaffolds have excellent mechanical strength but may be difficult to populate with cells [89].

3.4 Replica Molding

The 3D molding technique consists of the fabrication of a rigid 3D template, used as a negative mold to define the network of the microfluidic architecture, the casting of the 3D template into a suitable material and the sacrifice of the template revealing a microfluidic architecture in the bulk material. In order to go through those steps may be used both standard microfabrication techniques and also CAD based techniques.

Other nanofabrication routes, such as replica molding (RM) and embossing, have been developed for patterning nanoscale structures. The formation of these kind of structures requires a high-resolution master, typically generated by conventional nanofabrication techniques that can be replicated by molding or embossing [131]. Hot embossing, thermal forming, solvent casting and injection molding require dedicated tools such as a hot-press or injection molding machines and can be used to create small patterns into different thermoplastics biocompatible materials [82]. RM and soft lithography techniques allowed the obtainment of replicas, realized using biocompatible polymers (PDMS, polystyrene and so on), characterized by nanometric features (down to 50 nm) [132]. The indirect fabrication strategy is advantageous for sensitive biomaterials that are incompatible with fabrication conditions, since only the mold itself is subjected to the processing environment. Further, the resulting scaffold represents an inverse of the mold, thereby extending the 3D design possibilities [89].

3.5 Scaffold materials

The biomaterials which are derived from polymers generally fall into two categories: naturally occurring and human-made synthetic materials. The polymers derived from synthetic origins are divided into two classes: non-biodegradable and biodegradable synthetic polymers. For example, the crosslinked form of soft polymers, classified as hydrogels, is a class of new generation of exciting biomaterials that has demonstrated the ability to form scaffolds for a variety of uses, such as tissue

engineering, delivery of active molecules, and biosensors and actuators. Biomaterial scaffolds have been synthesized from different types of organic and inorganic polymers and materials including polymers of natural and synthetic origin, ceramics, and their composites. Scaffold materials must be designed to mimic the 3D structure of the native tissue and have the ability to act as delivery agents for growth factors, drugs/antibiotics, and chemotherapeutic agents, depending on the nature of the tissue to be repaired [84].

Microfabricated gel constructs have been realized using RM techniques. Natural biomaterials such as collagen, gelatin and fibroin [133] and synthetic thermoplastic biopolymers such as poly(l-lactic acid) (PLA), PCL, and poly(l-lactic-co-glycolic acid) (PLGA) have been used in a wide range of tissue engineering application [134]. For example, nano featured substrates fabricated using nickel electroforming against a nanoporous anodic aluminum oxide followed by nanoinjection molding or hot embossing process, have been developed able to enhance neural differentiation [82, 88]. Alternatively, hydroxyapatite/acrylate suspension was casted onto a negative epoxy mandible mold made by stereolithography [135]. After heat-curing the polymer, the mold and acrylate binder were incinerated. The resulting hydroxyapatite scaffolds contained different internal channel architectures and resulted in bone ingrowth in minipigs up to nine weeks post-implantation [136]. Others have created molds for indirect scaffolds using 3D printing by depositing wax or other low melting point compounds that can be later removed with elevated temperature or solvents. This method has been combined with particulate leaching to indirectly fabricate porous scaffolds composed of hydroxyapatite, poly(L)lactide, and polyglycolide [137]. These cell layering techniques have limited capability for the formation of complex 3D patterned structures. Instead of using cell monolayers that fuse into a sheet, some groups have achieved greater complexity of tissue construction by the selective delivery and spontaneous fusion of living cells into 3D structures. Mironov et al., indeed, used a jet-based printer to position cell aggregates and embryonic heart mesenchymal fragments that fused together within biocompatible gels of varying chemical and mechanical properties [89, 138].

3.5.1 Hydrogels

Hydrogels are crosslinked networks of insoluble hydrophilic polymers that swell with water. Their increasing popularity as tissue engineering biomaterials reflects mechanical properties and high water content analogous to those of natural tissue [89]. Biological hydrogels are traditionally used to establish biomolecule gradients around cells *in vitro*, using several stratagems. The biological hydrogel method has several unique features that have made it popular for exposing cells to biomolecule gradients. First, the gels are easy to make and provide cells with an environment that is, in theory, more similar to *in vivo* tissue than conventional two-dimensional culture substrates. Second, the high network density of the gels allows the movement of chemical species to occur only via free diffusion, unaffected by bulk fluid movement around the gel. Third, the biological hydrogel method offers significant control over the positions of the biomolecule sources, enabling the generation of gradients with specific orientations, or combinatorial gradients of multiple factors over distances as small as 2 mm. The optical properties of some gels also make it difficult to distinguish the cell from the hydrogel background. For example, collagen gels have ordered

fibrils that refract incident light and interfere with phase contrast microscopy [22]. The hydrogels can be manufactured with required properties depending on the chemical structure, composition of starting materials, density of linking of polymer chains, hydrophobicity and hydrophilicity for a particular biomedical application.

Hydrogels can be synthesised both from natural and synthetic polymers. The examples of hydrogels from natural polymers are: collagen, gelatin, hyaluronic acid, chondroitin sulfate, chitin and chitosan, alginate, starch, cellulose, and their derivatives. Hydrogels from natural polymers have many advantages over the synthetically derived ones: low toxicity and good biocompatibility because of their chemical structures and are very akin to the structure of glycosaminoglycan molecules, present in the native ECM. Hydrogels from synthetic polymers are prepared by chemical polymerisation methods. Various types of monomers, for examples, acrylates, methacrylates, acrylamides, esters, carboxylic acid and polyfunctional monomers, can be utilised for the preparation of synthetic hydrogels [84].

The 3D structural-integrity and properties of hydrogels are mainly dependent on their method of preparation such as physical or chemical crosslinking reaction. A chemical crosslinking form permanent junction-type networks [84]. The examples of this type of hydrogel include polymerization of the acryloyl group, ionizing radiation-induced crosslinking, small molecule crosslinking with a polymer chain (glutaraldehyde) and polymer-polymer crosslinking by condensation reaction. The physical crosslinking of hydrogels promotes the formation of transient junction-type networks, such as polymer chain entanglements and physical interactions, like ionic interactions, hydrogen bonds, or hydrophobic interactions. Indeed, there are varieties of different polymer structures, which can form physical and chemical hydrogel networks [84].

Light energy can also be used to photopolymerize hydrogel polymer scaffolds that are less rigid than conventional stereolithography materials[89].

Hydrogels, as it was previously discussed, have been used as bioinks but also, and more frequently, as scaffolds. For example, they have been used to create 3D perfusable capillary like microchannel networks using sacrificial poly(N-isopropylacrylamide) (PNIPAM) fibers. The use of PNIPAM as a sacrificial material leverages the attractive combination of a thermal trigger at a threshold between room and physiological temperatures, cytocompatibility, and ease of handling. Solvent spun PNIPAM microfibers yielded capillary-like microchannel networks with sizes, densities, and complexity that have not been achieved using more traditional patterning approaches. Perfusion of the tissue-scale hydrogels improved cell viability significantly compared to channel-less and nonperfused counterparts, indicating adequate soluble compound exchange for supporting high density of metabolically active cells throughout a hydrogel construct. Future studies may investigate optimization of these small vessel network architectures based on the unique metabolic demands of various engineered tissue varieties and co-culture systems [139].

Outside the tissue engineering arena, hydrogel microstructures have been formed by photolithographic patterning with applications such as microfluidic valves [59] and cell-laden microstructures on silicon [140]. Albrecht et al. have developed a complimentary technology capable of defining the organization of encapsulated cells within a hydrogel to a resolution of $< 10 \mu\text{m}$ [141].

This method utilizes electromagnetic fields to specify the position of cells in the liquid polymer solution prior to photocrosslinking. In conjunction with bioactive

hydrogel technologies being explored by numerous groups, the photopatterning of hydrogels containing homogeneous or organized patterns of living cells may lead to the development of improved tissue engineered constructs with customized spatial, physical, and chemical properties [89].

Therefore hydrogel polymers have the ability to provide both structural support and high tissue density while maintaining an in vivo-like environment for cells [142]. Although molding techniques can form hybrid cell/hydrogel constructs with micropatterned external features, they are not amenable to patterning internal structure of complex engineered tissues. However, recent developments have exploited the ability to localize light exposure, and therefore hydrogel crosslinking, in defined micropatterns, potentially allowing the buildup of complex microstructures in a layer by layer manner. The flexibility of these hydrogel systems shows great promise for the fabrication of 3D tissues that mimic the structural, multicellular, and biochemical complexity found in many organs in the body [89].

Chapter 4

Impedance Spectroscopy

TEER measurements consist in the quantification of the resistance of a certain epithelial/endothelial tissue. TEER is expressed in $\Omega \cdot cm^2$ and it has become a well-established method to characterize epithelial and endothelial tissue barrier integrity. The impedance of a monolayer, indeed, is dependent on its confluency, cell differentiation and chemical reactions, but also presence of corpuscles such as tight junctions. TEER measurements success is because they represent a non-destructive, label-free method to quantitatively monitor the integrity and permeability of the barrier in real-time. TEER can be obtained by applying either a DC or AC voltage across the barrier, and measuring the resulting current [3]. Anyway with a measurement of the electrical resistance over a range of AC frequencies may allow to obtain a fully comprehensive analysis of the barrier electrical properties [3, 143]. However, several factors influence the measurement, determining differences in the recordings over different labs.

4.1 Ohm's Law Method, DC versus AC TEER measurements

The classical setup for measurement in Transwell plates, as shown in Figure 4.1, consists of a cellular monolayer cultured on a semipermeable filter. For electrical measurements, are necessary just two electrodes: the electrodes are separated by the cellular monolayer and they are placed respectively above and below the membrane.

One of the options to determine the ohmic resistance can be by applying a DC voltage (or current) to the electrodes and measuring the resulting current. The ohmic resistance is calculated based on Ohm's law, thus as the ratio of the voltage and current. However the drawback of this method is that DC currents can damage both the cells and the electrodes.

To overcome this issue, a single-frequency AC voltage (or current) signal is applied [144]. Impedance spectroscopy is performed by applying a small amplitude AC excitation signal with a frequency sweep and measuring the amplitude and phase response of the resulting current, see Figure 4.2.

An in-depth analysis of impedance spectroscopy across a wide spectrum of frequencies instead of a DC or single-frequency AC TEER measurement can provide ad-

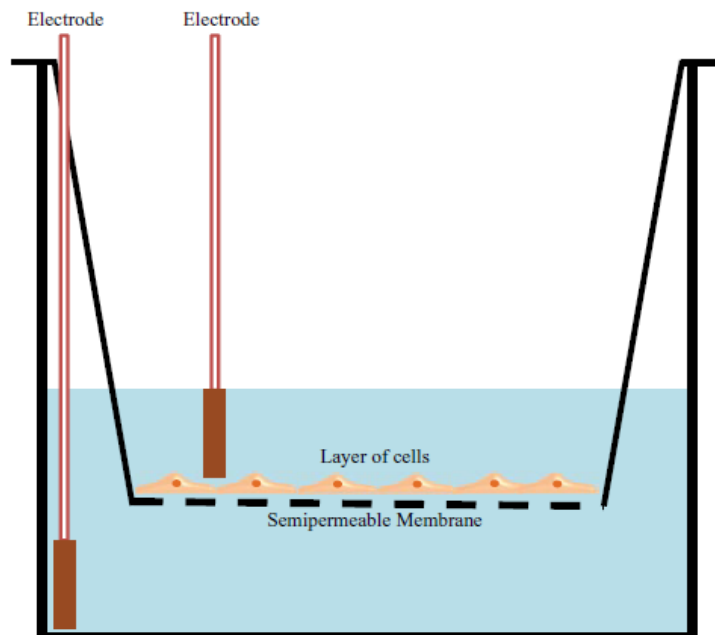


Figure 4.1: TEER measurement with chopstick electrodes [3]

ditional information about the capacitance of the cell layer [3]. Moreover, impedance spectroscopy, when combined with a fitting algorithm, provides a more accurate representation of TEER values than traditional DC or single-frequency AC measurement systems [144].

In the widely used and commercially available TEER measurement systems can be mentioned the Epithelial Voltohmmeter (EVOM; World Precision Instruments, Sarasota, FL). It applies an AC square wave at a frequency of 12.5 Hz is used to avoid any charging effects on the electrodes and the cell layer. The EVOM system has a measurement range of $1 - 9999\Omega$ with a 1Ω resolution, and it uses a pair of electrodes popularly known as a STX2 chopstick electrode pair. Each stick of the electrode pair (4 mm wide and 1 mm thick) contains a silver/silver chloride pellet for measuring voltage and a silver electrode for passing current [3]. Similar to the EVOM, there is Millicell ERS-2 (Millipore) unit that also uses a near DC, 12.5 Hz, current of $10\ \mu\text{A}$ and a 4-point measurement method with either silver/silver chloride chopstick electrodes or special chambers with patterned Ag or AgCl electrodes, which facilitate measurements of TEER in Transwell culture inserts [144]. The Millicell device uses a fixed current of $10\ \mu\text{A}$, which results in potentials that exceed the maximum measurable membrane potential of 200 mV due to the high resistance of the microchannels [144].

An AC measurement system is offered by the company Flocel Inc., but it is tailored towards special proprietary cartridges used for cell culture. Therefore is not easily transferable to organs-on-chips or Transwell systems. Other AC systems commercially available to determine TEER in Transwell are the cellZscope system⁷² (nanoAnalytics GmbH) and the ECIS system (Applied Biophysics). Ultimately it is expected that Ag/AgCl electrodes would be no longer required as measuring with AC enables the use of other (inert) electrode materials like platinum [144].

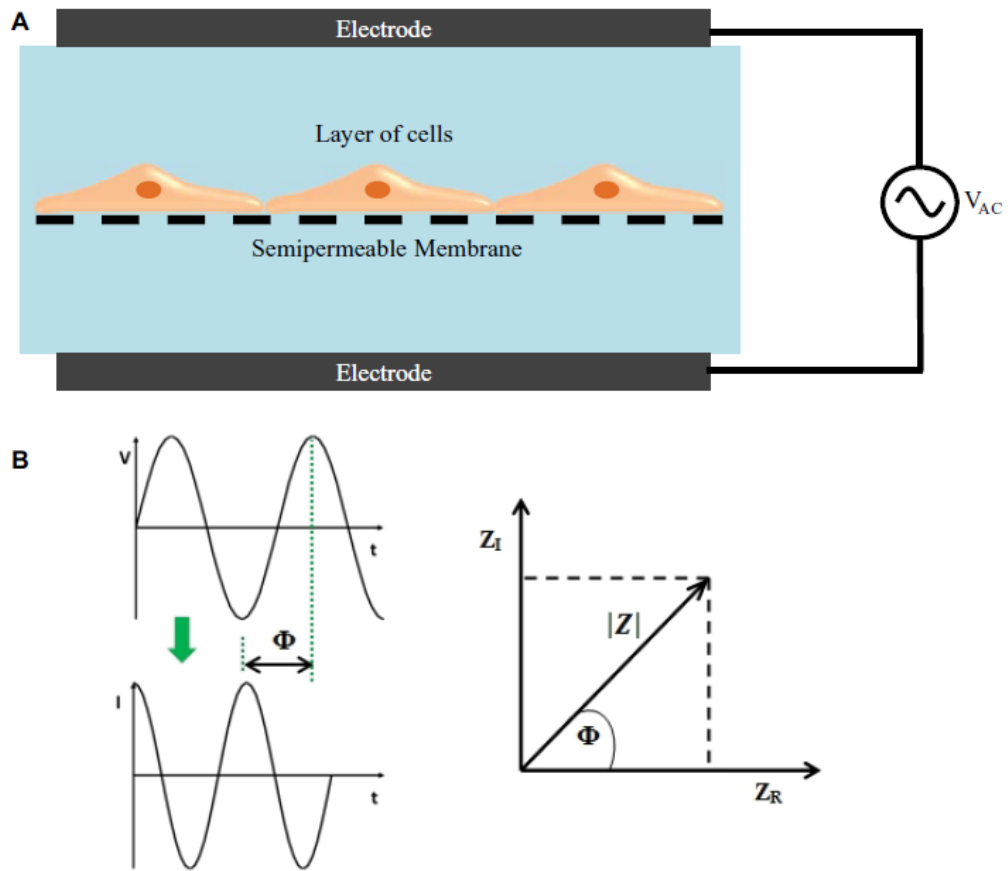


Figure 4.2: (A) TEER measurement concept based on impedance spectroscopy. (B) Components of impedance [3].

Special care needs to be taken if it is used a multimeter to determine the resistance, as the applied voltage to the electrodes can vary significantly among manufacturers, models and also between various resistance measurement ranges. The used voltage can therefore influence the determination of TEER or, in worst case, deplete the Ag/AgCl electrode, leading to measurement errors and cell toxicity due to the release of silver ions [144].

4.2 The measurement procedure and model

Whenever TEER measurements are performed, the procedure includes measuring the blank resistance (R_{BLANK}) of the semipermeable membrane, or of the barrier created on chip, without cells and measuring the resistance across the cell layer (R_{TOTAL}). The baseline level of noise or error in the system may result from recording equipment as well as other variables that could not be perfectly controlled such as temperature fluctuation in the incubator, precise attachment of system to recording equipment, or resistivity of the Dulbecco's Modified Eagle Medium (DMEM) solution. So the blank measurement guarantees to eliminate in part such effects to the TEER value [77].

The cell-specific resistance (R_{TISSUE}), in units of Ω , can be therefore obtained as:

$$R_{TISSUE}(\Omega) = R_{TOTAL} - R_{BLANK} \quad (4.1)$$

where resistance is inversely proportional to the effective area of the semipermeable membrane (M_{AREA}), which is reported in units of cm^2 .

$$R_{TISSUE}(\Omega) \propto \frac{1}{M_{AREA}(cm^2)} \quad (4.2)$$

TEER values are typically reported ($TEER_{REPORTED}$) in units of Ωcm^2 and calculated as:

$$TEER_{REPORTED}(\Omega \cdot cm^2) = R_{TISSUE} \cdot M_{AREA} \quad (4.3)$$

In case it is performed an impedance spectroscopy or an AC measurement, electrical impedance (Z) is obtained in this way:

$$Z = \frac{V(t)}{I(t)} = \frac{V_0 \sin(2\pi ft)}{I_0 \sin(2\pi ft + \phi)} \quad (4.4)$$

where V_0 and I_0 are the peak voltage and current, respectively, f is the frequency, t is the time and ϕ is the phase shift between the voltage and current functions. Z is a complex function, if it is expressed with fasors, that can be written as:

$$Z = Z_R + jZ_I \quad (4.5)$$

The modulus $|Z|$ and the phase shift ϕ fully describe the impedance and its components.

To obtain the electrical parameters from the measured impedance spectrum, and therefore characterize the cellular barrier properties, is made an equivalent circuit

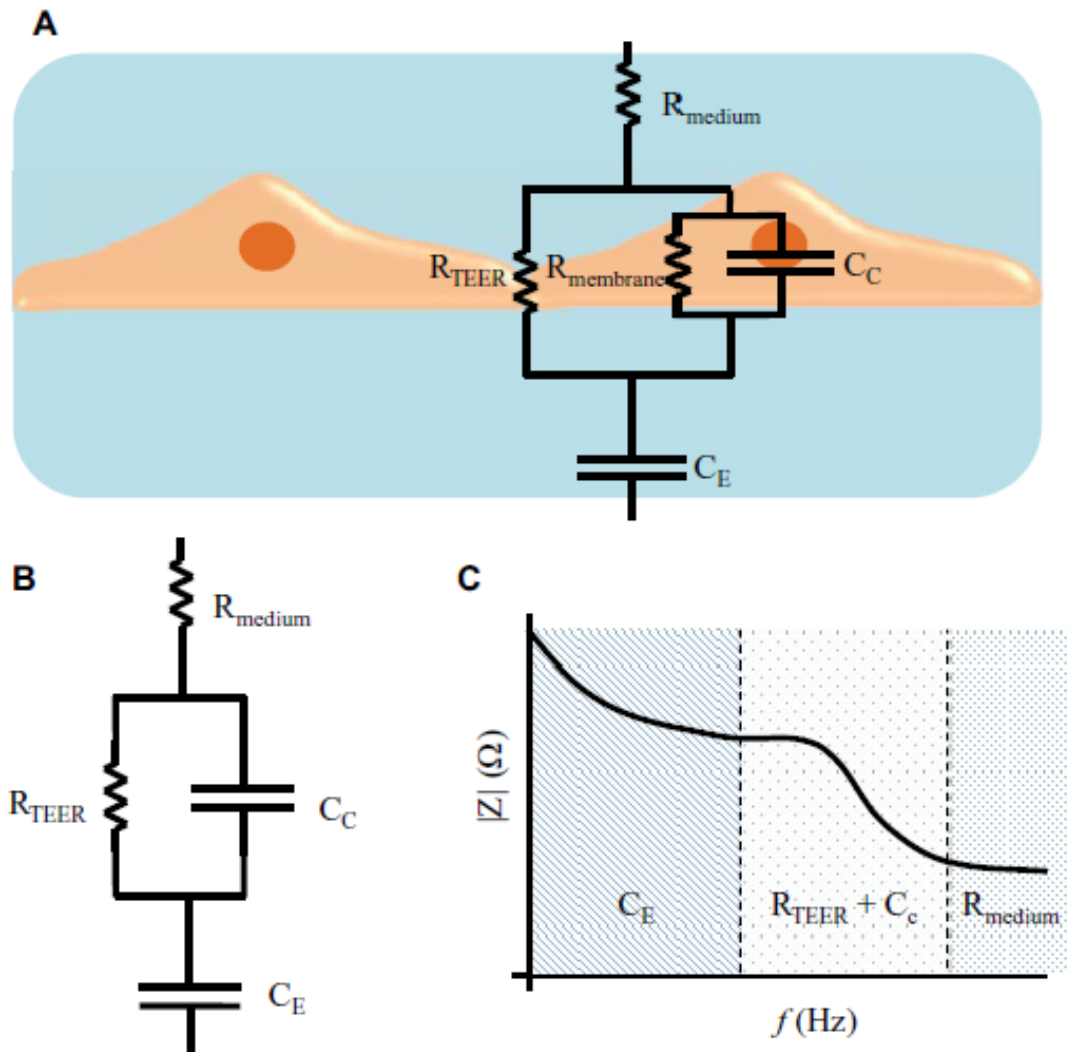


Figure 4.3: (A) A typical equivalent circuit diagram that can be applied to analyze the impedance spectrum of cellular systems. (B) Simplified equivalent circuit. (C) A typical impedance spectrum with distinct frequency-dependent regions (adapted from Benson et al. [145])

analysis like in Figure 4.3 A. As you can see from the equivalent circuit represented, the tight junction proteins in the paracellular route contribute to an ohmic resistance (R_{TEER}). Each lipid bilayer in the transcellular route contributes to a parallel circuit consisting of ohmic resistance ($R_{membrane}$) and an electrical capacitance (C_C). It is moreover included the resistance of the cell culture medium (R_{medium}) and the capacitance of the measurement electrodes (C_E), to be considered if a 2 point probe measurement is performed. Because of the high values of $R_{membrane}$, the current is forced to mostly flow across the capacitor C_C . This allows to neglect $R_{membrane}$ and the lipid bilayers can be represented with just C_C . Based on this approximation, the equivalent circuit diagram can be further simplified as shown in Figure 4.3 B and the impedance spectrum observed will have a nonlinear frequency dependency as shown Figure 4.3 C. In this model, the impedance spectrum can show three distinct frequency regions in which the impedance is dominated by certain equivalent circuit elements. In the low-frequency range, the impedance signal is dominated by C_E . In the midfrequency range, the impedance signal is dominated by circuit elements related to the cells, namely, R_{TEER} and C_C . In the high frequency range, C_C and C_E provide a more conductive path and the impedance signal is dominated by R_{medium} . However these equivalent circuit parameters are not readily available, but they can be estimated by fitting the experimental impedance spectrum data to the equivalent circuit model using nonlinear least-squares fitting techniques to obtain the best fit parameters [3].

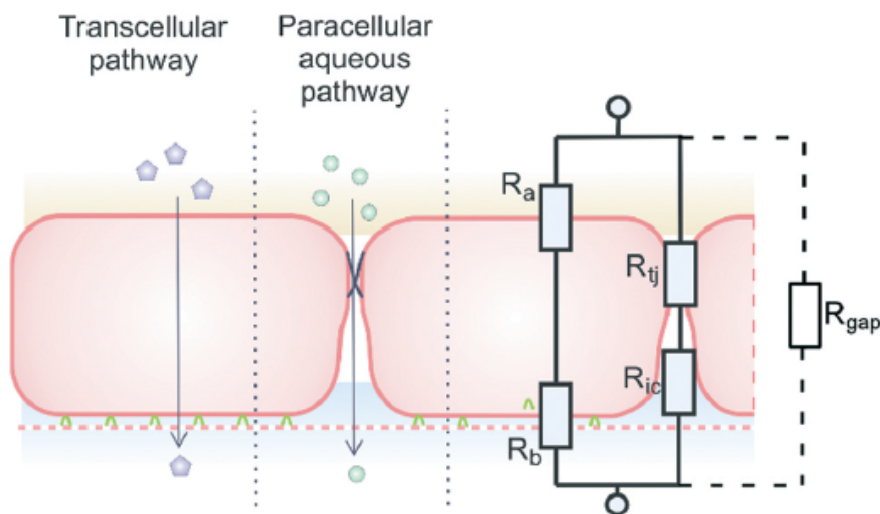


Figure 4.4: Endothelial cell layer forming a barrier. The resistance components are modeled here to include the effect of the paracellular and transcellular pathways [144].

A more detailed schematic model, approaching the problem on another perspective, of a typical tissue barrier consisting of a culture of epithelial or endothelial cells is shown in Figure 4.4. This model is only valid for the transfer of DC signals.

The transported ions and other charged molecules are the charge carriers in the system. The transcellular pathway R_{TC} , is the sum of the apical cell membrane resistance (R_a) and the basolateral cell membrane resistance (R_b). R_{PC} instead depicts the paracellular pathway and is equal to the sum of the tight junction resis-

tance (R_{tj}) and the intercellular resistance (R_{ic}). An extra pathway through a gap resistance (R_{gap}) representing partial cell coverage of the cell support, is included in the Figure 4.4 indicated by the dashed line and will be discussed in more detail in the next sections. Typically, the paracellular pathway is more dominant in the overall TEER, especially at the beginning of the barrier culture when adherent junctions or tight junctions between the cells have not yet formed. Although this simplified model is conceived for DC acquisitions, it still applies for low-frequency AC measurements, such as 12.5 Hz used by commercially available TEER measurement equipments. In this framework, the total TEER is the equivalent resistance of R_{TC} and R_{PC} in parallel [144]:

$$R_{TEER} = \frac{R_{TC} \cdot R_{PC}}{R_{TC} + R_{PC}} \quad (4.6)$$

4.3 Resolving TEER from Circuit Model

As it is said above, in order to obtain the magnitude of TEER from the experimental impedance spectra, it is necessary to make a control measurement before cell seeding. It is afterwards subtracted from the measured experimental impedance spectra, eliminating the effect from electrolyte, membrane, and electrode-electrolyte interfaces, simplifying the analysis.

In order to simulate the cell monolayer electrical behavior before the experiment, it is possible to use an equivalent lumped element circuit model previously analyzed, see Figure 4.3 and Figure 4.4. This circuit may represent the most simplified model considering three components: R_E , R_I , and C_M , representing extracellular (TEER) and intracellular resistances and a membrane capacitance, respectively. Therefore it is used a numerical method fit TEER values in order to obtain the contribution of its components. One of the popular options to handle those data is MATLAB (The MathWorks, Inc., Natick, MA) [77].

TEER values are usually resolved from the impedance spectra taken on each day following seeding using a best-fit circuit algorithm. Data from several studies showed that TEER values increase daily before reaching a plateau and even decreasing slightly [76].

4.4 Factors influencing TEER

Temperature is the first factor that have been shown to affect TEER measurements. Cell cultures usually are maintained at 37°C, therefore ideally TEER measurements should be conducted in an incubator. If TEER measurements are performed at room temperature, instead, it would be necessary to equilibrate the temperature before performing TEER measurements. Otherwise may verify temperature fluctuation, inducing TEER changes. This action, however, could be detrimental to cell physiology and function. Typically, equilibration from 37°C to room temperatures requires at least 20 minutes. A mathematical way out may help to overcome these problems and to allow TEER measurements during cooling or heating. This algorithm correct TEER values for the actual temperature at which they were recorded;

this is referred to as temperature-corrected TEER (tcTEER) [3].

Usually biological studies in different labs differ in many ways, for example because of different origin of cell lines and the different protocols used to maintain these cells in culture. Those differences can affect the process of spontaneous differentiation. For example, in the case of Caco-2 cells, the degree of differentiation achieved with serum-free and serum-reduced media has been studied and related TEER measurements showed such difference [3].

The type of cells have a major influence on the TEER values. Anyway they show large variations in literature, not only between various cell lines but also between different studies with the same cell lines [76].

The age of cells is measured by the passage, i.e., the number of times they are divided and allocated in different flasks to be stored or increase their number. The effect of the passage number of Caco-2 cells on TEER measurements has been studied. TEER values were compared between the early passages of Caco-2 cells (passages in the range 35-47) and later passages of the cells (passages in the range 87-112). It was observed that the TEERs for younger Caco-2 cells ranged from 475 to 700 $\Omega \cdot cm^2$ when compared to elderly Caco-2 cells, which ranged from 1100 to 1500 $\Omega \cdot cm^2$. Another study on the effect of passage number on TEER values has also examined Caco-2 cells from passage 20 through passage 109. It was observed that TEER values increased until passage 36, then the resistance was variable until passage 70, after which there was a decline in TEER value until passage 100 [3].

Cell culture period is another variable of importance when using the Caco-2 cell line or other endothelial lines. The culture period is considered to be important for the formation of a tight junction in these cells. The conventional culture period of Caco-2 cells for transport studies is considered to be 21 days [3, 76].

The most widely used and commercially available TEER measurement system is the EVOM and, as it was said, includes a pair of electrodes known as an STX2/chopstick electrode pair. The position of the STX2 electrodes can introduce variability between measurements if the positioning is not consistent. The introduction of STX2 electrodes into the well under test requires careful handling to prevent any disturbance to the cells under study. This problem can be overcome by the development of integrated microelectrodes within these systems. The positioning of integrated microelectrodes in close proximity to the cellular layer can also reduce the contribution of electrical resistance from cell culture medium and also minimize the signal noise generated by electrode motion [3].

Fluid flow has a potential impact on the readings. Anyway, it is not demonstrated and in our experiment (it will further be examined) such an impact was negligible, because it is several orders of magnitude lower with respect to TEER values found in literature. Shear stress, however, has a mechano-transductive effect on several endothelial molecular pathways through activation of membrane-bound receptors. These pathways stimulate increased gene and protein expression leading to the production of tight junction proteins and they modulate cytoskeletal structure promoting cell reorientation and restructuring. Shear stress can affect the barrier functions of endothelial cells and therefore the TEER values of endothelial cells

under flow conditions [3].

It also has been difficult to compare results obtained with different culture systems, such as Transwell culture inserts versus microfluidic organs-on-chips. When measuring TEER in organ-on-a-chip systems, the confined environment of microfluidic channels results in higher values compared to Transwell. This seemingly higher TEER has a geometrical origin, rather than a biological one. Measurements obtained in microfluidic systems can be compared to those obtained in Transwell systems using the theoretical models that were presented here

The cell coverage over the supporting substrate is also an important factor. Only the slightest gap (0.4%) can reduce the measured TEER significantly (80%). Even if fluorescent staining indicates a good barrier with tight junctions, TEER values might be lower if a small gap is present somewhere in the cell monolayer. It is suspected such small defects in cell coverage are the main cause for large variations in measurements reported in literature [76].

In principle, the TEER parameter describes the quality of the barrier function of a cell layer. Figure 4.5 shows the impact of a small gap in the monolayer due to partial cell coverage. As can be seen from this figure, even a minor defect in monolayer confluency will have a major impact on the measured TEER. For example, at 99.6% cell coverage the measured TEER value will be 80% lower than the TEER of a culture with full cell coverage. The effects of cell coverage are of particular importance in microfluidic systems because of the relatively small surface area as well as the decreased effective surface area due to the unequal current distribution [144].

Moreover dynamic impedance changes in response to chemical or protein treatment. In fact the impedance of the entire system decreased significantly, in the work described in [77], at all frequency points following treatment with TritonX-100 (Figure 4.6.). This decrease varied from $161.51 \pm 0.755 \Omega \cdot \text{cm}^2$ to $39.73 \pm 1.925 \Omega \cdot \text{cm}^2$. Furthermore, also a change in the impedance at all frequency points following trypsinization was demonstrated. Thus a TEER measurement can detect changes in response to chemical or protein treatment in real time thanks to the decrease in impedance amplitude [76, 144]. This actually allows to trace also changes in tight junctions permeability.

The physical support that is used for cell culture is another factor of influence, as well as the material, quality and surface state of the electrodes [144]. Judging from the discussion made it is sure that TEER is an useful technique to investigate several barrier features, however it is apparent that they also show large variance, that does not allow to quantitatively compare specific barrier tightness in a reproducible and standardized manner.

For Caco-2 monolayer TEER varies between 150 and $400 \Omega \cdot \text{cm}^2$. Table 4.1 shows a range of some of the TEER values reported for gastrointestinal tract models. It has been discussed the problem of comparing TEER data across laboratories, suggesting that determining the permeability coefficients for substances may provide a more accurate basis for cross-laboratory comparison [146]. In addition, including

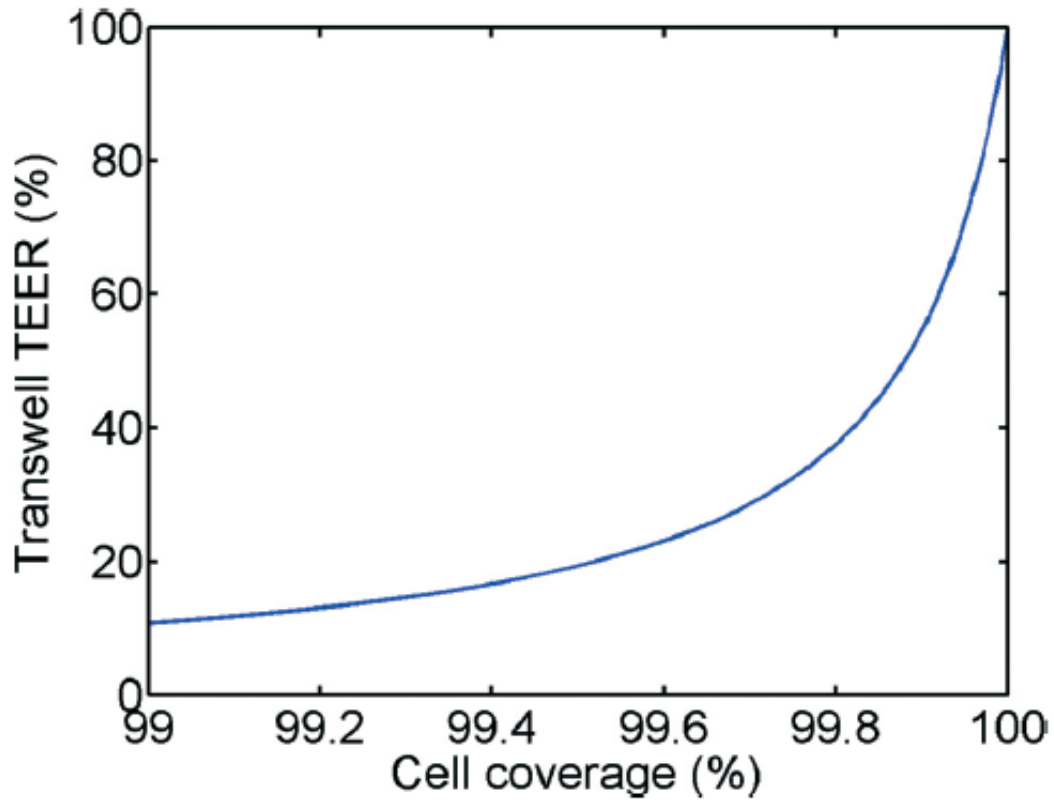


Figure 4.5: TEER dependence on the cell coverage [144]

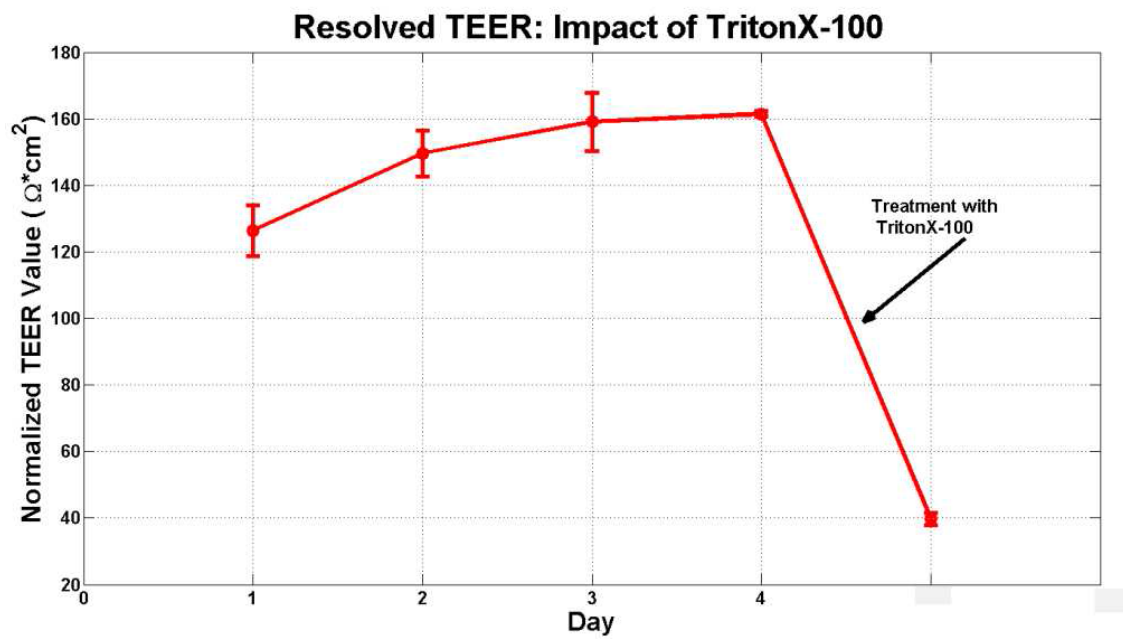


Figure 4.6: Effect of TritonX-100 on the TEER measurement [77]

Table 4.1: Examples of TEER values for gastrointestinal cell lines [3].

Cell Type Used in In Vitro Model	TEER ($\Omega \cdot \text{cm}^2$)	Equipment Used
Gastric mucosa (in vivo)	2000	Ussing chambers
Colon (in vivo)	300–400	Ussing chambers
Small intestine (in vivo)	50–100	Ussing chambers
Human epithelial colorectal adenocarcinoma cells (Caco-2)	1100–1350	Millicell-ERS system
Caco-2/TC7	711±79	Millicell-ERS/EndOhm chamber
Rat small intestinal (IEC-18)	100	Millicell-ERS system
Human immortalized colon cell line (HCEC)	200	Millicell-ERS system
Caco-2	1400–2400	EVOM/chopstick
Caco-2	763±287	EVOM/EndOhm
Caco-2 and HT29-MTX	110–185	EVOM/chopstick
HT29-MTX	25	EVOM/EndOhm
MDCK	1500	Impedance analyzer/Ag electrodes
Caco-2	250	Millicell-ERS system
Caco-2 amd HT29-MTX	122±19	Millicell-ERS system
Caco-2 amd HT29-MTX	100–300	Millicell-ERS system
Caco-2 and Raji B	285±76	Millicell-ERS/EndOhm
Caco-2 and Raji B	88±27	Millicell-ERS system
Caco-2, HT29, and Raji B	60±17	Millicell-ERS system
Caco-2	3000–4000	Voltage-ohm meter/Ag electrodes

other cell types into the model, such as mucus-producing goblet cells, has the potential to decrease TEER values, which may make the model more physiological. Gastrointestinal epithelia are classified based on TEER values as "tight" indicated by values of about $2000 \Omega \cdot \text{cm}^2$, as "intermediate" indicated by values in the range of $300\text{--}400 \Omega \cdot \text{cm}^2$, and as "leaky" indicated by values of $50\text{--}100 \Omega \cdot \text{cm}^2$ [3].

4.5 Comparison between 2 points measurements and 4 points measurements

Supposing to wish to measure the resistance of some component located a significant distance away from our ohmmeter, could result in a problematic situation. Indeed if the ohmmeter is connected directly the component being measured ($R_{subject}$), it measures all resistance in the circuit loop, which includes the resistance of the wires (R_{wire}) connecting the ohmmeter to $R_{subject}$ and a contact resistance. Although wire resistance is very small, a substantial error may be introduced, particularly if the connecting wires are very long or the component to be measured has a very low resistance. Such configuration is known as 2-point probes. 4-point probes method, instead, is an electrical impedance measuring technique that uses separate pairs of current-carrying and voltage-sensing electrodes to make more accurate measurements. Separation of current and voltage electrodes eliminates the lead and contact resistance from the measurement, but also electrodes polarization. This makes the measurements independent from such effects [147] and is an advantage for precise measurement of low resistance values. Four-terminal sensing is also known as Kelvin sensing. When a Kelvin connection is used, current is supplied via a pair of source connections (current leads). These generate a voltage drop across the impedance to be measured according to Ohm's law. A pair of sense connections (voltage leads)

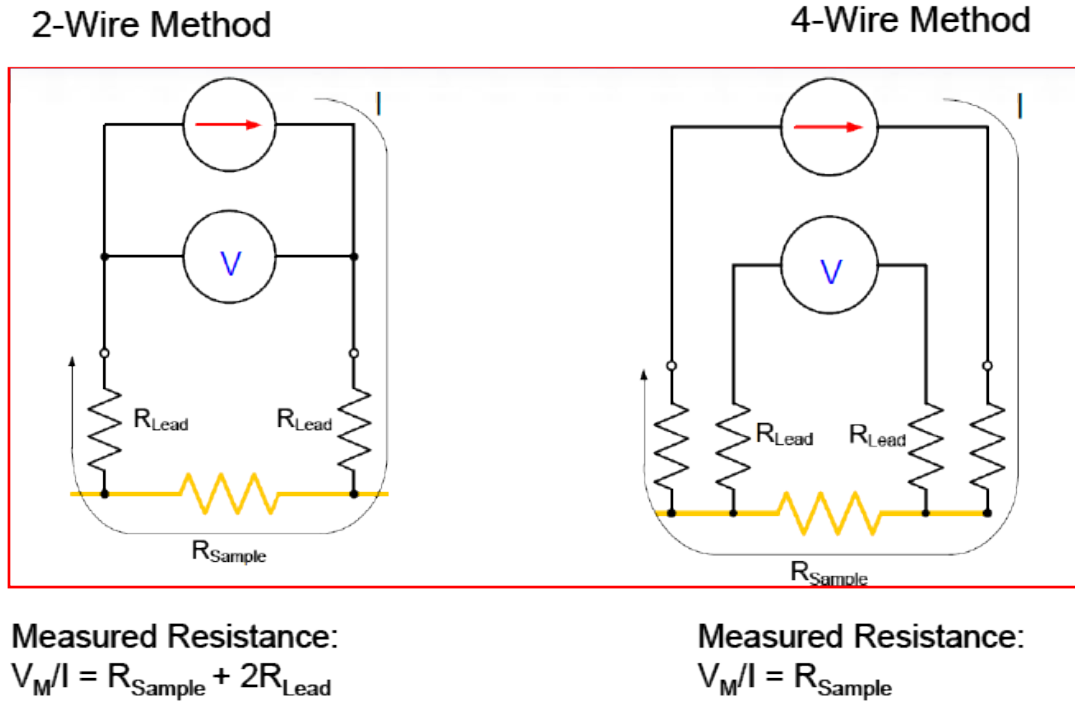


Figure 4.7: Comparison between 2-point probe method and 4-point probe one, showing how the measurement is simplified. [147]

are made immediately adjacent to the target impedance, so that they do not include the voltage drop in the force leads or contacts. Since almost no current flows to the measuring instrument, the voltage drop in the sense leads is negligible.

It is usual to arrange the sense wires as the inside pair, while the force wires are the outside pair. If the force and sense connections are exchanged, accuracy can be affected, because more of the lead resistance is included in the measurement.

Chapter 5

Materials and Methods

Due to several considerations related to the previous topic discussed, it was designed a microfluidic system that reassemble a physiological environment, providing as a support a biologically derived hydrogel. Cells are seeded in one of the inner channels. The elastic nature of the hydrogel allow to provide also mechanical stresses when it is subjected to a flow. It was designed and calibrated the pump for this specific system, studying, thanks to Poiseulle's model, the right flow rate to provide a shear stress that could stimulate Caco-2 cells differentiation. The device can support 4 electrodes to analyze the TEER. Cell growth and seeding was studied and analyzed also with imaging techniques, exploiting traditional barrier integrity assays.

5.1 Hydrogel Preparation



Figure 5.1: Hydrogel core.

The core of the device is composed by a gelatin hydrogel with two empty channels. The hydrogel used is composed by gelatin hydrogel, crosslinked with microbial transglutaminase. This choice is due to the thermo-reversibility of the hydrogel,

at $\sim 20^\circ\text{C}$, indeed, the hydrogel physical state is liquid, while the temperature decrease promotes physical crosslinking. There are actually different proteins that can crosslink the gelatin. The choice of the transgluteminase anyway was due to the costs, the biocompatibility, in addition to the crosslinking temperature range and time in which the process acts. The increase of transgluteminase (mTrans) concentration encourage the increase of crosslinking velocity and stiffness.

Considering a constant concentration of gel, in terms of mass percentage per 100 mL (w/v), it is possible to fix a certain target of enzyme unity per gel weight. This allows to compute how much mTrans should be used and the volume in which it has to be dissolved. The mentioned target is related to the stiffness, determined by the unity (U) of enzyme per gel grams, and depends on the enzyme activity. The enzyme activity is a measure of the quantity of active enzyme present and is defined as the moles of substrate converted per unit time, i.e. rate per reaction volume. The SI unit to specify it is the katal, that is $1\text{katal} = 1\text{mol/s}$. Anyway, it can be also described a units where 1 U corresponds to 16.67 nanokatals [148]

- In our case the target is: $50U_{enzyme}/g_{gel}$
- The enzyme activity instead is: $100 U/g_{enzyme}$
- The initial concentration of gel: $7.5\%w/v$
- The final concentration of gel: $5\%w/v$

Given the data above and imposing the final volume of gel (concentrated at $5\% w/v$) we can obtain the volume of gel that should be taken from the batch (concentrated at $7.5\% w/v$) thanks to the formula:

$$C_1V_1 = C_2V_2 \quad (5.1)$$

The difference between V_1 and V_2 is the volume of solution of mTrans to add to V_1 . The units of enzyme x are determined by the target imposed and the actual grams of gel in the batch at $7.5\% w/v$:

$$x : g_{initial} = U_{target} : g_{gel} = 50U_{enzyme}/g_{gel} \quad (5.2)$$

Such amount of enzyme units has to be diluted in the volume of Phosphate-buffered saline (PBS) $V_{PBS} = V_1 - V_2$. The concentration of enzyme units in V_{PBS} is:

$$c_{enzyme} = x/V_{PBS} \quad (5.3)$$

Thus it is possible to compute the enzyme mass to be duluited in V_{PBS} , in order to obtain V_2 of gel with a certain stiffness, considering the enzyme activity A_{enzyme} :

$$m_{enzyme} = \frac{c_{enzyme} \cdot V_{PBS}}{A_{enzyme}} \quad (5.4)$$

That actually can be written as:

$$m_{enzyme} = \frac{x}{A_{enzyme}} \quad (5.5)$$

From the calculations results that, in any case, the proportion of solution and gelatin is $\sim 1:2$. At first the target was $100U_{enzyme}/g_{gel}$, thus the amount of enzyme in 15 mL of PBS was 2.25 mg.

The solution used for the fabrication of the inner channels ended up being a sacrificial one, using commercially available PVA channels. Those channels are fabricated thanks to FDM technique using the Felix 3 (Felix Printers, IJsselstein, The Netherlands) printer with a nozzle diameter of 250 μm . The printing settings imposed were:

1. Nozzle temperature for PVA: 200 /*degree*C
2. Bed temperature: 55 °C
3. Layer thickness: 100 μm
4. Extrusion width: 300 μm

The sacrificial templates and molds were designed and converted into STL files using CAD software (computer aided design, Dassault Systemes SolidWorks Corporation, US). All STL files were processed by KISSlicer [149] software and sliced to generate G-code instructions for the 3D printer. G-code instruction sets were sent to the printer using Repetier-host [150], an open-source 3D printer host program. The use of 3D printing allows to have a dynamic design, thus any change was ready to make anytime.

5.2 Fluidic mold design and fabrication

The fluidic mold has the aim of hosting the hydrogel core, granting a stable connection with the fluidic apparatus using its higher stiffness with respect to the gelatin. Moreover it allows to control the distance between the inner channels in the hydrogel casting step. The component is manufactured casting flexible clear polydimethylsiloxane (PDMS, Sylgard 184, Dow Corning Corporation) polymer within a 3D printed mold. A PVA mold, that defines the internal chamber, is screwed together to this mold also. This chamber has dimensions: 18 mm x 14 mm x 9 mm. Four hub-free stainless steel blunt needles (18G; Kimble Chase, Vineland, NJ) were used to define the fluidic connections, and four solid stainless steel needle electrodes (Neuroline Monopolar (74325-36/40), Ambu) were used to create the electrode guides. All these components are inserted in the PVA mold in order to assure the connection with the outer environment. The electrodes were made with stainless steel and had an external diameter of 350 μm . 3D printed mold components, in turn, were fabricated with a sthereolithography technique, using Form 2 SLA 3D printer (Formlabs, Somerville, Massachusetts, USA). The photocurable resin employed in this study were: GPCL02 clear resin and GPWH02 white resin (Formlabs, Somerville, Massachusetts, USA). The resin that was used was stable at 70 °C, the operating temperature for the crosslinking of the PDMS. There were

not chemical interactions between the resin and the PDMS that could damage the biocompatibility of the device. It is actually very important the post processing of the mold indeed: the printed components are not completely crosslinked and usually there is resin in excess. Therefore, once the printing is finished, the pieces must be completely immersed in isopropanol twice for 15 minutes, in order to be sure to discard the resin in excess accumulated and not crosslinked. Afterwards the parts should be dried and the crosslinking process on the surfaces is improved with a UV lamp, although may be helpful also the sunlight. Other processes are possible, but they may bent the printed parts or obtain non-good-looking surfaces.

The 3D printed mold was composed by three parts: one upper part and two bottom parts that were screwed together allowing an easy demolding. The PDMS had a 1:10 w/w part of curing agent in order to have a quite stiff device. Once the curing agent was mixed with the PDMS, silicon was both degassed before and after the molding step. This allowed to have a more homogeneous device, as a matter of fact the trapped bubbles could escape from the mold thanks to several attendant holes in the mold upper part during the degassing process.

Anyway an important drawback of the PDMS chamber is the hydrophobicity of the material. In fact it does not allow the gelatin to bound with the surface. the gelatin, though, needs to stick with the walls in order to have enough stability, otherwise following steps of the fabrication and the connection with peristaltic pumps would not be feseable. That is why all the PDMS chambers, at the beginning of every experiment, were treated with oxygen plasma (125 W, 13.5 MHz, 50 sccm, and 40 millitorr), making the surfaces of the chambers hydrophilic. The RF plasma indeed can ionize the surface and create unbounded orbitals, making the surface hydrophilic. On the contrary it would not be possible neither the passages of the fabrication process nor the normal use of the device. The mold was subsequently sterilized with a bath in ethanol for 1 hour.

The design of the PDMS chamber has anyway evolved firstly in order to control the distance between the electrodes and also improve their stability. Moreover the inner chamber dimensions were changed in order to assure more material above the channels, thus preventing the risk of gelatin break in correspondence of the channel. Moreover the shape helps the device handling, especially at the time of the casting step. To avoid undesired movements that could cause changes in the recorder electrical measurements, the electrodes had to be positioned at the same location every time. Therefore, the 3D printed mold was designed to precisely allocate the four electrodes (Figure 5.2B). Moreover the PDMS chamber was designed so the electrodes could reach at most the axis of symmetry of the bulk.

5.3 Fluidic platform

The connection with the fluidics for a device that simulates an intestine is a necessary step to gain a more physiological environment. In fact peristaltic movements demonstrated to make Caco-2 cells produce mucus and have villi differentiation [64]. Moreover it can be used to automate the dissolution of PVA in the fabrication process. In order to connect the devices with the fluidics, it was designed a platform

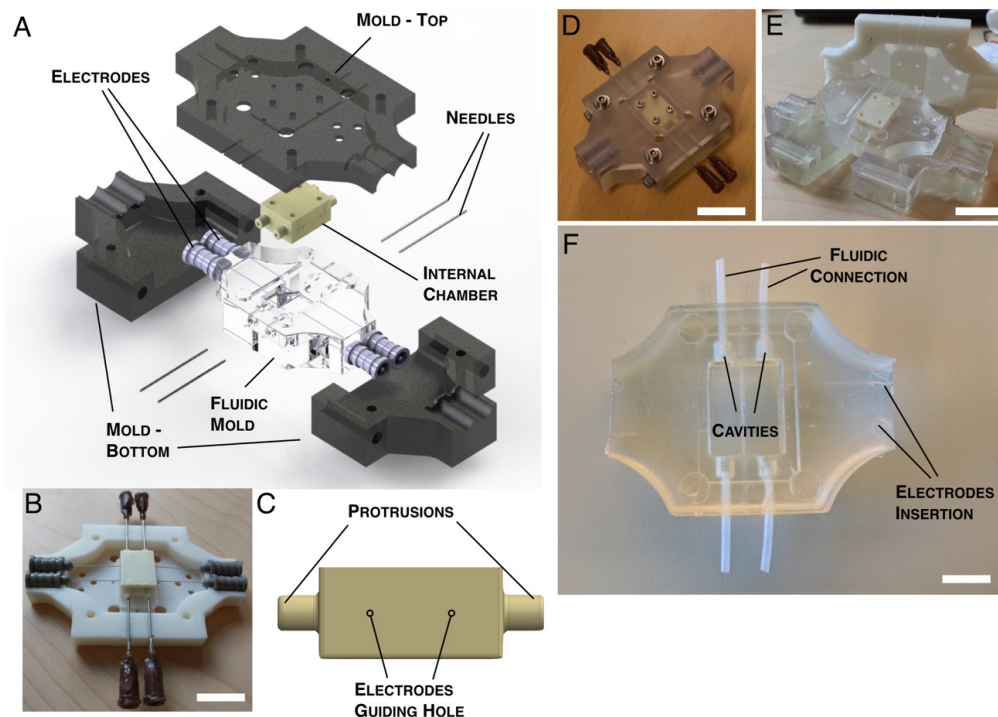


Figure 5.2: (A) Designed mold used for the fabrication of the fluidic mold. The mold consisted in three external parts responsible for defining the external surface of the fluidic mold while the internal chamber was designed and 3D printed in PVA to include the final cavities and the guides for the electrodes insertion. (B) Photograph of the top part of the mold mounted with the PVA structure responsible for defining the internal chamber with the four electrodes in position and four needles responsible for defining the fluidic connections. (Scale bar: 2.5 cm) (C) CAD Designed of the part responsible for defining the internal chamber depicting the guides used to control the insertion and final position of the electrodes. (Scale bar: 4 cm) (D) Photograph of the mounted mold with screws and electrodes in place prior the casting of the PDMS used for the fabrication of the fluidic mold. (Scale bar: 3.5 cm) (E) Photograph of the de-molded mold revealing the fabricated fluidic mold before the dissolution of the 3D printed PVA structure responsible for defining the internal chamber. (F) Photograph of the fabricated fluidic mold after the demold process and dissolution of the PVA printed part (Scale bar: 2.2 cm).

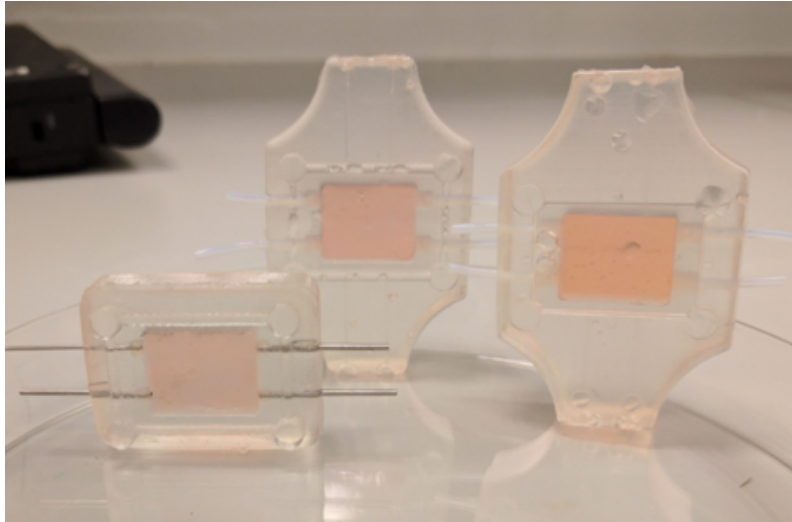


Figure 5.3: The three different designs implemented.

Table 5.1: Summary of the data acquired during the first part of the calibration. The mean of flow rates computed for each channel "ch" is reported. It is also showed the mean of the flow rates of those channels and the respective standard deviation.

RPM	Mean of Ch1	Mean of Ch3	Mean of Ch3	Mean of Ch4	Mean of 4 channels	Standard Deviation
5	3.06	3.1	3.54	3.63333	3.33333	0.29545
10	9.73333	9.66667	8.29333	9.93333	9.48167	0.79889
15	16.38	15.89333	14.33333	15.44667	15.515	0.87634
20	20.68667	21.08	19.38	20.36667	20.37833	0.72668
30	30.68	30.64	28.98667	30.81333	30.28	0.86540
50	51.14667	51.73333	44.25333	52.94	50.01833	3.91517
75	76.99333	77.12667	76.12667	77.56667	76.95333	0.60310
100	103.48	103.03333	96.92	103.86	101.82333	3.28630

that could host an electric motor and its control board, an Arduino microcontroller (Arduino, Italy) and an easydriver stepper motor driver (Brian Schmalz, Creative Commons Attribution 3.0 United States License), vials for the liquid sources and the samples. The platform was designed in Solidwork and printed, thanks to g-code made with KISSlicer, printing with Felix 3 using PLA filament. The stepper motor runs the four peristaltic pumps and can be controlled with a computer interface trough a micro-USB. The software indeed can manage the RPMs of the motor, but obviously this information per se does not bring any clue about the amount of volume pumped per minute. That is why a calibration was needed.

The calibration was performed using water a source and the volume of water pumped was sampled each 5 minutes at different RPMs. The water at the outlet was collected and weighted. Thus considering the water density ρ equal to $1g/cm^3$ it was possible to compute the flow rate, in terms of $\mu l/min$, per each pump (it is also referred to them as channels). Per each channel and RPM value were made 3 tests, thus the values in the table below are related to the mean over the three tests of the flow rates computed.

The scope of this first part of the calibration was to compute the regression line

Table 5.2: Summary of the data acquired during the second part of the calibration. For theoretical flow is meant the flux imposed to the pumps using the regression line computed previously.

Theoretical value	Mean of Ch1	Mean of Ch3	Mean of Ch3	Mean of Ch4	Mean of 4 channels	Standard Deviation
5	3.34667	2.8	2.54667	3.15333	2.96167	0.35745
10	8.3	8.81333	7.37333	8.94	8.35667	0.71156
15	13.94667	14.58	13.40667	12.98667	13.73	0.68957
20	18.04	17.96667	16.66	17.88667	17.63833	0.65522
30	26.98	27.86667	26.51333	26.65333	27.00333	0.607862
50	46.19333	46.41333	43.52	46.12667	45.56333	1.36772
75	67.50667	68.28	63.88	68.77333	67.11	2.21553
100	88.72	91.16	83.61333	89.38	88.21833	3.23834

with Excel (Windows Microsoft Excel), allowing therefore to convert the RPMs to $\mu L/min$. The regression line resulted to be:

$$flowrate = 1.0287 \cdot RPM - 0.7462 \quad (5.6)$$

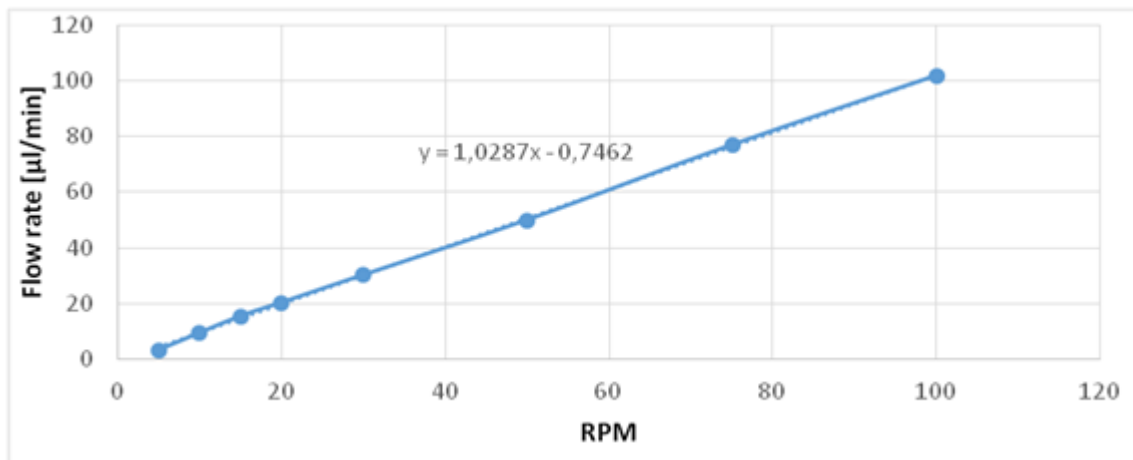


Figure 5.4: Result of the first part of the calibration. The relation between the flow rate and the RPMs imposed by the pumps is almost linear. It is reported also the regression line, to have an approximation of such relation.

Thus in order to verify and eventually correct this rule a second part of the calibration was performed: imposing a certain flow rate we should have collected the same amount at the outlet.

In order to compare the theoretical flow rate and the flow obtained, it was made a Bland and Altman plot, a graphic way to study the statistical error comparing a reference value and the data obtained [151].



Figure 5.5: Bland and Altman plot for comparing the results of the pump calibration

The graph shows that the error is cumulative and it increases as the imposed theoretical flow increases, so the RPMs. Therefore for low regime the error is around 0 $\mu\text{L}/\text{min}$, while for a theoretical value of 100 $\mu\text{L}/\text{min}$, that is ~ 95 RPMs using 2, is around 10 $\mu\text{L}/\text{min}$. This coherence grants to correct the error with the software.

The fluidic molds were tested using the fluidic platform. Deciding the flow rate to apply taking into account the behavior of the fluid, using Navier-Stokes equation, and the possible effects of the shear stress to seeded cells. Considering the dimensions of the channels and their geometry, actually, it was better suited the Poiseuille law.

The premise for the Navier-Stokes equation is that the fluids used are incompressible and Newtonian, thus the viscosity μ is constant. There are several examples of Newtonian fluids applied in organs-on-a-chip, including water-based fluorescent dyes [152], dilute cell medium [153], , dilute solutions of growth factors [154], proteins [155] and medical drugs. Navier-Stokes equation balances the rate of change in fluid momentum with the convective, viscous, and pressure forces, and other externally applied forces.

$$\rho \frac{\partial \mathbf{v}}{\partial t} = -\rho(\mathbf{v} \cdot \nabla \mathbf{v}) - \Delta \mathbf{p} + \mu \Delta \mathbf{v} + \mathbf{G} \quad (5.7)$$

In the absence of externally applied forces (such as electrical or gravitational forces) the force term \mathbf{G} is omitted from the equation Equation 5.7. In our case, considering that the fluid flows in a microfluidic system, gravitational force is negligible. The turbulence of a flow is characterized by Reynold's number, Re . This number is a dimensionless quantity that measures the relation between inertial ($\rho \bar{v}^2$)

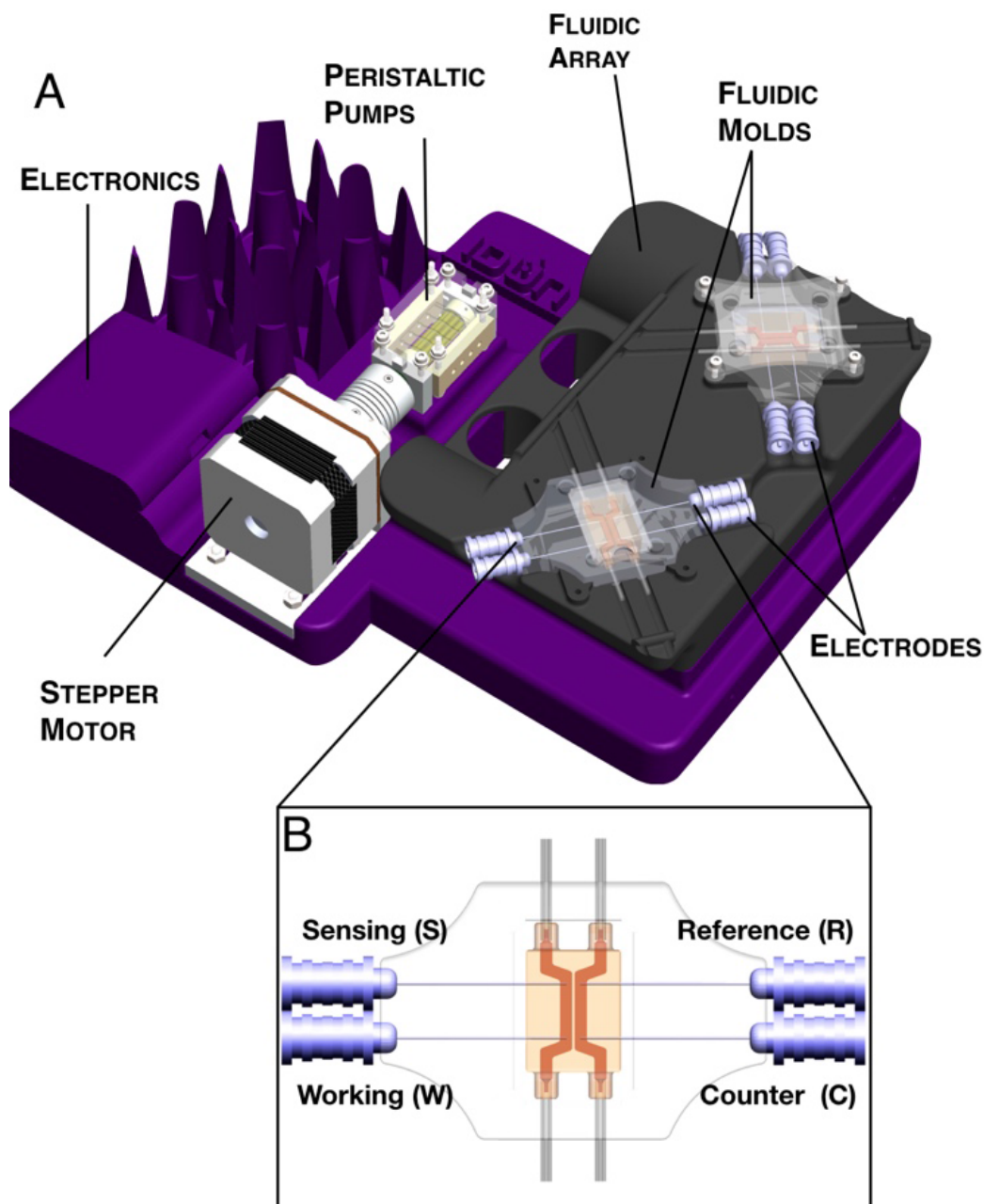


Figure 5.6: (A) Designed fluidic platform. (B) Designed hydrogel-based fluidic system with the schematic of the four-terminal sensing configuration used for impedance measurements.

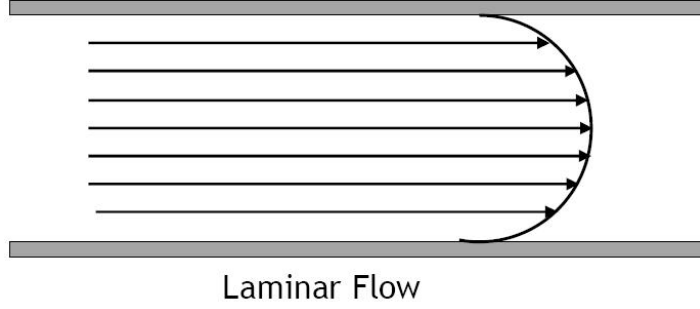


Figure 5.7: Scheme of the velocity profile of a laminar flow [156].

and viscous forces ($\frac{\mu\bar{v}}{L}$) and is defined as:

$$Re = \frac{\rho\bar{v}^2}{\frac{\mu\bar{v}}{L}} = \frac{\rho \cdot \bar{v} \cdot L}{\mu} \quad (5.8)$$

where ρ is the fluid density, \bar{v} is the mean fluid velocity, and L is the characteristic length of the fluidic channel. The mean velocity \bar{v} may be determined both from the volumetric flow rate equation (Equation 5.9), taking into account that the channel crosssectional area is A , and from Navier-Stokes equation.

$$Q = \bar{\mathbf{v}} \cdot \mathbf{A} \quad (5.9)$$

The characteristic length depends on the geometry of the channel and can be easily determined by the ratio between its volume and crosssectional area. In general, however, a flow is considered laminar when Re is smaller than $2.3 \cdot 10^3$. In our system, considering that the medium has a density of 1 g/cm^3 and a viscosity of $0.001 \text{ Pa} \cdot \text{s}$, the channel radius R can be approximated to 1 cm and imposing a flow rate of $65 \mu \text{ L/min}$, the Reynold number is ~ 34 .

In pure diffusion state the viscous forces are dominant over convective forces, thus the convective term is omitted from Navier-Stokes equation, simplifying it:

$$\rho \frac{\partial \mathbf{v}}{\partial t} = -\Delta \mathbf{p} + \mu \Delta \mathbf{v} \quad (5.10)$$

The pressure drop along the channel length occurs along the flow direction, imposing it to be along the x -axis. The velocity profile, v , does not change along such axis because resistive effects are neglected, anyway it varies along the y and z direction, thus $v = v(y, z)$. In steady state condition and in the 2D approach, the velocity profile results to be parabolic and, with polar coordinates, it can be expressed as:

$$\mathbf{v}(r) = -\frac{\Delta \mathbf{p}}{4\mu L}(r^2 - R^2) \quad (5.11)$$

In order to apply the Poiseuille law some assumptions should be added: the first is that the walls of the channels are stiff and uniform, secondly the flow is laminar and there is no slip at the walls, which means that at such interface the velocity is zero. So it is possible to compute the pressure drop with Poiseuille law as:

$$\frac{\Delta p}{L} = \frac{Q \cdot 8\mu}{\pi R^4} \quad (5.12)$$

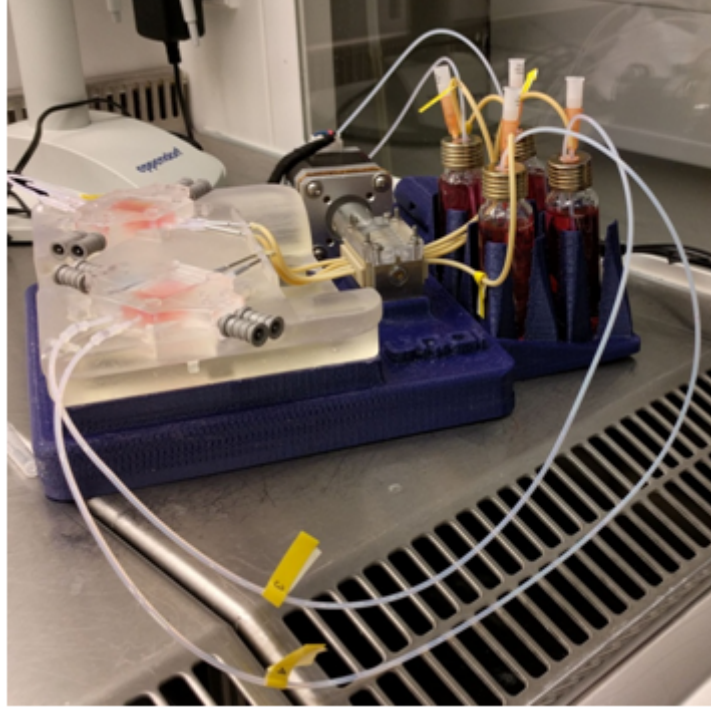


Figure 5.8: Fluidic platform connected with the device during a microfluidic test.

Taking into account Equation 5.9 the mean velocity results:

$$\bar{v} = v(0) = \frac{\Delta p R^2}{4\mu} \quad (5.13)$$

During the biological experiments, the presence of a flow field introduces shear stresses to biological cells residing on the bed of the fluidic channel. Therefore, microfluidic devices have to be designed to provide cells with a physiologically relevant shear flow microenvironment. The maximum shear stress, τ_{max} , occurs at the microchannel walls and can be determined as [157]:

$$\tau_{max} = \frac{4\mu Q}{\pi R^3} \quad (5.14)$$

To design the system, the shear stress imposed to the cells it is imposed at 0.02 dyne/cm^2 . An important part of this fluidic apparatus is the piping system. A wrong assembly may impede the normal flow imposed. This may bring to the failure of the devices due to overpressure, breaking the gel or exposing it to contamination. The piping system was based on PTFE tubing (inner diameter of 0.8 mm) (BOLA 1818-10, Bohlender GmbH, Germany), and PDMS ones with inner diameter of 1.3mm.

The sterilization of the system was made autoclaving all the removable components, such as vials, tubes, metal pins and vials caps. For the fluidic platform a feasible way to sterilize the external surfaces was to clean with ethanol. To assure the sterilization, and also to clean the tubes of the pumps, the system was closed and, activating the motor, 0.5 M sodium hydroxide was flushed. It is a good choice to remove residue of sodium hydroxide flushing with PBS because it can be dangerous for cells.

5.4 Device fabrication, sensor integration and testing

Here are explained the steps, non necessarily consecutive, of the samples preparation: The gelatin hydrogel were prepared in a laminar flow bench (LAF). It was added to gel solution a 0.5% of chloroform to be sure that it was sterile. Before the use the chloroform had to evaporate for biocompatibility.

The PDMS chamber and teflon tubes had to be treated with oxigen plasma to assure the hydrophilicity of the surface. Obviously, also the PVA channels had to be sterilized. Therefore, they were immersed in chloroform in the LAF bench. In order to have a better handling of the PVA channels and for biocompatibility the chloroform needed to evaporate. The PDMS molds, instead, were sterilized in ethanol for 1 hour, so that the plasma treatment in this way would not be affected. Anyway, any trace of ethanol were washed in steril water. PMMA lids, used to lock the gelatin from the outer environment, were washed in sodium hydroxide dilutions and then several times in water. After these washing steps the leads were dried.

Teflon tubes were inserted in the PDMS chamber after being dried, so PVA channels could be embed in the teflon tubes. In this way teflon tubes sustained PVA channels and dissolved PVA had a low resistive conduction with the outer environment. Thus leaks were avoided and therefore the risk of failure was lowered.

Teflon tubes were filled with water so the PVA started to dissolve and acted as a glue, stabilizing the channels. Just before the casting, the gel was mixed with sterilized mTrans solution and casted in the chamber. After 3 minutes, the device was sealed in a Petri dish filled with water and put in a fridge at 4°C for half a hour. At this point the physical crosslinking was promoted while, on the other hand, the diffusion of water in the PVA was not, allowing the PVA to mantain its stability and avoiding an unwanted shrink of the channels. The device was afterwards left at room temperature for half an hour. The increase of temperature promoted the chemical crosslinking and the diffusion of water in PVA. Such diffusion could lead to an increase of the channel dimension because PVA itself could hinder the flowing of dissolved PVA and water. Then the PVA could be washed away gently with a syringe or with a pump and covered with PMMA leads. The system was put in an incubator at 37°C and 5% CO₂ to fully finalize the chemical crosslinking of the gelatin ensuring mechanical stability at higher temperatures.

Each of these passages is very important for the success of the device, mechanically and biologically speaking.

When the devices were made for TEER readings, it is necessary to add another step to the described ones. The insertion of the electrodes after the casting indeed could damage the gel, most likely, if there was a repeated stress. What is sure is that the extraction and subsequently insertion could cause the formation of bubbles, event that is unwanted because such bubbles could interfere with the measurements. The PVA channels in fact were provided with little guides for the insertion of the tip of the electrodes. In this way the respective position of the electrodes and channels was fixed with little variations. Moreover, this feature assured that the tips of the electrodes were inside the channels. On the other hand, the electrode insertion assured PVA channels sustaining and channels parallelism.

Failure, most commonly, arised from a not successful plasma treatment, but also

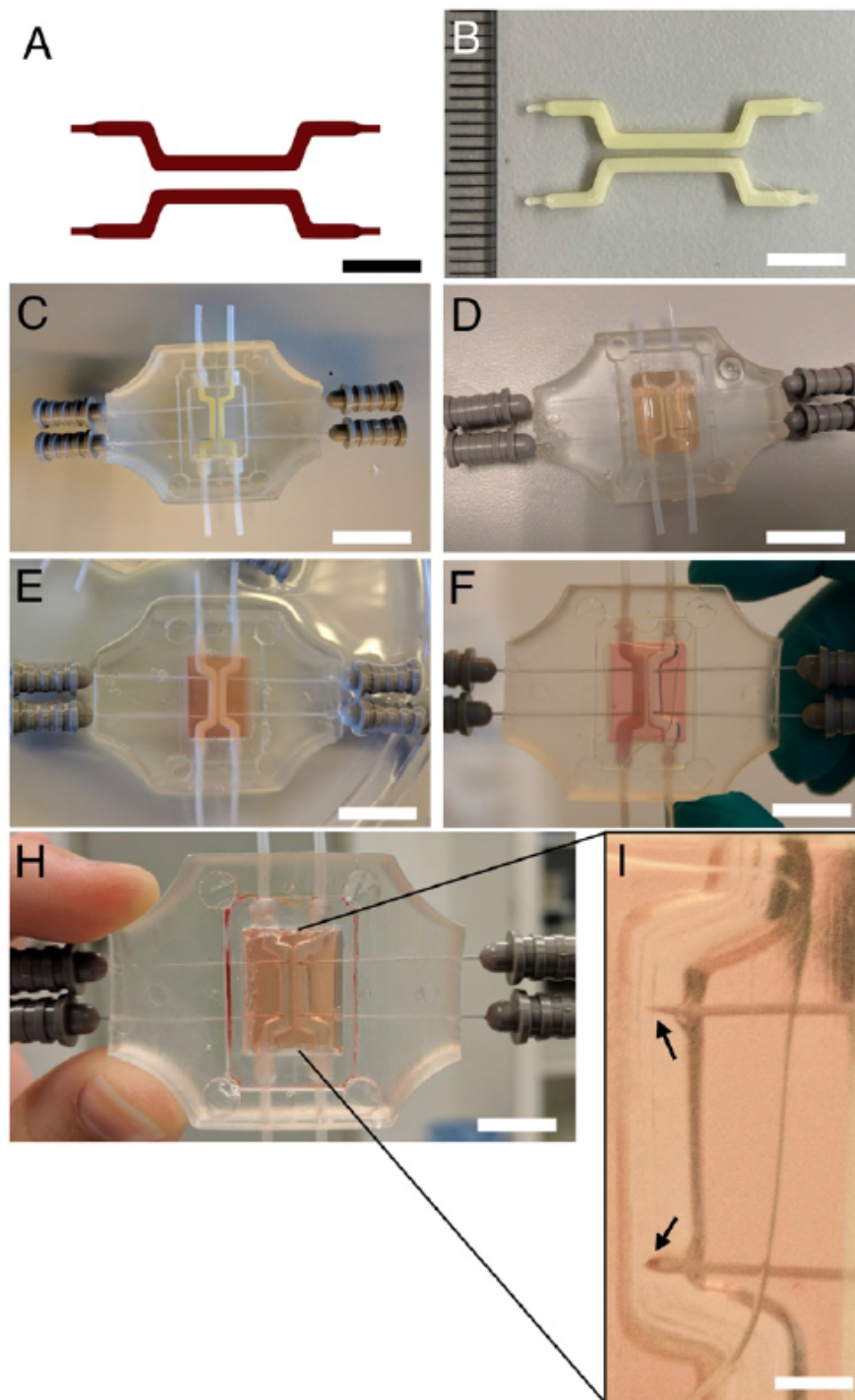


Figure 5.9: (A-B) Designed model and photograph of the two 3D printed PVA channels. (Scale bars: 6 mm) (C) Photograph of the inserted electrodes as well as the two PVA printed templates used for the creation of hydrogel-based fluidic device. (Scale bars: 2.5 cm) (D) Photograph of 3D printed sacrificial templates along with the electrodes embedded in a gelatin hydrogel construct before the dissolution and removal of PVA (Scale bars: 2.2 cm). (E-F) Photograph of the (E) dissolved and (F) removed PVA from the right channel revealing the fluidic channel divided by the hydrogel barrier (Scale bars: 2.2 cm, 1.8 cm). (H) Hydrogel-based fluidic system (Scale bar: 1.5 cm) (I) Magnification of the right channel showing the active area of the electrodes inside the fluidic channels, indicated by the black arrows (Scale bar: 1.5 mm).

for a non correct positioning of the PVA channels, the most delicate part. PVA channels indeed may be mechanically compromised by the water in the teflon tubes, but also by the same gel due to the crosslinking. The dissolution process may cause leaks: the dissolved PVA, in fact, may occupy the space in which gelatin should be. Therefore an overpressure, that normally can be substained by the gelatin and gelatin-PDMS bonding, may push the dissolved PVA in the gelatin-PDMS interface causing a leak and the failure of the device.

5.5 Electrical characterization

As it has said before, TEER measurements are influenced by many factors. Luckily the best configuration for doing measurements on our devices, included the positioning of the galvanostatic potentiostat, PGSTAT128N (Metrohm Autolab, The Netherlands) next to an incubator, that was actually acting as a Faraday cage. Thus noise coming from dispersion currents of the other apparatus in the lab or from power line was not influencing the data. It was always used, for precaution, a high resistivity support, isolating the devices and forcing just one connection to the ground. In this way we had quite a high signal-to-noise ratio.

The measurements were performed in different days showing reproducibility. The configuration of the electrode was driven by SENSING(S), COUNTER(CE), REFERENCE(RE) and WORKING(WE).

The electrode connections are provided by the Autolab instrument through 4 mm male banana connectors. These electrode connections are labeled as follows:

- Working (or indicator electrode): WE (red)
- Sense electrode: S (red)
- Reference electrode: RE (blue)
- Counter electrode: CE (black)
- Groud connector (green)

In the 2-point probe configuration, the current is measured between the CE and the WE and the potential difference is measured between the RE and the WE, connecting the S to the WE. In 4-point probe mode the CE and RE are connected to a counter and reference electrode, respectively on side of the electrochemical cell. The WE and S are connected to a second set of working electrode and reference electrode on the other side of the electrochemical cell. Both sides of the cell are separated by a membrane. The current is measured between the CE and the WE and the potential difference is measured between the RE and the S. The counter electrode differs from the reference electrode, because this one establishes the electrical potential against which other potentials may be measured. While the working electrode is usually defined as the electrode at which the cell reaction takes place [158].

Notice that the impedance spectra was made in galvanostatic mode. This allows to control the current passing through the electrodes, therefore avoid to burn electrodes or gelatin or eventually cells Figure 5.10. This configuration makes the S and

CE to be the ones that actually measure. Considering that the aim is to measure the biological barrier, the respective electrodes were put, in different channels, one in front of the other.

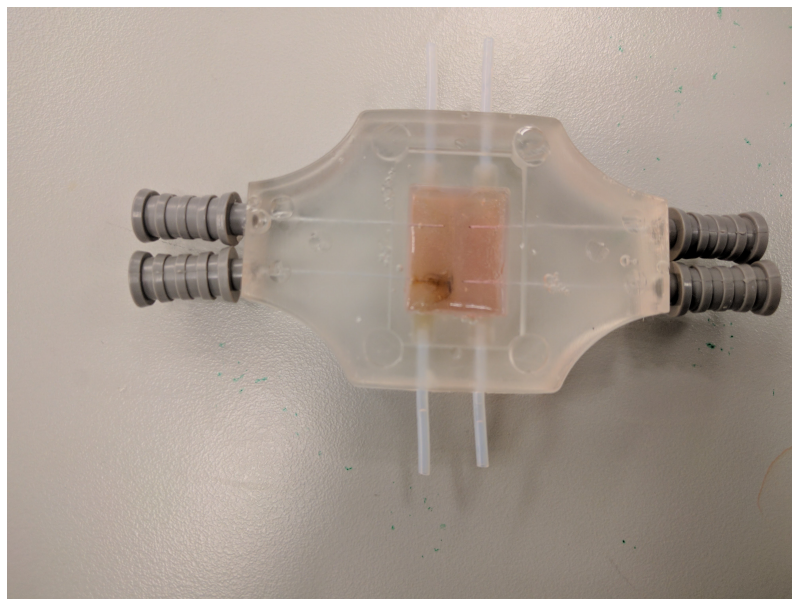


Figure 5.10: The effect of the use of the potentiostatic mode. In this case both the electrode and gelatin are burned.

The maximum current was set at $30 \mu\text{A}$ and the signal imposed was a sine wave type. Higher currents showed in the microscope to produce bubbles in the gelatin. The range of frequencies sampled in the measurement is between 1kHz and 100 kHz.

5.6 Cell culture and seeding

The intestinal epithelium is composed of a single layer of columnar cells which forms the innermost lining of the intestinal tract. The cells of this epithelium differentiate as absorptive enterocytes, anti-microbial producing Paneth cells, mucus producing goblet cells, and hormone producing enteroendocrine cells. Such tissue represents not only a physical barrier, which separates the luminal contents from the host, but also it determines intestinal permeability and plays multiple roles in regulating the mucosal immune system [159]. Goblet cells do not form tight junctions but they are mucus-producing cells that coat the epithelium with a layer of mucus, providing an additional diffusion barrier [3].

As it was mentioned before, the cells used to model the intestinal barrier were Caco-2 (ATCC HTB-37TM). This cell line is preferred with respect to human intestinal epithelial cells because they rapidly undergo apoptosis when cultured *ex vivo* [159]. This cell line is composed by heterogeneous human epithelial colorectal adenocarcinoma cells [160]. An adenocarcinoma is actually a type of cancerous tumor that can occur in several parts of the body. Although Caco-2 derived from a colon carcinoma, when cultured under specific conditions the cells become differentiated and polarized resembling the enterocytes lining the small intestine such that their phenotype, morphologically and functionally [161, 162]. For example Caco-2 cells can

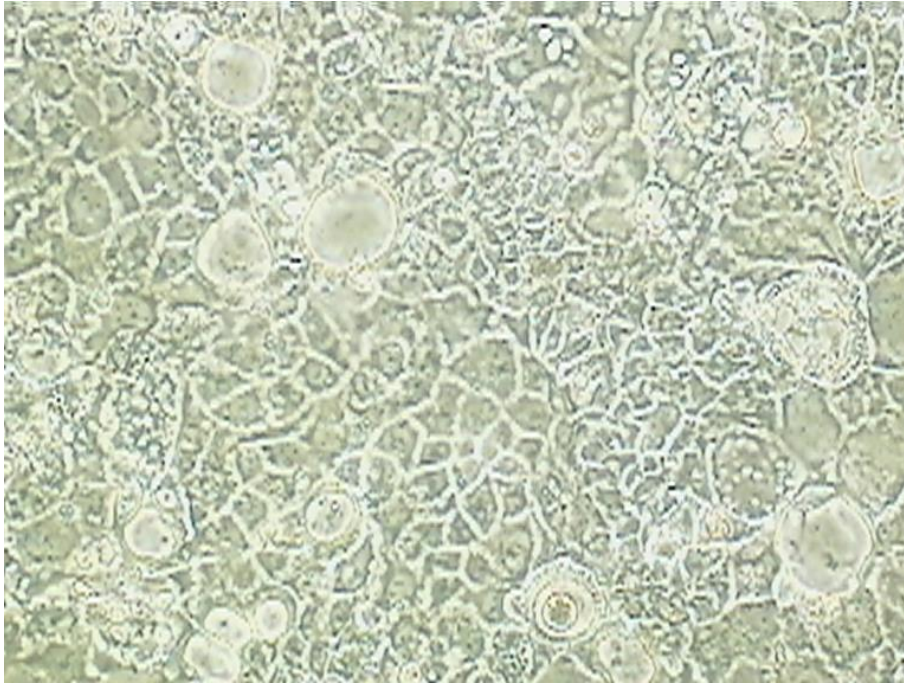


Figure 5.11: Caco-2 image acquired with transmission microscope.

express many characteristic of such enterocytes, like tight junctions, and other enzymes and transporters. They are also capable of create microvilli when they are cultured under a peristaltic flow [64]. The Caco-2 cells are usually used as a model of the intestinal barrier for in vitro toxicology studies. Reproducibility problems often reported in literature have been generally attributed to different culture related conditions, such as the type of animal serum used, the supplements added to the culture media, the passage number and the source of cell clones [163], resulting over the years to have characteristics of the cells that diverge significantly [164]. Caco-2 cell cultures, indeed, microscopically and even by visual inspection, are heterogeneous, and therefore difficult to compare results across labs.

The reasons why Caco-2 cells are often used for studying nutrient and drug transport is because they provide the main routes of substance transport:

1. the paracellular route through tight junction complexes;
2. the passive transcellular route through the bodies of epithelial cells;
3. the active, carrier-mediated paracellular route through cells;
4. transcytosis.

Across the pharmaceutical industry, they are most commonly used as a confluent monolayer, usually seeded in Transwell chamber.

Preventing contamination and providing renewed nutrients, the cells can reach confluence in 3-4 days, i.e. the surface onto which cells are grown is almost completely covered [163]. Specifically after 2-3 weeks, a densely populated cell layer forms, differentiating spontaneously into polarized enterocytes and a monolayer of columnar cells that are coupled together by tight junction protein complexes [3]. The cells are grown in specific flasks and they are fed with nutrients in the medium.

When cultured in this format and the splitting protocol is performed correctly, the cells differentiate to form a polarized epithelial cell monolayer that provides a physical and biochemical barrier to the passage of ions and small molecules [165]. A culture medium is a solid, liquid or semi-solid designed to support the growth of microorganisms or cells [1] or small plants. Cells anyway are usually grown onto flat surfaces, therefore medium is in liquid form in order to cover them. The amount of medium depends on the surface, that is strictly related to the number of cells. The medium used for Caco-2 cells is Dulbecco's Modified Eagle Medium (DMEM; Gibco) with high glucose enriched with 20% fetal bovine serum (FBS) and 1% penicillin/streptomycin. Eagle's minimal essential medium (EMEM) is a cell culture medium developed by Harry Eagle that can be used to maintain cells in tissue culture. It contains:

1. aminoacids
2. salts (calcium chloride, potassium chloride, magnesium sulfate, sodium chloride, and monosodium phosphate)
3. glucose
4. vitamins (folic acid, nicotinamide, riboflavin, B₁₂)

A variation of this medium is DMEM and contains approximately four times as much of the vitamins and amino acids present in the original formula and two to four times as much glucose. Additionally, it contains iron and phenol red. The use of the 10% or 20% serum is almost a personal choice and it is due to the fact that cells derived from whole organisms and grown in culture often cannot grow without the addition of, for instance, hormones or growth factors which usually occur in vivo [166]. In the case of animal cells, this difficulty is often addressed by the addition of blood serum or a synthetic serum replacement to the medium. The enrichment with penicillin, instead, is in order to prevent a possible contamination and the following death of the cells. Every time the medium in the flask is consumed is visible, thanks to pH dependent colorants in it, and obviously it should be changed. The cells are grown in an incubator, thus in a controlled and sterile environment in which the temperature is 37°C and 5% CO₂. The cells are allowed to grow until approximately 80% confluence before splitting of the cells. The splitting is carried out in order to decrease the number of cells in the flask.

1. The medium is removed from the cells.
2. The cells are washed with PBS
3. A trypsin/EDTA solution is added so that it just covers the cells and the flask is placed in the incubator for few minutes.
4. If the cells are loosened from the bottom of the flask, medium is added and mixed with the cell suspension.
5. The cells are divided by suspension with centrifugation and mixed again with the medium.
6. The obtained suspension is put in a flask and placed in the incubator.

If the splitting protocol is not performed correctly, it is probable to encounter cells death because of formation of clusters or cells damaging.

Caco-2 cells are grown enough to reach the number of cells needed for the seeding. This number depends on the surface that they need to cover and also on the material composing this surface. As a matter of fact, cells may change shape and occupy the surface with respect to the material and amplitude of the area that they are actually covering. Their covered area is indeed wider onto rigid material and smaller onto soft ones [167]. In previously cited device ([64]) the cell density used was $1.5 \cdot 10^5$ cell/cm². The surface that those cells were covering anyway is stiffer than the gelatin. Moreover Caco-2 cells of our batch had a mean diameter ranging between 12.9 μm and 14 μm , known thanks to the NucleoCassette (ChemoMetec NucleoCounter). In the final design we have:

- Inner surface per each channel equal to: $\mathbf{S} = 1.557 \text{ mm}^2$
- **volume** of: $\mathbf{V} = 5.3735 \text{ cm}^3 = 53.735 \mu\text{l}$

Therefore, it results:

- Thus the **total number of cells** for such a surface is: $\mathbf{n}_{\text{cell}} = 23 \cdot 10^6$ cells
- Therefore the density of cells is: $\mathbf{d} = 8 \cdot 10^5 \text{ cells/cm}^2$

When the seeding is performed it is needed to assure the exact amount of cells. This is made by trypsinizing the cells from flasks, suspending those cells in a certain amount of medium and therefore generating the batch. c_1 is the concentration of cells in the batch suspension and it is obtained thanks to NucleoCassette. The batch suspension then is concentrated to c_2 in order to have $23 \cdot 10^6$ cells in each channel, obtaining $8 \cdot 10^5 \text{ cell/cm}^2$.

$$c_2 = \frac{n_{\text{cell}}}{V[\text{mL}]} \quad (5.15)$$

Therefore the concentration is obtained taking from the batch a volume V_1 such as:

$$V_1 \cdot c_1 = V_2 \cdot c_2 \quad (5.16)$$

At this point the seeding is performed injecting the suspension in the channel of interest. The channel in question should be treated with a protein that can re-assemble the ECM. Since Caco-2 cells are used, the choice was directed to fibronectin (Sigma Aldrich 1%), that is the most common glycoprotein of the extracellular matrix produced by the intestine. Anyway other possible choices may be matrigel and laminin. The concentration of those proteins should not be higher than 50 $\mu\text{g/mL}$. Anyway the diffusivity in the hydrogel is very high, therefore, once the solution is inserted in the channels, the initial concentration decrease very rapidly, following Fick's laws. That is why it was used laminin with a concentration of 100 $\mu\text{g/mL}$, and it was left in the channels for a quarter of a hour before the seeding.

The last part of the seeding step are the rotation: in order to let cells deposit onto all the surfaces of the channel the device is put in 4 different position, corresponding to rotations of 90°, for at least 20 minutes. This interval was adjusted several times but it seems that 30 minutes is a good compromise, giving the cells the time to attach but also avoid the detachment of the cells on the other sides of the channel.

5.7 Fluorescence staining

Fluorescence staining was used in order to assess the seeding quality. This was allowed by Hoechst 33342 (Invitrogen), capable of labeling the cell nuclei, and Phalloidin (F432, Invitrogen) for labeling the cellular membrane.

Hoechst 33342 is excited by ultraviolet light at around 350 nm, and emits blue-cyan fluorescent light around an emission spectrum maximum at 461 nm. Hoechst stains can be excited with a xenon- or mercury-arc lamp or with an ultraviolet laser. There is a considerable Stokes shift between the excitation and emission spectra that makes Hoechst dyes useful in experiments in which multiple fluorophores are used. This dye is used for the imaging of nuclei. This cell-permeable dye is effective for fixed-cell and live-cell staining. Because Hoechst stains bind to DNA, they interfere with DNA replication during cell division. Consequently, they are potentially mutagenic and carcinogenic, so care should be used in their handling and disposal [149].

Phalloidin is a bicyclic peptide that belongs to a family of toxins isolated from the deadly *Amanita phalloides* "death cap" mushroom and is commonly used in imaging applications to selectively label F-actin in fixed cells, permeabilized cells, and cell-free experiments. Phalloidin is much smaller than an antibody that would typically be used to label cellular proteins for fluorescent microscopy which allows for much denser labeling of filamentous actin and much more detailed images can be acquired, particularly at higher resolutions.

Cells treated with phalloidins exhibit a number of toxic effects and frequently die [9]. Furthermore, it is important to note that phalloidin-treated cells will have greater levels of actin associated with their plasma membranes, and the microinjection of phalloidin into living cells will change actin distribution as well as cell motility. Phalloidin originates from the *Amanita phalloides* mushroom. It is toxic because it irreversibly binds together filamentous actin, which paralyzes the cell's cytoskeleton and leads to cell (or organism) death. This is why it is used with fixed cells [168]. The steps to be followed to do the staining are explained in the following:

1. the samples are washed twice with PBS
2. they are fixed in 4.5% (w/v) paraformaldehyde in phosphate buffered solution (PBS) for 20 minutes
3. PBS washing
4. the samples are permeabilized with 0.1% (v/v) Triton X-100 in PBS for 10 minutes
5. the samples are stained for 45 minutes with Hoechst
6. PBS washing
7. the samples are stained for 45 minutes with Phalloidin

5.8 Imaging and analysis

Confocal acquisitions were performed using a Zeiss LSM 700 module in the Axio Imager M2 upright microscope using: an epiplan-neofluar 5X/0.13 HD, and 10X/0.25

HD. To eliminate any possible crosstalk between channels, images were collected with a sequential scan, using the following laser lines and mirror settings: 405 (30%) 420-480 nm; 555(30%) 605-700 nm. Photographs of the fabrication of the fluidic system were acquired using a DSLR camera (Canon EOS, 5D Mark II; Canon). ImageJ was used to visualize composite images by combining fluorescent channels, to visualize the dark-field mode images. The diameter of the channels was measured by ImageJ software using at least 4 images from different areas of 3 samples for each condition [104].

Chapter 6

Results and Discussion

Hereby are showed the analysis of the actual geometrical dimension obtained after the fabrication process of the core of the device, its electrical characterization and the results of the cell seeding.

6.1 3D printing and fabrication of the barrier fluidic device

As it was explained in the previous chapter, 3D printed PVA structures were used as the sacrificial template to create two channels inside the hydrogel bulk. Those channels are separated by a hydrogel barrier with a controlled thickness. Figure 5.9 A-B show the designed CAD structure and the sacrificial templates 3D printed in PVA, respectively. The printed structure were designed to have square transversal area with dimensions of 1.2 mm x 1.2 mm. To be conform with the model, the design of the printed PVA structure was made to assure a hydrogel barrier thickness of 300 μm and two independent and almost parallel channels. The actual printed structures had a width dimension of 1.33 ± 0.04 mm and layer thickness of 1.21 ± 0.10 mm (Figure 6.1). The printed PVA were used also to control the position of the electrodes, thanks to the guides for the electrodes integrated into the fluidic molds. Before the casting, the electrodes were inserted until the tip of the needle in strong contact with the sacrificial templates printed in PVA (Figure 6.1). That allowed to prevent an interposition of the gelatin and therefore be sure that the electrodes were inside the channels.

After the dissolution of the sacrificial templates, the final gelatin/TG hydrogel fluidic device had dimensions of 18 mm x 14 mm x 9mm with a resultant volume of $\approx 2.3\text{cm}^3$. The width and the height of the two embedded channels within the hydrogel were then measured by microscopy, resulting to be respectively 1.78 ± 0.18 mm and 1.76 ± 0.15 mm (Figure 6.1). The gelatin barrier thickness was found to be $370 \pm 75\mu\text{m}$ (for a design of 300 μm).

The structural stability of the fabricated device was tested by perfusing both channels with 65 $\mu\text{L}/\text{min}$ for 48 hours at 37°C. It was found that the device along with its built-in barrier was mechanically stable without any structural deformation in response to the volumetric flow rate or increase in temperature. The exposed area of the electrodes was in position inside the channels and stayed in place during perfusion (Figure 5.9).

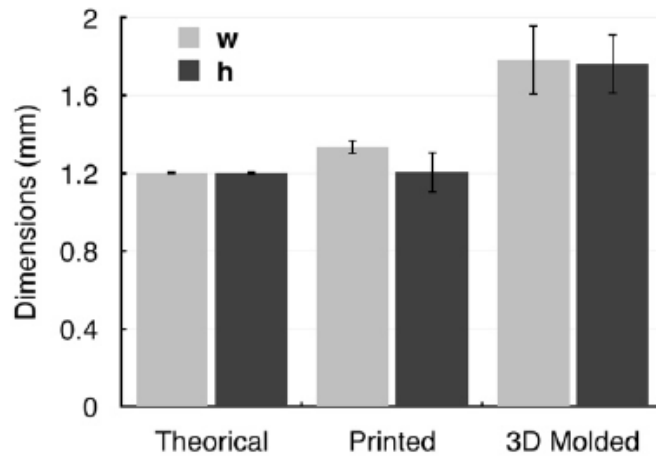


Figure 6.1: Quantification of the dimensions of the designed channels, 3D printed templates, and embedded channels fabricated within the gelatin/TG hydrogel.

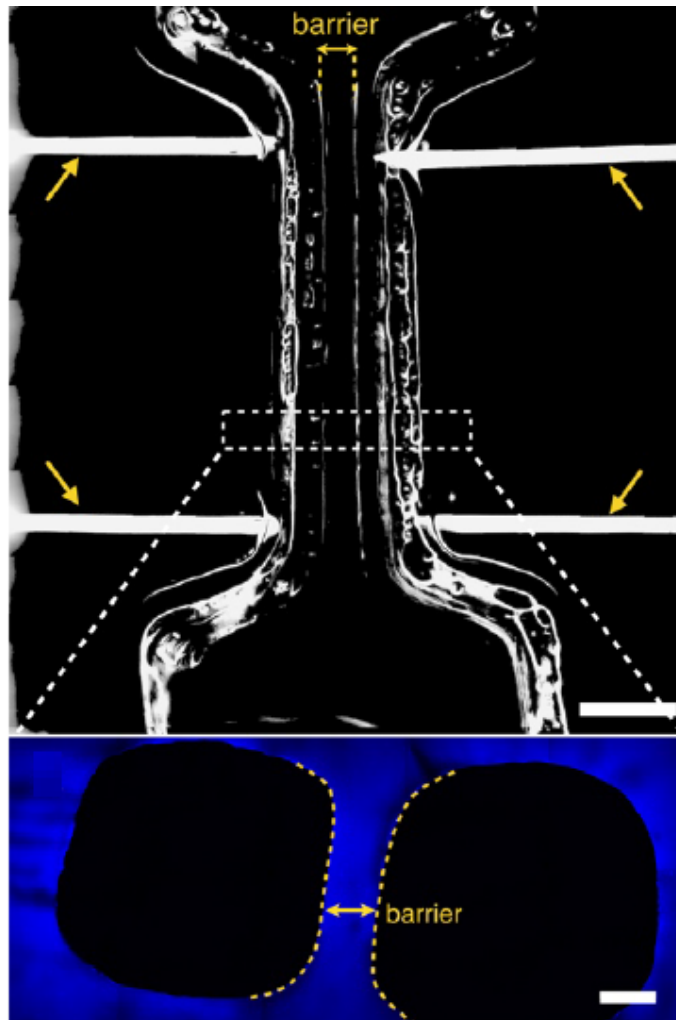


Figure 6.2: Dark-field image of the hydrogel-base fluidic system integrating the needle electrodes, indicated by the yellow arrows, (Scale bar: 2 mm) and fluorescence micrograph of the cross-section of the fluidic device. It shows the the gelatin barrier separating the two channels separated, the scale bar corresponds to, $500\mu m$

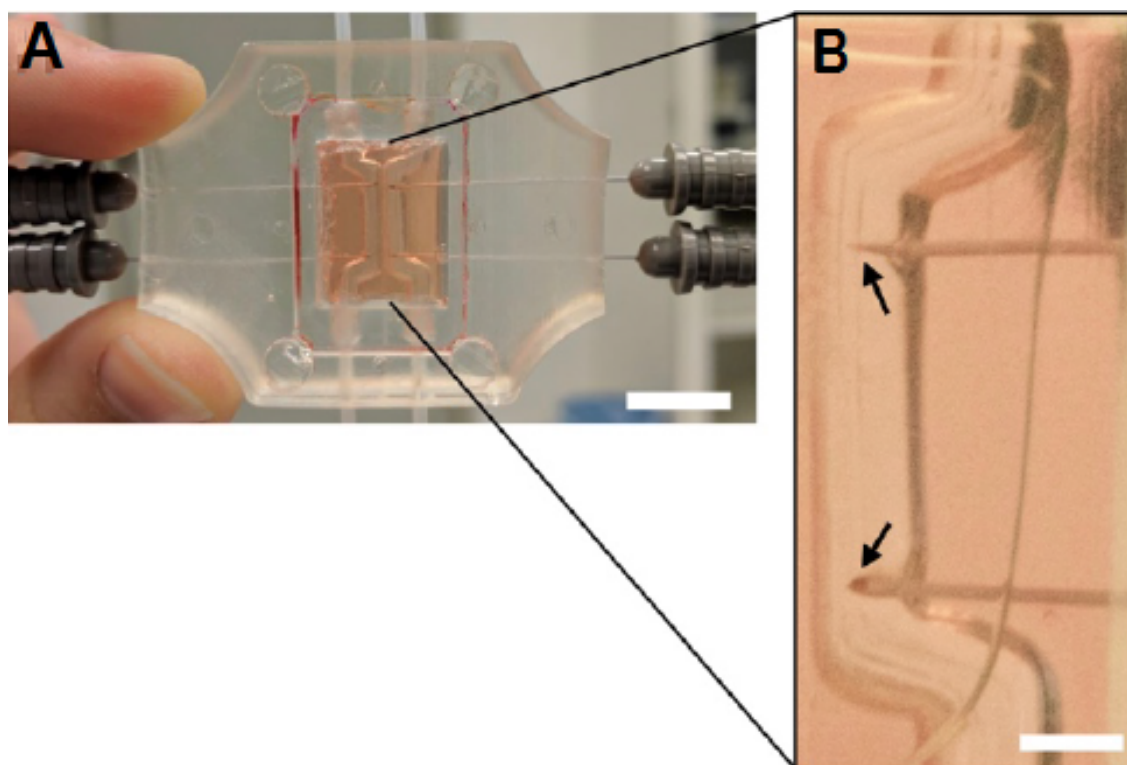


Figure 6.3: (A) Hydrogel-based fluidic system (Scale bar: 1.5 cm) (B) Magnification of the right channel showing the active area of the electrodes inside the fluidic channels (indicated by the black arrows). (Scale bar: 1.5 cm)

Such barrier thickness of $370\ \mu\text{m}$ derived mostly by the risk of merging channels rather than the impossibility to lower the distance between the PVA sacrificial templates. With this purpose, the presence of the electrodes in the fluidic mold was actually helpful for the positioning of PVA channels. Anyway, one of the challenges was to have the active part of the electrodes inside the channels, without touching the walls of the channels; the reason will be explained afterwards.

6.2 Cell seeding optimization

The seeding was at first performed using $1.5 \cdot 10^5\ \text{cell}/\text{cm}^2$, having as a reference results from the articles [64]. The experiment with these conditions was performed several times. In three experiments the devices rotated 6 times of 90° every 20 minutes, starting from an horizontal position and finishing with a vertical one (such that the channel with cells was above the other one, assuring a better conformality of the barrier). The protein used to confer ECM was laminin at the concentration of $20\ \mu\text{g}/\text{mL}$. While in the three following experiments the devices rotated 8 times of 90° degrees every 30 minutes. Despite the number of experiment, there are not many results because of the failure of the device due the formation of mold. The protein used to confer ECM, in this case, was fibronectin at the concentration of $20\ \mu\text{g}/\text{mL}$. Anyway after 24h incubation it was seen that the Caco-2 cells did not reach the confluence and they showed to be lining on top of each other in one side of the channel (Figure 6.5).



Figure 6.4: An example of a not successful seeding. The cell coverage is too low.



Figure 6.5: Not successful seeding. In this case cells are stacked one onto each other.

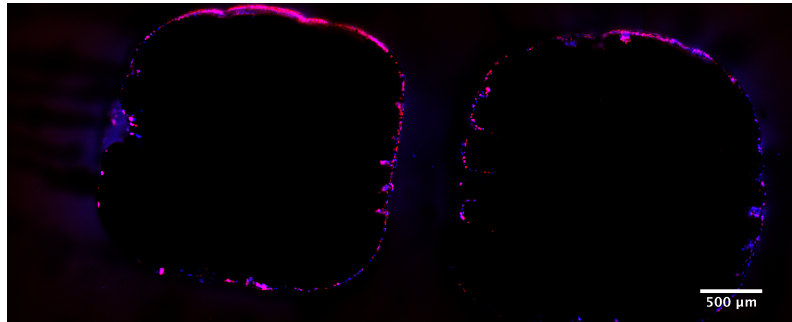


Figure 6.6: Confocal microscopy images of nuclei (blue) and F-actin (red) of the hydrogel-based fluidic system crosssection at 24 hours after the seeding of $8 \cdot 10^5 \text{ cells/cm}^2$ in both channels by rotating the fluidic device of 90° every 45 minutes, for a total of 3 hours, the cells started to be distributed within the surface of both channels.

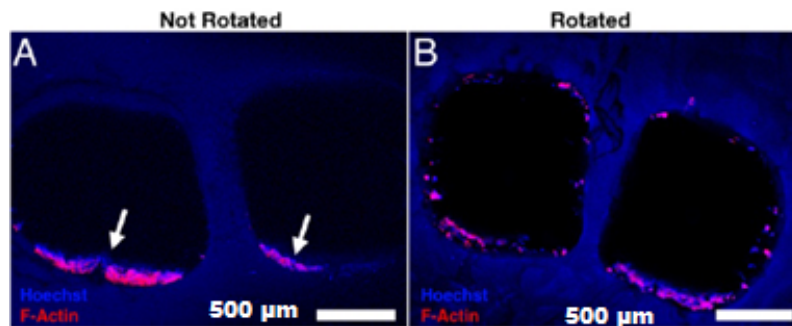


Figure 6.7: Confocal microscopy images of nuclei (blue) and F-actin (red) of the hydrogel-based fluidic system cross-section at 24 hours after the seeding of $1.5 \cdot 10^5 \text{ cells/cm}^2$ in both channels and without flushing; (A) when the fluidic device was not rotated the Caco-2 cells sediment on top of each other (as indicated by the white arrows) while (B) by rotating the fluidic device of 90° every 45 minutes, for a total of 3 hours, the cells started to be distributed within the surface of both channels.

It is likely that the cells were aggregated in this way as they had enough time to sediment. Another possible reason may be also for the low concentration of fibronectin and laminin ($20 \mu\text{g/mL}$). In fact due to the nature of the gelatin, the solution diffused rapidly in the bulk resulting in a low superficial concentration. Therefore such concentration was increase to $100 \mu\text{g/mL}$. In contrast, we could observe a better cell distribution within the whole surface of the channels when rotating the fluidic device for 90° every 30 minutes for a total of 3 hours (Figure 6.6).

In order to prove what it was previously showed, it was made a trial to increase the coverage of the surface and $8 \cdot 10^5 \text{ cells/cm}^2$ were seeded in both channels, in addition the fluidic device was rotated every 20 minutes for 4 times. After the last rotation, one of the channels was flushed with fresh culture media, removing the excess of not adherent cells, while the other was not. After 24 hours, the cells were homogeneously distributed as well as covered the whole surface of the channels in both flushed and not flushed condition, respectively Figure 6.8 A-B.

However, in the channel that was not flushed, a major aggregation and superposition of Caco-2 cells were observed after the last rotation (Figure 6.8, left channel).

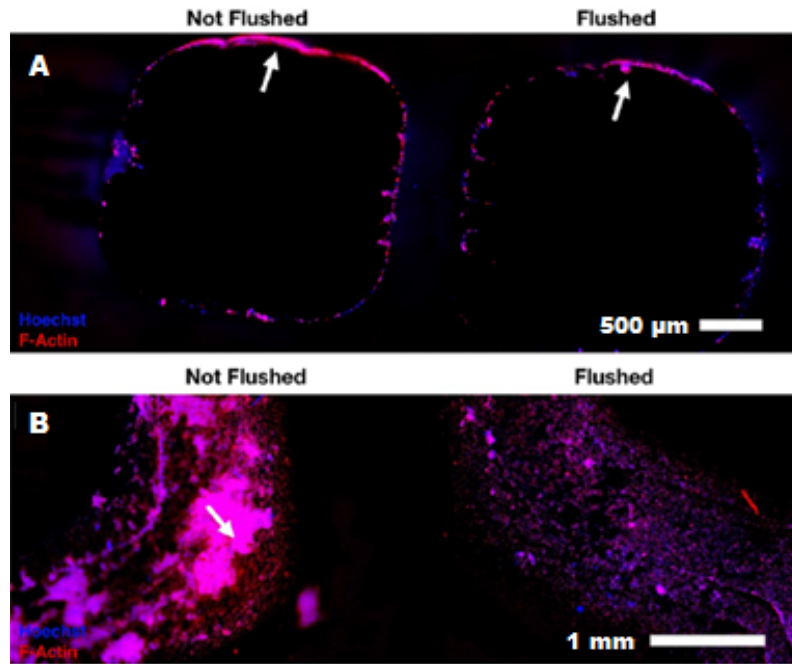


Figure 6.8: (A) Confocal microscopy images of nuclei (blue) and F-actin (red) of the hydrogel-based fluidic system cross-section at 24 hours after the seeding of $8 \cdot 10^5 \text{ cells/cm}^2$ in both channels. When the fluidic device was not flushed (channel on the left) the Caco-2 cells sediment on top of each other in the last rotation position. When flushed (right channel) the amount of aggregate cells was smaller compared to the channel not flushed (Scale bar: $500 \mu\text{m}$). (B) Confocal microscopy images of nuclei (blue) and F-actin (red) of the hydrogel-based fluidic system cross-section, parallel to both channels, at 24 hours after the seeding of $8 \cdot 10^5 \text{ cells/cm}^2$ in both channels confirming that when not flushed the cells will sediment on top of each other. (Scale bar: 1 mm)



Figure 6.9: Seeding with $8 \cdot 10^5 \text{ cells/cm}^2$. The result of this seeding could not be verified.

This was not observed in the channel where the excess of non-adherent cells has been removed (Figure 6.8, right channel).

This experiment was performed a second time but there were just 4 rotations every 40 minutes. The only channel seeded was flushed after the last rotation (Figure 6.9).

Despite in previous studies the Caco-2 density of $1.5 \cdot 10^5 \text{ cells/cm}^2$ could create a confluent monolayer in a PDMS membrane [64], the same did not happen for our gelatin fluidic device. One possible explanation is that since PDMS is a relatively stiff material and the surface occupied by the adherent cells is dependent on the stiffness of the substrate [167], it is possible to assume that the material could influence the number of cells needed for covering the whole surface. Considering that gelatin is softer compared to PDMS the overall morphology of the adherent Caco-2 cells most-likely would have been different. The results confirmed that it was necessary to increase five times the cell density necessary to form a confluent monolayer in a PDMS membrane to obtain the same confluent monolayer in our gelatin based fluidic device (Figure 6.10)

TEER measurements were performed in the meantime. When the cell concentration was $1.5 \cdot 10^5 \text{ cells/cm}^2$, impedance values did not show significant values because of the low cell coverage, as it was explained before. Even with the second concentration there were no good results because of the formation of mold that affected one by one all the devices within three days, making not possible the attainment of the confluence.

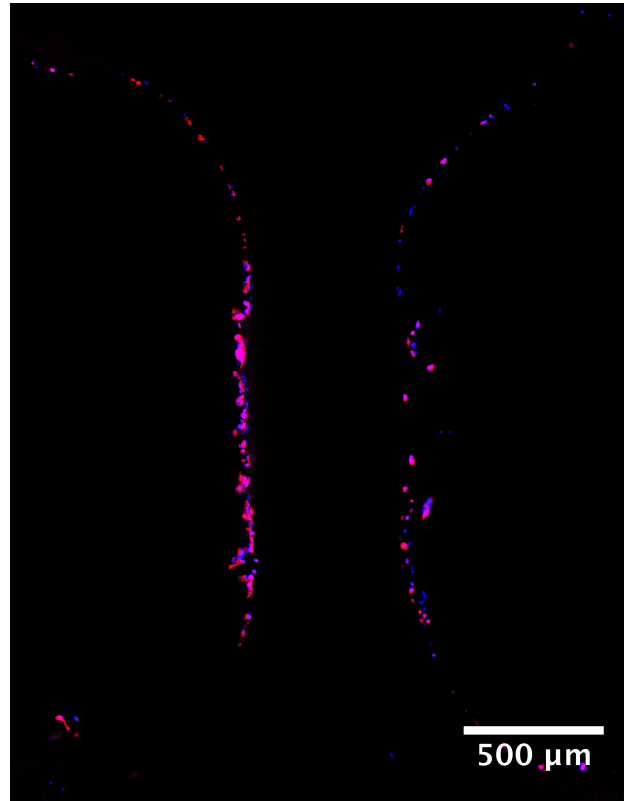


Figure 6.10: Confocal microscopy images of nuclei (blue) and F-actin (red) of the hydrogel-based fluidic system cross-section, depicting the barrier and Caco-2 cells after 24 hours of the seeding of $8 \cdot 10^5 \text{ cells/cm}^2$.

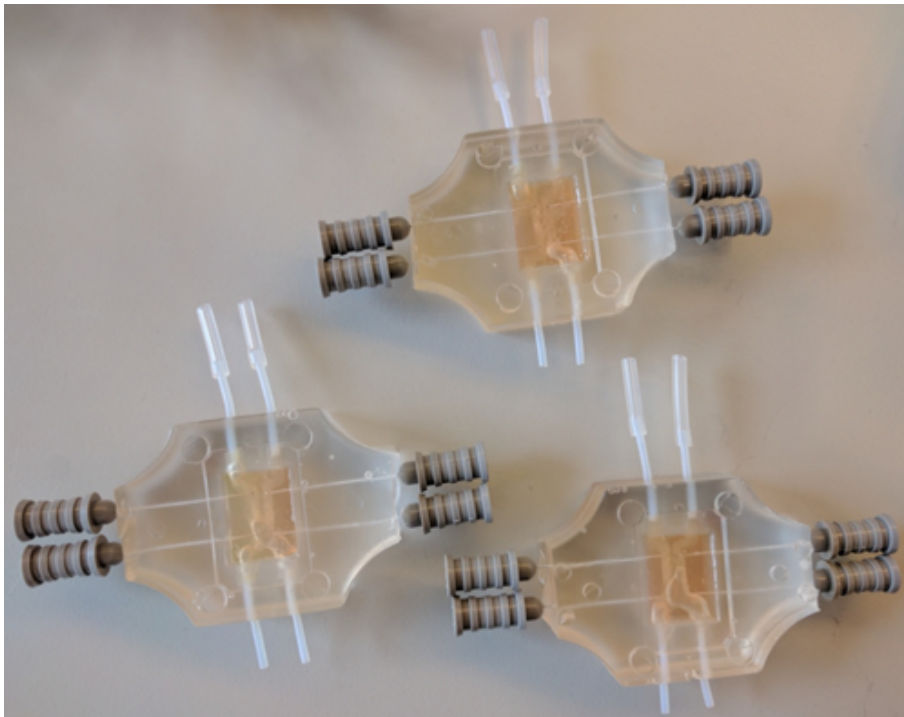


Figure 6.11: Examples of formation of mold. Such formations affected the mechanical stability, disrupting the chemical crosslinking of the gel and made not possible the survival of the cells.

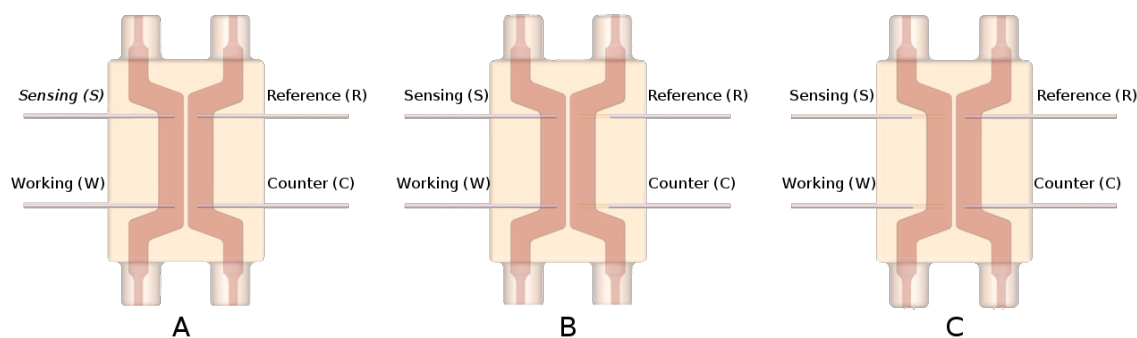


Figure 6.12: (A-C) Schemes of the four-terminal sensing with the 3 different configurations used for impedance measurements. WE and CE form the source connections used to apply a defined current, while S and RE form the sensing connections, used to record the resultant voltage.

6.3 System characterization

In order to make TEER measurements there were three possible configurations for the electrodes, as shown in Figure 6.12.

In the configuration A the electrodes are in the two channels. Therefore, the measured resistance between S-RE has just the contribution of the hydrogel barrier barrier and potentially the contribution of the biological barriers present in one or both channels. Anyway moving the electrodes in the configuration B or C allows the investigation of the single contributes of one or the other compartment. Anyway the configuration A, with all electrodes inside the channels was used throughout the rest of this study.

The totality of the measurements was made having the samples inside the incubator (37°C and 5% CO₂), controlling therefore the environment parameters and discarding the effect of the temperature.

The impedance measured when the channels are filled with medium resulted to be very similar conductivity with respect to the crosslinked gelatin, without channels. The measured impedance had almost a constant trend and varies between 4 Ω and 6 Ω . Also the phase angle had a constant value $\sim 0^\circ$ throughout the whole frequency range (1-100 kHz). Those data indicate the absence of capacitive or inductive effects and that the hydrogel bulk has just resistive component (Figure 6.13 and Figure 6.14) As it was previously said the measurement are not influenced by electrodes polarization because of the use the 4-point probe measurement setup, contributing to have a phase angle of 0° .

The explanation for the impedance similarities is due to the fact that since the gelatin hydrogel was solubilized in the culture medium the conductivities of the two phases across the barrier (i.e., liquid and solid gel) were identical.

In order to characterize the device, it was at first analyzed if it could sense different medium. This is why were compared measurements in gel (without channels), with inner channels full of medium and with air.

Figure 6.13 shows that when an insulating material, such as air, is present within the channels, the impedance magnitude increases from 6 Ω to 10 k Ω . Such a difference depends from the amplitude of the channels and from the position of the electrodes inside them.

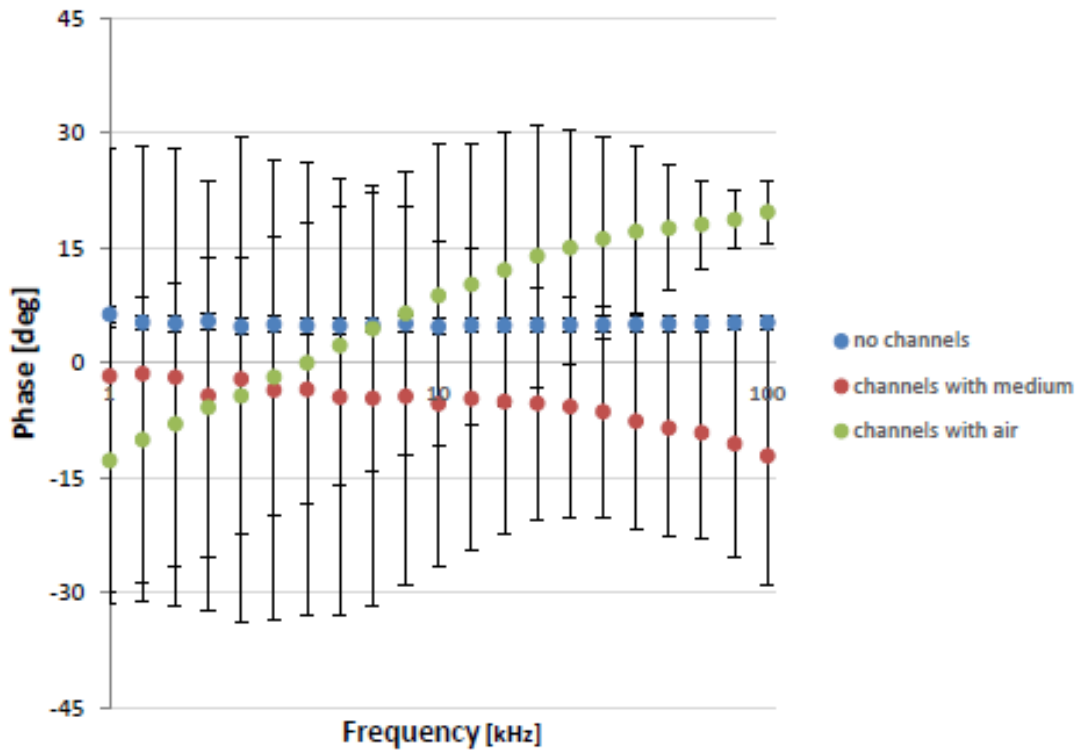
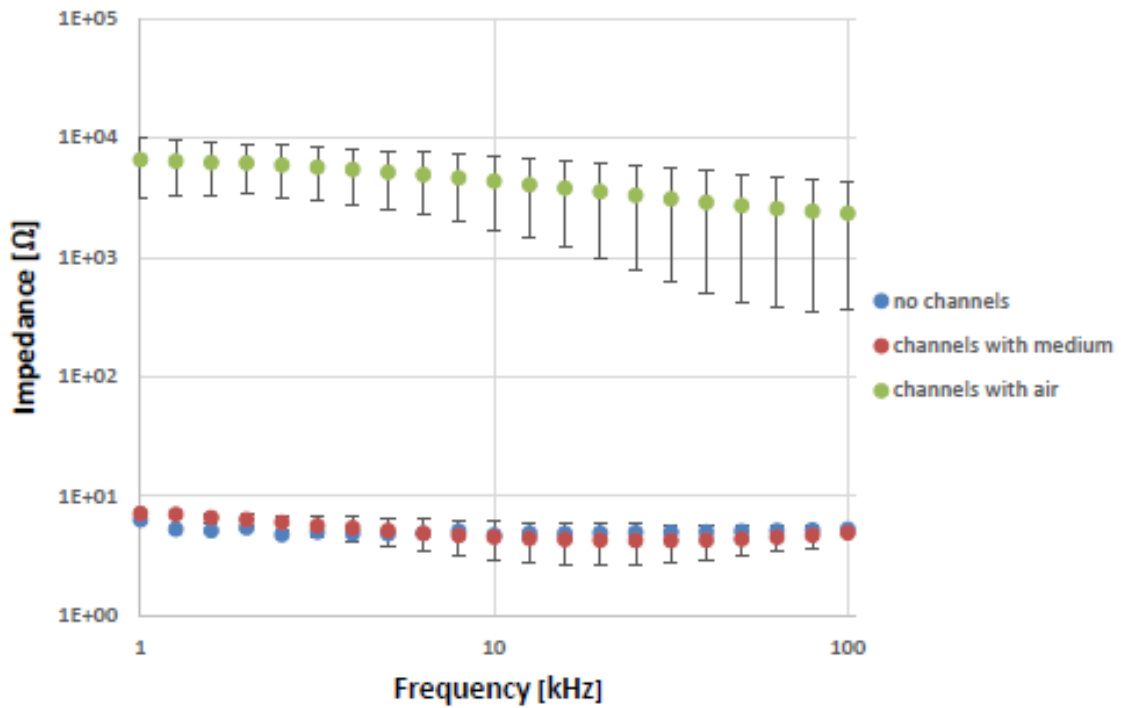


Figure 6.13: Bode plot, of the impedance spectra recorded at 37°C within a gelatin/TG hydrogel and across a gelatin/TG barrier defined by two fluidic channels perfused either with air or with culture medium.

Given the result obtained by this comparison, were measured samples filled with different liquids, but very similar conductivities, in order to test the device sensitivity. Those liquid were:

- water+PBS 1:10
- water+PBS 1:2
- PBS (electrical conductivity $\sigma \approx 1.5S/m$)
- DMEM (electrical conductivity $\sigma \approx 0.25S/m$)

As it is possible to see in Figure 6.14, , PBS had the lowest impedance magnitude value ($\approx 3\Omega$), followed by medium ($\approx 4\Omega$). As the conductivity of the solutions decreased (e.g., diluted PBS with distilled water) the impedance magnitude increased. However, the impedance magnitude variation did not scale up with overall conductivity changes due to the small volume of electrolyte within the fluidic channels ($100 \mu L$). Probably this response is due to a fast diffusion of ions, from the hydrogel bulk to the small volume of the measure electrolyte, since the hydrogel was prepared by dissolving gelatin in cell culture media. Interestingly culture media in the channels showed a very stable impedance phase, with a resultant phase angle of 0° (Figure 6.16 and Figure 6.17). On the other hand PBS and its dilutions in water showed very specific trends. This proved that the system can discriminate between small variations in conductivity even though the volumes within the channels are small ($\sim 100\mu L$).

It was analyzed at the same time how the position of the electrodes may influence the measurements, considering what it is said in literature. The measurements were done with channels filled with medium and the electrodes were put in three different position, that can be summarized in :

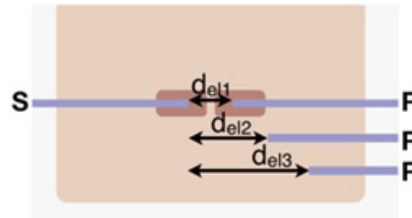


Figure 6.15: Electrode positions

- All four electrodes inside the channels
- Two electrodes inside one channel and the other couple just outside the other one
- Two electrodes inside one channel and the other couple far away from the other one

The electrode distances (d_{el}) were: 2 mm, 3.5 mm and 5.5 mm.

In terms of impedance, it is possible to notice the quasi linear relation between the amplitude of the impedance spectra and the electrode distance. On the other hand, the phase is almost constant, with variations that do not exceed 5° . Even if the system showed to discriminate different substances, it has happened to notice errors in the measurements. Impedance data, indeed, showed similarity with the trend of the impedance in gel (Figure 6.18). The variation was evident in the

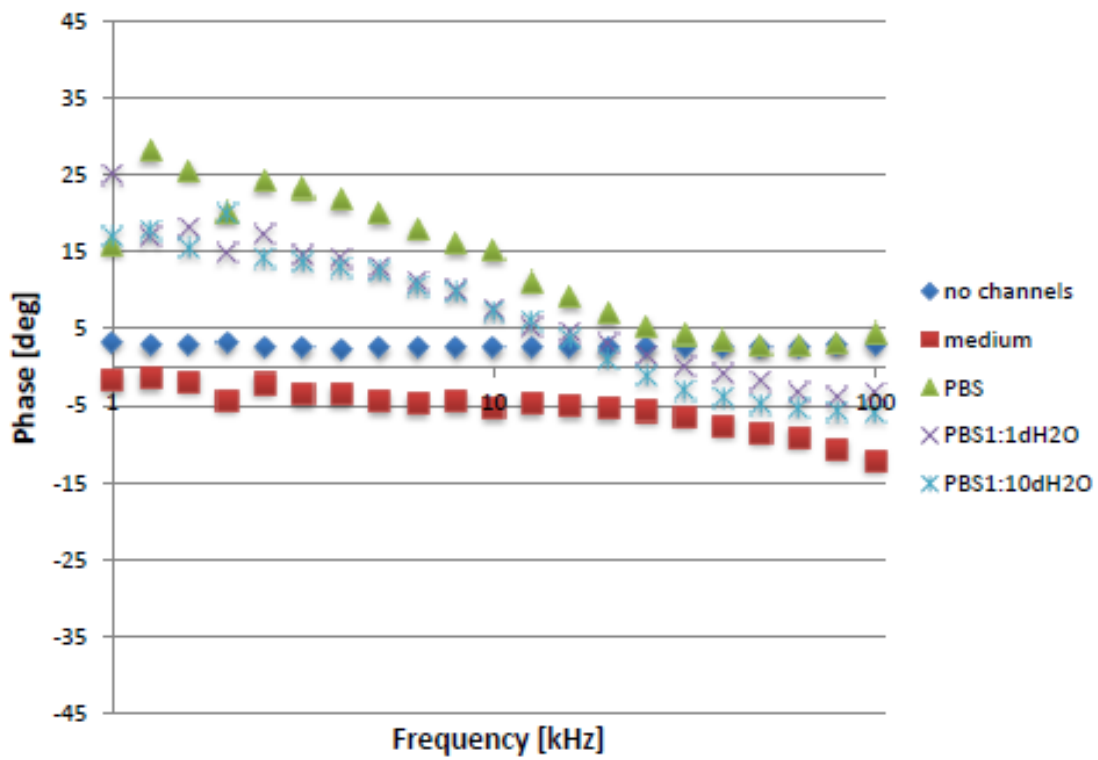
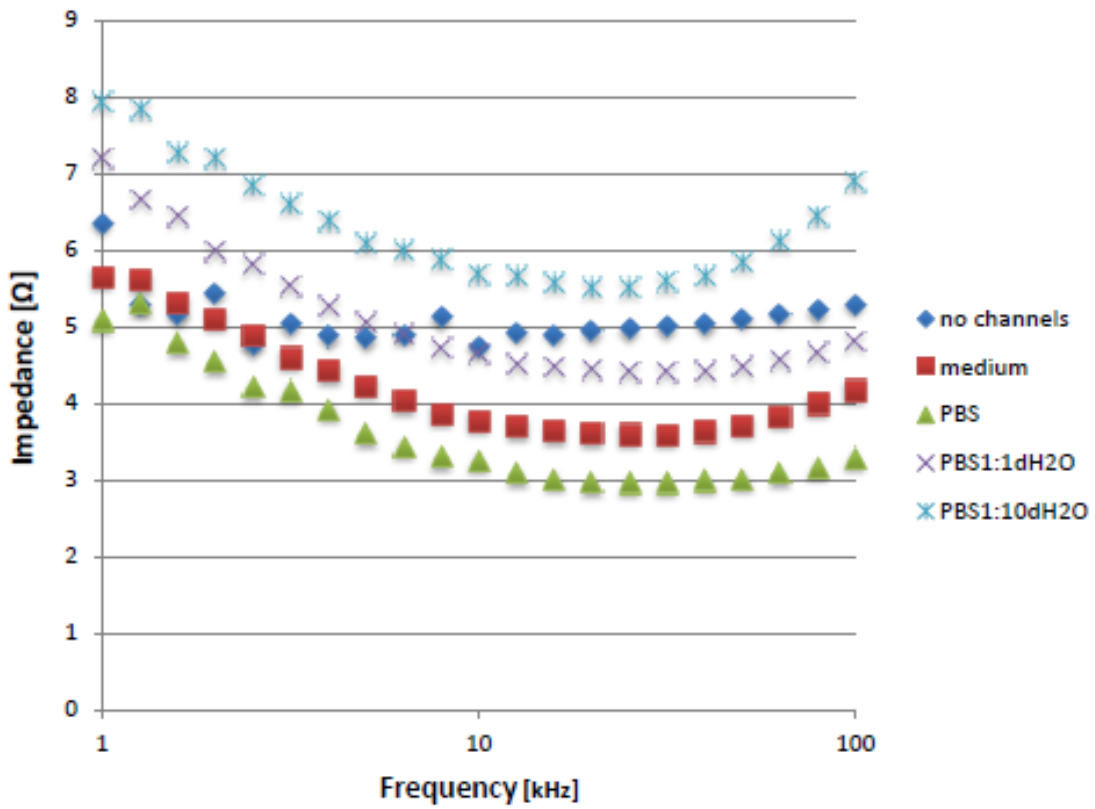


Figure 6.14: Bode plot defining the device sensibility.

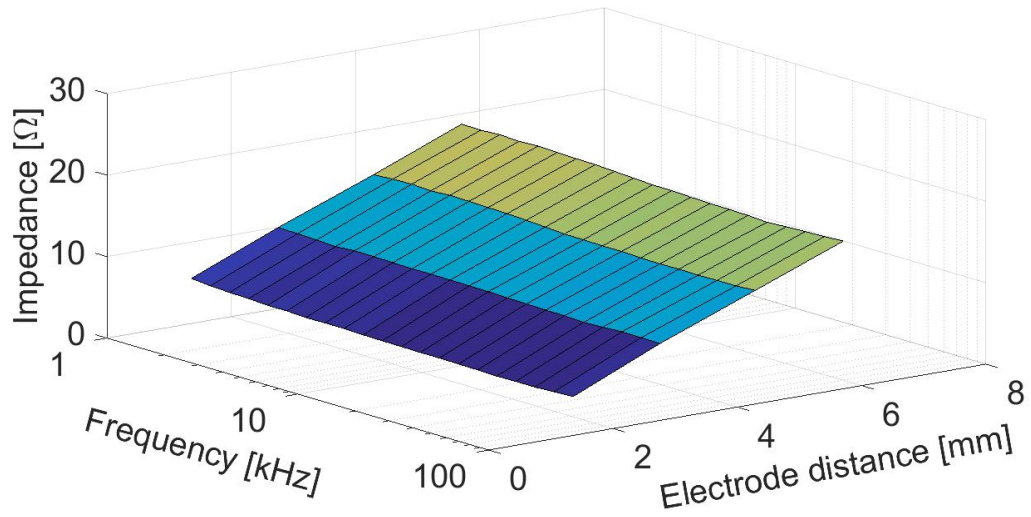


Figure 6.16: Effect of the electrode distance in the impedance spectra measurements.

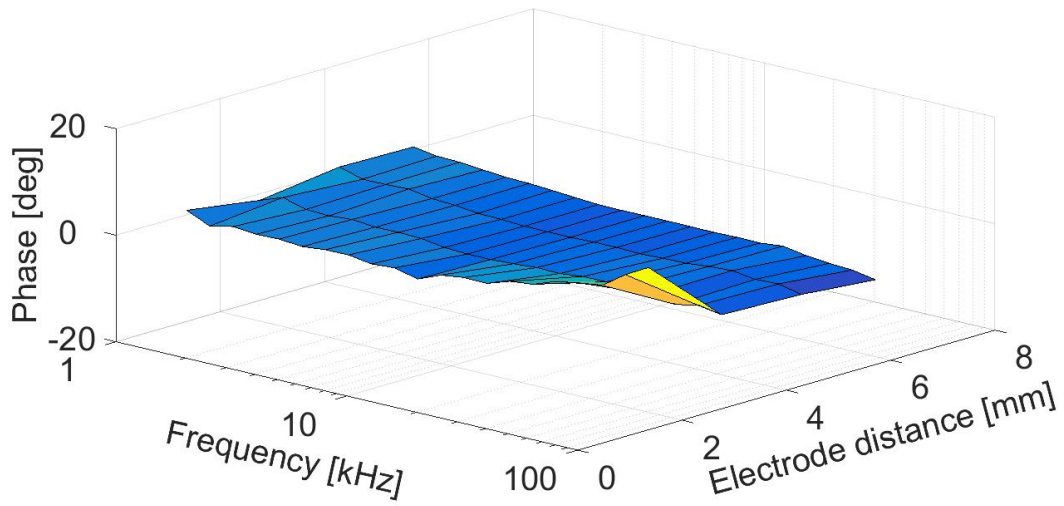


Figure 6.17: Effect of the electrode distance in the phase spectra measurements.

measurements with empty channels, were the spectra is substantially different. The explanation was quite simple: the electrodes were touching the gel. It is shown below the effect. That is how the air became to represent a benchmark, in fact allowed to determine if the electrodes could actually measure what was inside the channels. This is one of the occasion in which the design of the system has changed. In fact, in order to be more sure to avoid the contact effect , channels needed to be bigger.

Moreover, it was studied the effect of the flow on impedance spectroscopy. The flow imposed was in a first experiment, with 1mm of diamenters channels, 20 $\mu\text{L}/\text{min}$. With the increase of channels radius the imposed fluid flow, associated with a shear stress of $0.02\text{dyne}/\text{cm}^2$, was 65 $\mu\text{L}/\text{min}$. In both those experiments the operating temperature was 37° . In parallel, just in this second experiment, two other fluidic samples integrating the measuring system were fabricated and were incubated at the same temperature for 48h. In all the cases cell culture media was used as the electrolyte.

Figure 6.19 shows the impedance magnitude acquired every 24h for samples in static and flow conditions. It appears that for lower frequencies (1 kHz range) the impedance magnitude of samples under fluid flow is slightly higher than the ones in static conditions. By contrast, there is no significant difference between the static and the flow conditions for the mid-high frequencies range. The same behavior is seen in the phase as well Figure 6.19.

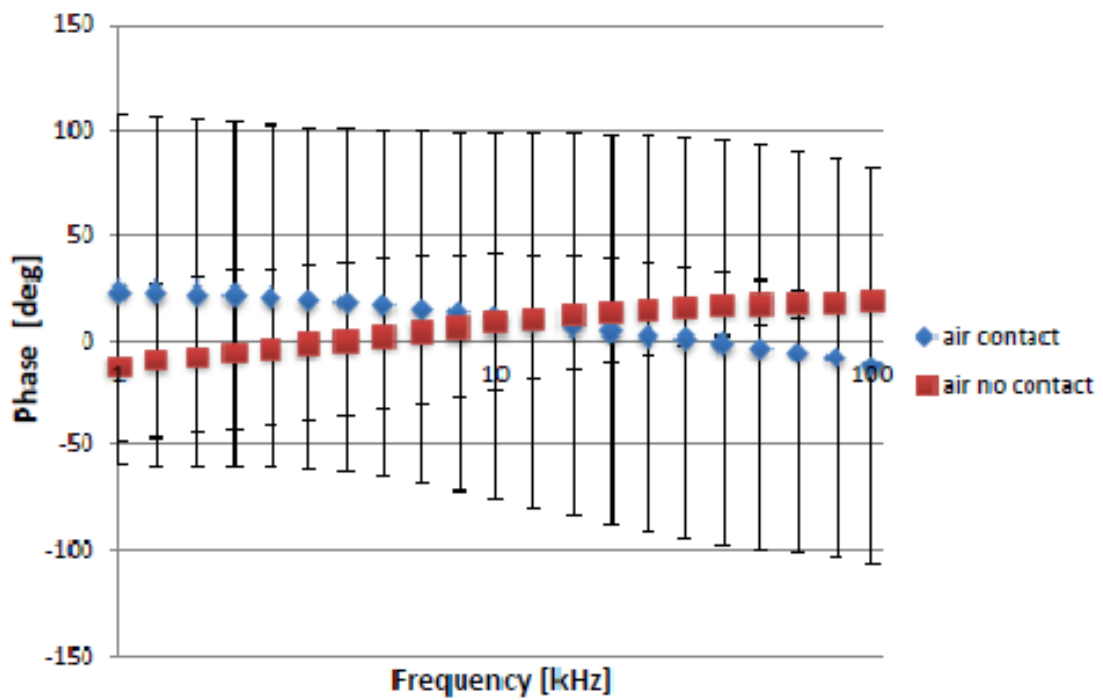
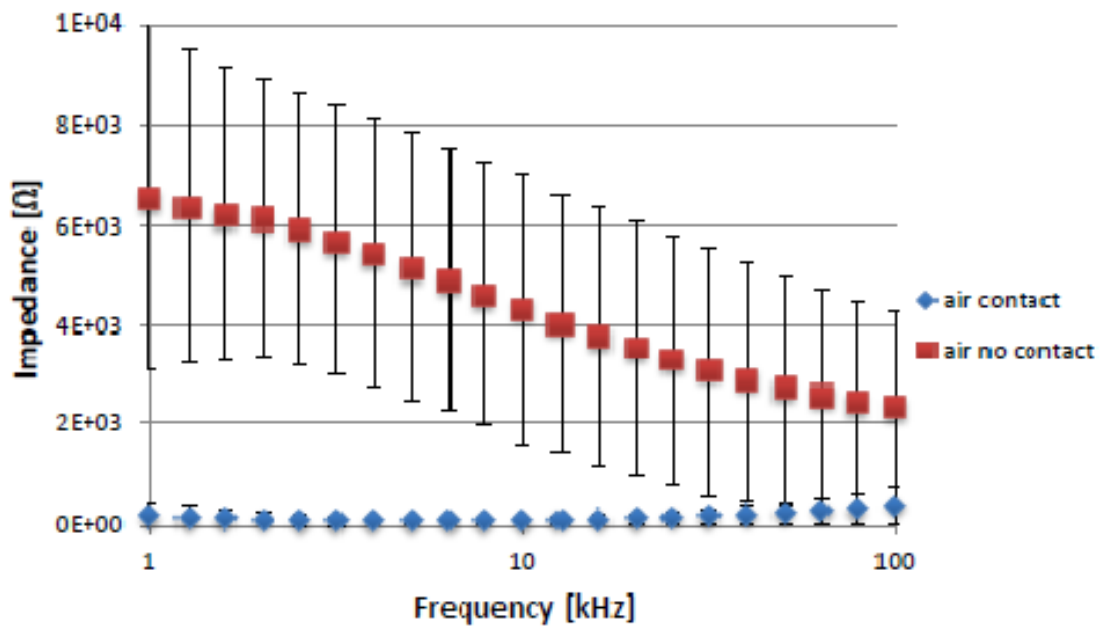


Figure 6.18: Bode plot, defying the correct assembling of the device.

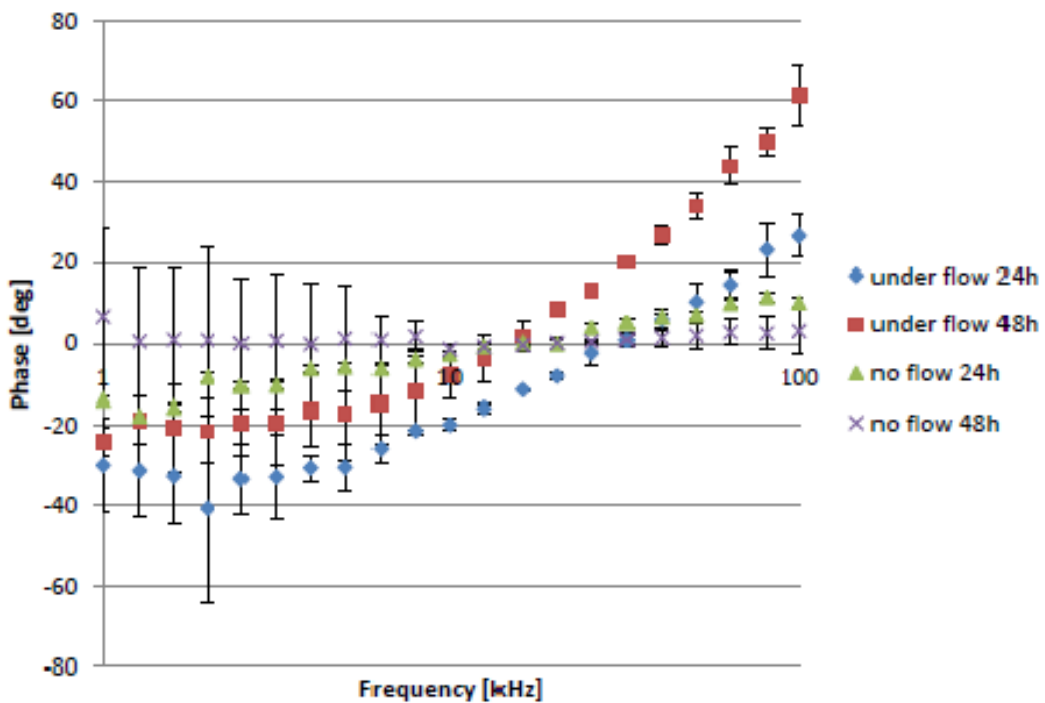
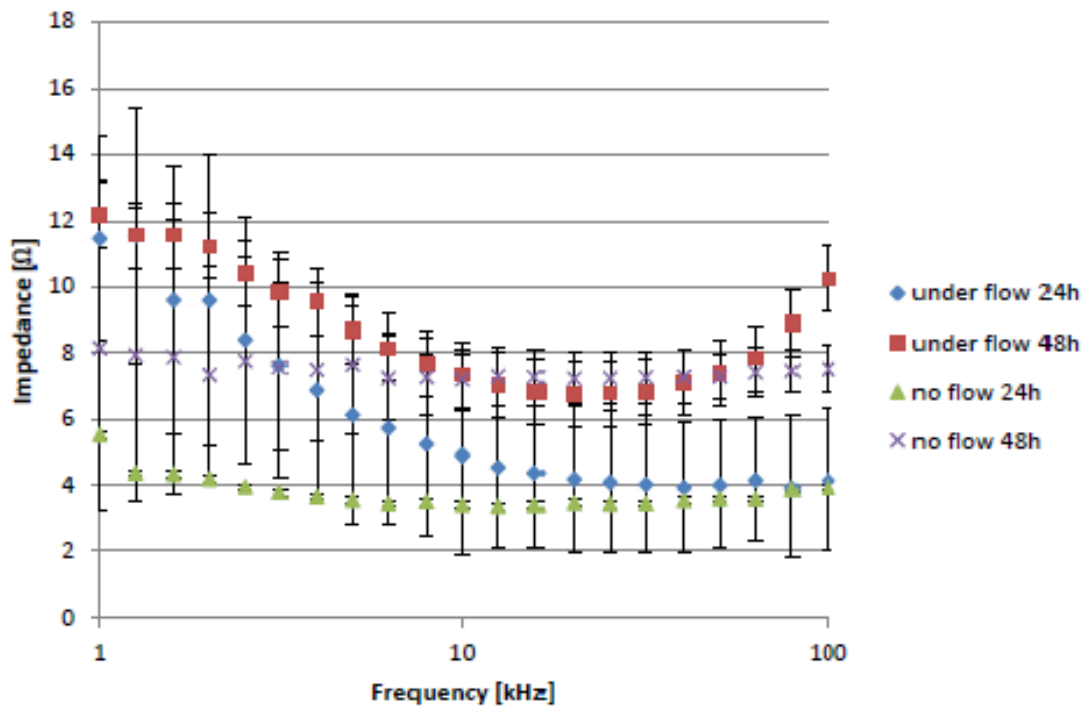


Figure 6.19: Bode plot, follow up of dynamic and static devices for 48h.

Chapter 7

Conclusions and Outlook

In this thesis is explained how it was reached the concept of a hydrogel-based fluidic capable of simulating physiological barriers.

In terms of costs and adaptability the 3D molding technique resulted to be one of the simplest choices. Such adaptability assured to have a design that could host a biodegradable, biocompatible and physiologically reliable scaffold and that could manage the insertion of four stainless electrodes. The system consisted of two independent fluidic channels separated by a hydrogel membrane of $370\ \mu\text{m}$ thickness. The possibility to have the control on the position and avoiding to do measurements in ambient temperature allowed to have reliable TEER measurements. In order to have an overview over the components that could affect the measurements, characterizing the device, the impedance spectroscopy was the most obvious solution.

The fabricated device showed to be capable of sensing different materials with different conductivities maintaining a good sample to sample reproducibility. A couple fluidic devices were tested under continuous perfusion for 48h at 37°C showing that the overall device is capable of perform real time and long term measurements.

It was not possible however to show its reliability as cell scaffold, due to contamination problems, for long periods. Although probably the seeding protocol should be improved, there are anyway good chances of success to form a cell monolayer and to have, therefore, a biological barrier.

Although the proposed device was conceived to simulate a gastrointestinal barrier, it could easily represent different barrier models. In fact it responses to several requirements addressed to biological barrier studies: the presence of the gelatin would give the more characteristic cell-cell and cell-ECM interaction [169], providing a soft and elastic support, while the presence of two parallel channels would allow the formation of chemical gradients in both directions. The hydrogel barrier moreover with its thickness of $350\ \mu\text{m}$ can actually represent a real barrier being at the same order of magnitude of the $200\ \mu\text{m}$ distances observed between capillaries [15].

Other development in this field may derive by co-culturing multiple cells together to better mimic the physiological cellular composition in vivo beside the use of hydrogel scaffolds, or other technologies, to better mimic the 3D environment [169, 170]. The simultaneous study of the effect of a drug to different organs, indeed, may be necessary. Drug metabolism in the liver, for example, can significantly influence renal adverse effects. Certain drugs, such as cyclosporine A and tetra-fluoroethylene, are metabolised by the liver and this can either suppress or enhance nephrotoxicity [171]. Therefore, the construction of organs-on-a-chip leads to the implementation of

body-on-chip models. Multi-organ-chips are reported that support in vitro growth of tissue derived from four different organs with the aim to fully recapitulate human pharmacokinetics [17, 172, 173].

Furthermore, there is a growing interest in exploiting stem cells from patients as the cell source with the purpose of creating a patient-specific body-on-a-chip for drug testing or disease model [169]. On the other hand to do that, it is necessary to increase the quantity of organoids in body-on-a-chip to better mimic the physiological whole-body response to drugs.

Another critical issue is to achieve the vascularization of body-on-a-chip. A step toward this goal is the endothelialization of microchannels [174]. Endothelialized microchannels show better capability to mimic the physiological environment and endocrine function of blood vessels than microchannels only. Finally, it is essential to develop a more user-friendly body-on-a-chip. In fact, various auxiliary devices, such as external pumps and bubble traps, together with the complex preparation process of the system itself, make body-on-a-chip suitable only for skilled researchers. This limits broad utilization of this technology for high-content analysis in the pharmaceutical industry [169].

Bibliography

- [1] D. A., W. B.T., and A. G.L., “Segmental-dependent membrane permeability along the intestine following oral drug administration: Evaluation of a triple single-pass intestinal perfusion (TSPIP) approach in the rat,” *European Journal of Pharmaceutical Sciences*, 2008.
- [2] G. Grootaers, R. Ostendorf, I. Bobeldijk, R. Hanemaaijer, I. Kooter, H. Sandt, and C. Krul, “The 3 dimensions of organ-on-a-chip,” *TNO*, 2016.
- [3] B. Srinivasan, A. Kolli, M. Esch, H. Abaci, M. Shuler, and J. Hickman, “Teer measurement techniques for in vitro barrier model systems,” *European Journal of Pharmaceutical Sciences*, 2008.
- [4] X. Cao, L. X. Yu, C. Barbaciru, C. P. Landowski, H. C. Shin, S. Gibbs, H. A. Miller, G. L. Amidon, and D. Sun, “Permeability dominates in vivo intestinal absorption of p-gp substrate with high solubility and high permeability,” *Mol. Pharm.*, vol. 2, p. 329, 2005.
- [5] D. Sun, L. Yu, M. Hussain, D. Wall, R. Smith, and G. Amidon, “In vitro testing of drug absorption for drug ‘developability’ assessment: forming an interface between invitro preclinical data and clinical outcome,” *Current Opinion in Drug Discovery & Development*, vol. 7, pp. 75–85, 2004.
- [6] C. Zihni, C. Mills, K. Matter, and M. S. Balda, “Tight junctions: from simple barriers to multifunctional molecular gates,” *Nature Reviews Molecular Cell Biology*, vol. 17, pp. 564–580, 2016.
- [7] Zoph, “File:membrantransport.png.” <https://commons.wikimedia.org/wiki/File:Membrantransport.png>. Accessed: 9-May-2017.
- [8] S. G. Massry and R. J. Glassock, *Massry & Glassock’s textbook of nephrology*. Lippincott Williams & Wilkins, 2001.
- [9] P. Medicine, “Urine formation - general mechanistic principles.” <http://www.pathwaymedicine.org/urine-formation-general-mechanistic-principles>. Accessed: 9-June-2017.
- [10] M. B. Nieto, “Tubular transport.” <http://www.acbrown.com/renal/OutTub1.htm>. Accessed: 15-May-2017.
- [11] S. N. Bhatia and D. E. Ingber, “Microfluidic organs-on-chips,” *Nature biotechnology*, vol. 32, no. 8, pp. 760–772, 2014.

-
- [12] B. Obermeier, R. Daneman, and R. M. Ranschoff, "Development, maintenance and disruption of the blood-brain barrier," *Nature medicine*, vol. 19, no. 12, pp. 1584–1596, 2013.
- [13] J. R. Turner, "Intestinal mucosal barrier function in health and disease," *Nature Reviews Immunology*, vol. 9, no. 11, pp. 799–809, 2009.
- [14] J. A. Whitsett and T. Alenghat, "Respiratory epithelial cells orchestrate pulmonary innate immunity," *Nature immunology*, vol. 16, no. 1, pp. 27–35, 2015.
- [15] R. Thuenauer, E. Rodriguez-Boulan, and W. Romer, "Microfluidic approaches for epithelial cell layer culture and characterisation," *Analyst*, vol. 139, no. 13, pp. 3206–3218, 2014.
- [16] D. Huh, G. A. Hamilton, and D. E. Ingber, "From 3d cell culture to organs-on-chips," *Trends in cell biology*, vol. 21, no. 12, pp. 745–754, 2011.
- [17] . W. M. J. Nieskens, T. T., "Kidney-on-a-chip technology for renal proximal tubule tissue reconstruction," *European journal of pharmacology*, no. 790, pp. 46–56, 2016.
- [18] D. Gao, I. Vela, A. Sbone, P. J. Iaquina, W. R. Karthaus, A. Gopalan, and J. Wongvipat, "Organoid cultures derived from patients with advanced prostate cancer," *Cell*, vol. 159, no. 1, pp. 176–187, 2014.
- [19] T. Sodunke, K. Turner, S. Caldwell, K. McBride, and M. Reginato, "Micropatterns of matrigel for three-dimensional epithelial cultures," *Biomaterials*, vol. 28, no. 27, pp. 4006–4016, 2007.
- [20] H. Leblochová, "Transport of ion channel blockers across the blood-brain barrier in vitro," Master's thesis, 2010.
- [21] "Transwell guidelines." <https://www.corning.com/worldwide/en/products/life-sciences/products/permeable-supports/transwell-guidelines.html>. Accessed: 2-June-2017.
- [22] T. M. Keenan and A. Folch, "Biomolecular gradients in cell culture systems," *Lab on Chip*, vol. 8, pp. 34–57, 2008.
- [23] J. H. Sung, M. B. Esch, J. Prot, C. J. Long, A. Smith, J. J. Hickman, and M. L. Shuler, "Microfabricated mammalian organ systems and their integration into models of whole animals and humans," *Lab Chip*, vol. 13, pp. 1201–1212, 2013.
- [24] B. T. Hawkins and T. P. Davis, "The blood-brain barrier/neurovascular unit in health and disease," *Pharmacological reviews*, vol. 57, no. 2, pp. 173–185, 2005.
- [25] B. V. Zlokovic, "Neurodegeneration and the neurovascular unit," *Nature medicine*, vol. 16, no. 12, pp. 1370–1371, 2010.
- [26] M. van der Helm, A. van der Meer, J. Eijkel, A. van den Berg, and L. Segerink, "Microfluidic organ-on-chip technology for blood-brain barrier," *Tissue Barriers*, 2016.

- [27] F. Zheng, F. Fu, Y. Cheng, C. Wang, Y. Zhao, and Z. Gu, “Organ-on-a-chip systems: Microengineering to biomimic living systems,” *Small*, vol. 12, no. 17, pp. 2253–2282, 2016.
- [28] M. Marroni, L. Cucullo, L. Krizanac-Bengez, M. Mayberg, M. Hossain, G. Grant, and D. Janigro, “Mechanisms of endothelial survival under shear stress,” *Endothelium*, vol. 9, pp. 89–102, 2002.
- [29] A. Wong, M. Ye, A. Levy, J. Rothstein, D. Bergles, and P. Searson, “The blood-brain barrier: an engineering perspective,” *Frontiers in neuroengineering*, vol. 6, 2013.
- [30] R. Booth and H. Kim, “Permeability analysis of neuroactive drugs through a dynamic microfluidic in vitro blood-brain barrier model,” *Annals of Biomedical Engineering*, vol. 42, pp. 2379–91, 2014.
- [31] J. Kim, H. Kim, S.-K. Im, S. Chun, J. Kang, and N. Choi, “Collagen-based brain microvasculature model in vitro using three-dimensional printed template,” *Biomicrofluidics*, vol. 9, no. 2, 2015.
- [32] J. Brown, V. Pensabene, D. Markov, V. Allwardt, M. Neel, M. Shi, C. Britt, O. Hoilett, Q. Yang, and B. Brewer, “Recreating blood-brain barrier physiology and structure on chip: A novel neurovascular microfluidic bioreactor,” *Biomicrofluidics*, vol. 9, 2015.
- [33] F. Walter, S. Valkai, A. Kincses, A. Petneházi, T. Czeller, S. Veszeka, P. Ormos, M. Deli, and A. Dér, “A versatile lab-on-a-chip tool for modeling biological barriers,” *Sensors and Actuators B: Chemical*, vol. 222, pp. 1209–1219, 2016.
- [34] M. J. Wilmer, C. P. Ng, H. L. Lanz, P. Vulto, L. Suter-Dick, and R. Masereeuw, “Kidney-on-a-chip technology for drug-induced nephrotoxicity screening,” *Trends in biotechnology*, vol. 34, no. 2, pp. 156–170, 2016.
- [35] E. Weinberg, M. Kaazempur-Mofrad, and J. Borenstein, “Concept and computational design for a bioartificial nephron-on-a-chip,” *International Journal of Artificial Organs*, vol. 31, no. 6, pp. 508–514, 2008.
- [36] M. Schetz, J. Dasta, S. Goldstein, and T. Golper, “Drug-induced acute kidney injury,” *Current opinion in critical care*, vol. 11, no. 6, pp. 555–565, 2005.
- [37] S. S. Sarang, M. D. Plotkin, S. R. Gullans, B. S. Cummings, D. F. Grant, and R. G. Schnellmann, “Identification of the γ -aminobutyric acid receptor β 2 and β 3 subunits in rat, rabbit, and human kidneys,” *Journal of the American Society of Nephrology*, vol. 12, no. 6, pp. 1107–1113, 2001.
- [38] L. C. Snouber, S. Jacques, M. Monge, C. Legallais, and E. Leclerc, “Transcriptomic analysis of the effect of ifosfamide on mdck cells cultivated in microfluidic biochips,” *Genomics*, vol. 100, no. 1, pp. 27–34, 2012.
- [39] T. DesRochers, L. Suter, A. Roth, and D. L. Kaplan, “Bioengineered 3d human kidney tissue, a platform for the determination of nephrotoxicity,” *PLoS ONE*, vol. 8, no. 3, 2013.

-
- [40] K. J. Jang, A. Mehr, G. Hamilton, L. McPartlin, S. Chung, K. Y. Suh, and D. E. Ingber, “Human kidney proximal tubule-on-a-chip for drug transport and nephrotoxicity assessment,” *Integrative Biology*, vol. 5, no. 9, pp. 1119–1129, 2013.
- [41] M. L. Lawrence, C. H. Chang, and J. A. Davies, “Transport of organic anions and cations in murine embryonic kidney development and in serially-reaggregated engineered kidneys,” *Scientific reports*, vol. 5, 2015.
- [42] K. J. Jang and K. Y. Suh, “A multi-layer microfluidic device for efficient culture and analysis of renal tubular cells,” *Lab on a Chip*, vol. 10, no. 1, pp. 36–42, 2010.
- [43] C. Willyard, “Channeling chip power: tissue chips are being put to the test by industry,” *Nature America*, 2017.
- [44] J. Kyung-Jin and S. Kahp-Yang, “A multi-layer microfluidic device for efficient culture and analysis of renal tubular cells,” *Lab Chip*, vol. 10, p. 36–42, 2010.
- [45] E. M. Frohlich, X. Zhang, and J. L. Charest, “The use of controlled surface topography and flow-induced shear stress to influence renal epithelial cell function,” *Integrative Biology*, vol. 4, no. 1, pp. 75–83, 2012.
- [46] M. Griese, R. Essl, R. Schmidt, E. Rietschel, F. Ratjen, M. Ballmann, and K. Paul, “Pulmonary surfactant, lung function, and endobronchial inflammation in cystic fibrosis,” *American journal of respiratory and critical care medicine*, vol. 170, no. 9, pp. 1000–1005, 2004.
- [47] D. Huh, H. Fujioka, Y. Tung, N. Futai, R. Paine, J. Grotberg, and S. Takayama, “Acoustically detectable cellular-level lung injury induced by fluid mechanical stresses in microfluidic airway systems,” *Proceedings of the National Academy of Sciences*, vol. 104, no. 48, pp. 18886–18891, 2007.
- [48] D. Gaver, D. Halpern, O. Jensen, and J. Grotberg, “The steady motion of a semi-infinite bubble through a flexible-walled channel,” *Journal of Fluid Mechanics*, vol. 319, pp. 25–65, 1996.
- [49] A. Miller and J. Spence, “In vitro models to study human lung development, disease and homeostasis,” *Physiology*, vol. 32, no. 3, pp. 246–260, 2017.
- [50] H. Danahay, A. Pessotti, J. Coote, B. Montgomery, D. Xia, A. Wilson, H. Yang, Z. Wang, L. Bevan, C. Thomas, S. Petit, A. London, P. LeMotte, A. Doelemeyer, G. Vélez-Reyers, P. Bernasconi, C. Fryer, M. Edwards, A. Chen, M. Hild, and A. Jaffe, “Notch2 is required for inflammatory cytokine-driven goblet cell metaplasia in the lung,” *Cell Reports*, vol. 10, pp. 239–252, 2015.
- [51] J. Rock, M. Onaitis, E. Rawlins, Y. Lu, C. Clark, Y. Xue, and B. Hogan, “Basal cells as stem cells of the mouse trachea and human airway epithelium,” *Proceedings of the National Academy of Sciences*, vol. 106, no. 31, pp. 12771–12775, 2009.
-

- [52] J. S. Lwebuga-Mukasa, D. H. Ingbar, and J. A. Madri, “Repopulation of a human alveolar matrix by adult rat type ii pneumocytes in vitro: a novel system for type ii pneumocyte culture,” *Experimental cell research*, vol. 162, no. 2, pp. 423–435, 1986.
- [53] H. Ott, B. Clippinger, C. Conrad, C. Schuetz, I. Pomerantseva, L. Ikononou, and J. Vacanti, “Regeneration and orthotopic transplantation of a bioartificial lung,” *Nature medicine*, vol. 16, no. 8, pp. 927–933, 2010.
- [54] T. Petersen, E. Calle, L. Zhao, E. Lee, L. Gui, M. Raredon, and E. Herzog, “Tissue-engineered lungs for in vivo implantation,” *Science*, vol. 329, no. 5991, pp. 538–541, 2010.
- [55] D. Huh, B. Matthews, A. Mammoto, M. Montoya-Zavala, H. Hsin, and D. Ingber, “Reconstituting organ-level lung functions on a chip,” *Science*, vol. 328, no. 5986, pp. 1662–1668, 2010.
- [56] “Lung on a chip, wyss institute.” <http://wyss.harvard.edu/viewpage/240/>, 2010. Accessed: 26-May-2017.
- [57] Y. Lin, W. Chrzanowski, J. Knowles, A. Bishop, and A. Bismarck, “Functionalized poly (d, l-lactide) for pulmonary epithelial cell culture,” *Advanced Engineering Materials*, vol. 12, no. 4, 2010.
- [58] J. Cortiella, J. Nichols, K. Kojima, L. Bonassar, P. Dargon, A. Roy, and C. Vacanti, “Tissue-engineered lung: an in vivo and in vitro comparison of polyglycolic acid and pluronic f-127 hydrogel/somatic lung progenitor cell constructs to support tissue growth,” *Tissue engineering*, vol. 12, no. 5, pp. 1213–1225, 2006.
- [59] A. Doryab, G. Amoabediny, and A. Salehi-Najafabadi, “Advances in pulmonary therapy and drug development: Lung tissue engineering to lung-on-a-chip,” *Biotechnology advances*, vol. 34, no. 5, pp. 588–596, 2016.
- [60] G. Mahler, M. Esch, R. Glahn, and M. L. Shuler, “Characterization of a gastrointestinal tract microscale cell culture analog used to predict drug toxicity,” *Biotechnology and bioengineering*, vol. 104, no. 1, pp. 193–205, 2009.
- [61] E. L. Ferrec, C. Chesne, P. Artusson, D. Brayden, G. Fabre, P. Gires, and M. Scarino, “In vitro models of the intestinal barrier,” *Atla*, vol. 29, pp. 649–668, 2001.
- [62] D. Huh, H. Kim, J. Fraser, D. Shea, M. Khan, A. Bahinski, and D. E. Ingber, “Microfabrication of human organs-on-chips,” *Nature protocols*, vol. 8, no. 11, pp. 2135–2157, 2013.
- [63] H. Shum, Y. Zhao, S. Kim, and D. Weitz, “Multicompartment polymersomes from double emulsions,” *Angewandte Chemie*, vol. 123, no. 7, pp. 1686–1689, 2011.
- [64] H. J. Kim and D. E. Ingber, “Gut-on-a-chip microenvironment induces human intestinal cells to undergo villus differentiation,” *Integrative Biology*, vol. 5, no. 9, pp. 1130–1140, 2013.

-
- [65] N. Saunders, K. Dziegielewska, K. Møllgård, and M. Habgood, “Markers for blood-brain barrier integrity: how appropriate is Evans blue in the twenty-first century and what are the alternatives?,” *Frontiers in neuroscience*, vol. 9, p. 385, 2015.
- [66] Z. Li, Y. H. M. Suzuki, F. Cao, X. Xie, A. J. Connolly, and J. C. Wu, “Comparison of reporter gene and iron particle labeling for tracking fate of human embryonic stem cells and differentiated endothelial cells in living subjects. stem cells and differentiated endothelial cells in living subjects,” *Stem cells*, vol. 26, no. 4, pp. 864–873, 2008.
- [67] S. Franciosi, R. D. Gasperi, D. L. Dickstein, D. F. English, A. B. Rocher, W. G. Janssen, and G. A. Elder, “Pepsin pretreatment allows collagen IV immunostaining of blood vessels in adult mouse brain,” *Journal of neuroscience methods*, vol. 163, no. 1, pp. 76–82, 2007.
- [68] S. Liddelow, K. Dziegielewska, C. Ek, P. Johansson, A. Potter, and N. Saunders, “Cellular transfer of macromolecules across the developing choroid plexus of *Monodelphis domestica*,” *European Journal of Neuroscience*, vol. 29, no. 2, pp. 253–266, 2009.
- [69] E. O’Shea, A. Urrutia, A. Green, and M. Colado, “Current preclinical studies on neuroinflammation and changes in blood-brain barrier integrity by MDMA and methamphetamine,” *Neuropharmacology*, vol. 87, pp. 125–134, 2014.
- [70] L. Blair, H. Frauen, B. Zhang, B. Nordhues, S. Bijan, Y. Lin, and C. Dickey, “Tau depletion prevents progressive blood-brain barrier damage in a mouse model of tauopathy,” *Acta neuropathologica communications*, vol. 3, no. 1, p. 8, 2015.
- [71] M. D. Habgood, N. Bye, K. M. Dziegielewska, C. J. Ek, M. A. Lane, A. Potter, and N. R. Saunders, “Changes in blood-brain barrier permeability to large and small molecules following traumatic brain injury in mice,” *European Journal of Neuroscience*, vol. 25, no. 1, pp. 231–238, 2007.
- [72] N. C. Veitch, “Horseradish peroxidase: a modern view of a classic enzyme,” *Phytochemistry*, vol. 65, no. 3, pp. 249–259, 2004.
- [73] J. A. Akkara, K. J. Senecal, and D. L. Kaplan, “Synthesis and characterization of polymers produced by horseradish peroxidase in dioxane,” *Journal of Polymer Science*, vol. 29, no. 11, p. 1561–1574, 1991.
- [74] S. Miyata and S. Morita, “A new method for visualization of endothelial cells and extravascular leakage in adult mouse brain using fluorescein isothiocyanate,” *Journal of neuroscience methods*, vol. 202, no. 1, pp. 9–16, 2011.
- [75] T. Rieg, “A high-throughput method for measurement of glomerular filtration rate in conscious mice,” *JoVE (Journal of Visualized Experiments)*, vol. 75, pp. e50330–e50330, 2013.
-

- [76] N. Ferrell, R. R. Desai, A. J. Fleischman, S. Roy, H. D. Humes, and W. H. Fissell, "A microfluidic bioreactor with integrated transepithelial electrical resistance (TEER) measurement electrodes for evaluation of renal epithelial cells," *Biotechnology and bioengineering*, vol. 107, no. 4, pp. 707–716, 2010.
- [77] N. J. Douville, Y. C. Tung, R. Li, J. D. Wang, M. E. El-Sayed, and S. Takayama, "Fabrication of two-layered channel system with embedded electrodes to measure resistance across epithelial and endothelial barriers," *Analytical chemistry*, vol. 82, no. 6, p. 25, 2010.
- [78] J. Hwang, Y. Jeong, J. M. Park, K. H. Lee, J. W. Hong, and J. Choi, "Biomimetics: forecasting the future of science, engineering, and medicine," *International journal of nanomedicine*, vol. 10, p. 5701, 2015.
- [79] M. Webber, E. Appel, E. Meijer, and R. Langer, "Supramolecular biomaterials," *Nature materials*, vol. 15, no. 1, pp. 13–26, 2015.
- [80] T. U. Luu, S. C. Gott, B. W. Woo, M. P. Rao, and W. F. Liu, "Micro-and nanopatterned topographical cues for regulating macrophage cell shape and phenotype," *ACS applied materials & interfaces*, vol. 7, no. 51, pp. 28665–28672, 2015.
- [81] H. Zhang, E. Burdet, A. N. Poo, and D. W. Hutmacher, "Microassembly fabrication of tissue engineering scaffolds with customized design," *IEEE Transactions on Automation Science and Engineering*, vol. 5, no. 3, pp. 446–456, 2008.
- [82] T. Limongi, L. Tirinato, F. Pagliari, A. Giugni, M. Allione, G. Perozziello, and E. D. Fabrizio, "Fabrication and applications of micro/nanostructured devices for tissue engineering," *Nano-Micro Letters*, vol. 9, no. 1, p. 1, 2017.
- [83] D. W. Hutmacher, J. T. Schantz, C. X. F. Lam, K. C. Tan, and T. C. Lim, "State of the art and future directions of scaffold-based bone engineering from a biomaterials perspective," *Journal of tissue engineering and regenerative medicine*, vol. 1, no. 4, pp. 245–260, 2007.
- [84] F. Khan, M. Tanaka, and S. R. Ahmad, "Fabrication of polymeric biomaterials: a strategy for tissue engineering and medical devices," *Journal of Materials Chemistry B*, vol. 3, no. 42, pp. 8224–8249, 2015.
- [85] G. B. Roth, "Matrix repatterning: The structural basis of health." www.rothinstitute.com/pro/SubPages/matrixrepat.html. Accessed: 20-May-2017.
- [86] V. Raffa, O. Vittorio, V. Pensabene, A. Menciassi, and P. Dario, "Fib-nanostructured surfaces and investigation of bio/nonbio interactions at the nanoscale," *IEEE transactions on nanobioscience*, vol. 7, no. 1, pp. 1–10, 2008.
- [87] F. D. Angelis, C. Liberale, M. L. Coluccio, G. Cojoc, and E. D. Fabrizio, "Emerging fabrication techniques for 3d nano-structuring in plasmonics and single molecule studies," *Nanoscale*, vol. 3, no. 7, pp. 2689–2696, 2011.

-
- [88] A. R. Jung, R. Y. Kim, H. W. Kim, K. R. Shrestha, S. H. Jeon, K. J. Cha, and J. Y. Lee, "Nanoengineered polystyrene surfaces with nanopore array pattern alters cytoskeleton organization and enhances induction of neural differentiation of human adipose-derived stem cells," *Tissue Engineering Part A*, vol. 21, no. 13-14, pp. 2115–2124, 2015.
- [89] A. A. Chen, V. L. Tsang, D. R. Albrecht, and S. N. Bhatia, "3-d fabrication technology for tissue engineering," *BioMEMS and Biomedical Nanotechnology*, pp. 23–38, 2006.
- [90] S. Yang, K. F. Leong, Z. Du, and C. K. Chua, "The design of scaffolds for use in tissue engineering: part ii. rapid prototyping techniques," *Tissue Engineering*, vol. 7, pp. 1–11, 2002.
- [91] J. H. Kim, J. W. Lee, and W. S. Yun, "Fabrication and tissue engineering application of a 3d ppf/def scaffold using blu-ray based 3d printing system," *Journal of Mechanical Science and Technology*, vol. 31, no. 5, pp. 2581–2587, 2017.
- [92] I. Zein, D. W. Hutmacher, K. C. Tan, and S. H. Teoh, "Fused deposition modeling of novel scaffold architectures for tissue engineering applications," *Biomaterials*, vol. 23, no. 4, pp. 1169–1185, 2002.
- [93] D. W. Hutmacher, M. Sittinger, and M. Risbud, "Scaffold design and fabrication technologies for engineering tissues-state of the art and future perspectives," *Journal of Biomaterials Science, Polymer Edition*, vol. 12, no. 1, pp. 107–124, 2001.
- [94] M. Endres, D. W. Hutmacher, A. J. Salgado, C. Kaps, J. Ringe, R. L. Reis, and J. T. Schantz, "Osteogenic induction of human bone marrow-derived mesenchymal progenitor cells in novel synthetic polymer-hydrogel matrices," *Tissue engineering*, vol. 9, no. 4, pp. 689–702, 2003.
- [95] T. B. Woodfield, J. Malda, J. D. Wijn, F. Peters, J. Riesle, and C. A. van Blitterswijk, "Design of porous scaffolds for cartilage tissue engineering using a three-dimensional fiber-deposition technique," *Biomaterials*, vol. 28, no. 15, pp. 4149–4161, 2004.
- [96] J. S. Miller, K. R. Stevens, M. T. Yang, B. M. Baker, D. H. T. Nguyen, D. M. Cohen, and R. Chaturvedi, "Rapid casting of patterned vascular networks for perfusable engineered three-dimensional tissues," *Nature materials*, vol. 11, no. 9, pp. 768–774, 2012.
- [97] A. Justin, R. Brooks, and A. Markaki, "Multi-casting approach for vascular networks in cellularized hydrogels," *Journal of The Royal Society Interface*, vol. 13, no. 125, 2016.
- [98] S. Li, Y. Y. Liu, L. J. Liu, and Q. X. Hu, "A versatile method for fabricating tissue engineering scaffolds with a three-dimensional channel for pre-vascularization networks," *ACS Applied Materials & Interfaces*, vol. 8, no. 38, pp. 25096–25103, 2016.
-

- [99] A. Tocchio, M. Tamplenizza, F. Martello, E. R. I. Gerges, S. Argentiére, and C. Lenardi, “Versatile fabrication of vascularizable scaffolds for large tissue engineering in bioreactor,” *Biomaterials*, vol. 45, pp. 124–131, 2015.
- [100] X. Y. Wang, Z. H. Jin, B. W. Gan, S. W. Lv, M. Xie, and W. H. Huang, “Engineering interconnected 3d vascular networks in hydrogels using molded sodium alginate lattice as the sacrificial template,” *Lab on a Chip*, vol. 14, no. 15, pp. 2709–2716, 2014.
- [101] L. E. Bertassoni, M. Cecconi, V. Manoharan, M. Nikkhah, J. Hjortnaes, A. L. Cristino, G. Barabaschi, D. Demarchi, M. R. Dokmeci, Y. Yang, and A. Khademhosseini, “Hydrogel bioprinted microchannel networks for vascularization of tissue engineering constructs,” *Lab. Chip*, vol. 14, pp. 2202–2211, 2014.
- [102] H. Chan, Q. Tian, Y. Shu, and H. Wu, “Replicating 3d printed structures into hydrogels,” *Material Horizons*, vol. 3, pp. 132–134, 2015.
- [103] T. Y. Kang, J. M. Hong, J. W. Jung, H. W. Kang, and D. W. Cho, “Construction of large-volume tissue mimics with 3d functional vascular networks,” *PloS one*, vol. 11, no. 5, 2016.
- [104] R. Pimentel, *Vascularization of Soft Tissue Engineering Constructs*. PhD dissertation, Technical University of Denmark (DTU), 2011.
- [105] S. Lohfeld and P. E. McHugh, “Laser sintering for the fabrication of tissue engineering scaffolds,” *Computer-Aided Tissue Engineering*, pp. 303–310, 2012.
- [106] C. M. Langton, M. A. Whitehead, D. K. Langton, and G. Langley, “Development of a cancellous bone structural model by stereolithography for ultrasound characterisation of the calcaneus,” *Medical engineering & physics*, vol. 19, no. 7, pp. 599–604, 1997.
- [107] D. Duane, S. C. Danforth, and M. J. Cima, “Solid freeform and additive fabrication,” *Biotechnology and bioengineering*, vol. 104, 1999.
- [108] O. A. Abdelaal and S. M. Darwish, “Fabrication of tissue engineering scaffolds using rapid prototyping techniques,” *World Academy of Science, Engineering and Technology, International Journal of Mechanical, Aerospace, Industrial, Mechatronic and Manufacturing Engineering*, vol. 5, no. 11, pp. 2317–2325, 2011.
- [109] K. Ikuta and S. Maruo, “Submicron stereolithography for the production of freely movable mechanisms by using single-photon polymerization,” *Sensor. Actuat. A-Phys.*, vol. 100, pp. 70–76, 2002.
- [110] F. P. Melchels, J. Feijen, and D. W. Grijpma, “A review on stereolithography and its applications in biomedical engineering,” *Biomaterials*, vol. 31, pp. 6121–6130, 2010.
- [111] J. W. Lee, G. Ahn, J. Y. Kim, and D. W. Cho, “Evaluating cell proliferation based on internal pore size and 3d scaffold architecture fabricated using solid

- freeform fabrication technology,” *Journal of Materials Science: Materials in Medicine*, vol. 21, no. 12, pp. 3195–3205, 2010.
- [112] J. W. Lee, G. Ahn, D. S. Kim, and D. W. Cho, “Development of nano-and microscale composite 3d scaffolds using ppf/def-ha and micro-stereolithography,” *Microelectronic Engineering*, vol. 86, no. 4, pp. 1465–1467, 2009.
- [113] N. E. Sanjana and S. B. Fuller, “A fast flexible ink-jet printing method for patterning dissociated neurons in culture,” *Journal of neuroscience methods*, vol. 136, no. 2, pp. 151–163, 2004.
- [114] D. Therriault, S. R. White, and J. A. Lewis, “Chaotic mixing in three-dimensional microvascular networks fabricated by direct-write assembly,” *Nature materials*, vol. 2, no. 4, pp. 265–271, 2003.
- [115] S. J. Eichhorn, “Cellulose nanowhiskers: promising materials for advanced applications,” *Soft Matter*, vol. 7, no. 2, pp. 303–315, 2011.
- [116] J. Araki, “Electrostatic or steric?-preparations and characterizations of well-dispersed systems containing rod-like nanowhiskers of crystalline polysaccharides,” *Soft Matter*, vol. 9, no. 16, pp. 4125–4141, 2013.
- [117] Y. Ito, “Covalently immobilized biosignal molecule materials for tissue engineering,” *Soft matter*, vol. 4, no. 1, pp. 46–56, 2008.
- [118] S. Suzuki and Y. Teramoto, “A simple inkjet process to fabricate microstructures of chitinous nanocrystals for cell patterning,” *Biomacromolecules*, 2017.
- [119] D. B. Kolesky, R. L. Truby, A. Gladman, T. A. Busbee, K. A. Homan, and J. A. Lewis, “3d bioprinting of vascularized, heterogeneous cell-laden tissue constructs,” *Advanced Materials*, vol. 26, pp. 3124–3130, 2014.
- [120] V. K. Lee, D. Y. Kim, H. Ngo, Y. Lee, L. Seo, S. S. Yoo, and G. Dai, “Creating perfused functional vascular channels using 3d bio-printing technology,” *Biomaterials*, vol. 35, pp. 8092–8102, 2014.
- [121] S. V. Murphy and A. Atala, “3d bioprinting of tissues and organs,” *Biotechnology and bioengineering*, vol. 32, pp. 773–785, 2014.
- [122] J. H. Chung, S. Naficy, Z. Yue, R. Kapsa, S. E. M. A. Quigley, and G. G. Wallace, “Bio-ink properties and printability for extrusion printing living cells,” *Biomaterials Science*, vol. 1, no. 7, pp. 763–773, 2013.
- [123] C. B. Highley, C. B. Rodell, and J. A. Burdick, “Direct 3d printing of shear-thinning hydrogels into self-healing hydrogels,” *Advanced Materials*, vol. 27, no. 34, pp. 5075–5079, 2015.
- [124] T. J. Hinton, Q. Jallerat, R. N. Palchesko, J. H. Park, M. S. Grodzicki, H. J. Shue, and A. W. Feinberg, “Three-dimensional printing of complex biological structures by freeform reversible embedding of suspended hydrogels,” *Science advances*, vol. 1, no. 9, 2015.

- [125] Y. S. Zhang, K. Yue, J. Aleman, K. Mollazadeh-Moghaddam, S. M. Bakht, J. Yang, and M. R. Dokmeci, “3d bioprinting for tissue and organ fabrication,” *Annals of biomedical engineering*, vol. 45, no. 1, pp. 797–803, 2017.
- [126] I. T. Ozbolat, “Bioprinting scale-up tissue and organ constructs for transplantation,” *Trends in biotechnology*, vol. 33, no. 7, pp. 148–163, 2015.
- [127] C. Mandrycky, K. K. Z. Wang, and D. H. Kim, “3d bioprinting for engineering complex tissues,” *Biotechnology advances*, vol. 34, no. 4, pp. 422–434, 2016.
- [128] W. Jia, P. S. Gungor-Ozkerim, Y. S. Zhang, K. Yue, K. Zhu, W. Liu, and A. Khademhosseini, “Direct 3d bioprinting of perfusable vascular constructs using a blend bioink,” *Biomaterials*, vol. 106, pp. 58–68, 2016.
- [129] H. W. Kang, S. J. Lee, I. K. Ko, C. Kengla, J. J. Yoo, and A. Atala, “A 3d bioprinting system to produce human-scale tissue constructs with structural integrity,” *Nature biotechnology*, vol. 34, no. 3, pp. 312–310, 2016.
- [130] T. Xu, J. Jin, C. Gregory, J. J. Hickman, and T. Boland, “Inkjet printing of viable mammalian cells,” *Biomaterials*, vol. 26, no. 1, pp. 93–99, 2005.
- [131] B. D. Gates, Q. Xu, M. Stewart, D. Ryan, C. G. Willson, and G. M. Whitesides, “New approaches to nanofabrication: molding, printing, and other techniques,” *Chemical reviews*, vol. 109, no. 2, pp. 1171–1196, 2005.
- [132] J. Love, B. Daniel, and M. George, *Dekker Encyclopedia of Nanoscience and Nanotechnology-Six Volume Set*. CRC Press, 2004. (Print Version).
- [133] C. Bettinger, K. Cyr, A. Matsumoto, J. B. R. Langer, and D. Kaplan, “Silk fibroin microfluidic devices,” *Advanced Materials*, vol. 19, no. 5, pp. 2847–2850, 2007.
- [134] F. Cesca, T. Limongi, A. Accardo, A. Rocchi, M. Orlando, V. Shalabaeva, E. D. Fabrizio, and F. Benfenati, “Fabrication of biocompatible free-standing nanopatterned films for primary neuronal cultures,” *RSC Adv.*, vol. 4, no. 86, pp. 45696–45702, 2014.
- [135] T. M. Chu, J. S. Hollister, J. W. Halloran, S. E. Feinberg, and D. G. Orton, “Manufacturing and characterization of 3-d hydroxyapatite bone tissue engineering scaffolds,” *Annals of the New York Academy of Sciences*, vol. 961, no. 1, pp. 114–117, 2002.
- [136] T. M. Chu, D. G. Orton, J. S. Hollister, S. E. Feinberg, and J. W. Halloran, “Mechanical and in vivo performance of hydroxyapatite implants with controlled architectures,” *Biomaterials*, vol. 23, no. 5, pp. 1283–1293, 2002.
- [137] J. M. Taboas, R. D. Maddox, P. H. Krebsbach, and S. J. Hollister, “Indirect solid free form fabrication of local and global porous, biomimetic and composite 3d polymer-ceramic scaffolds,” *Biomaterials*, vol. 24, no. 1, pp. 181–194, 2003.

-
- [138] V. Mironov, T. Boland, T. Trusk, G. Forgacs, and R. R. Markwald, "Organ printing: computer-aided jet-based 3d tissue engineering," *TRENDS in Biotechnology*, vol. 21, no. 4, pp. 157–161, 2003.
- [139] J. B. Lee, X. Wang, S. Faley, B. Baer, D. A. Balikov, H. J. Sung, and L. M. Bellan, "Development of 3d microvascular networks within gelatin hydrogels using thermoresponsive sacrificial microfibers," *Advanced healthcare materials*, 2016.
- [140] W. G. Koh, A. Revzin, and M. V. Pishko, "Poly (ethylene glycol) hydrogel microstructures encapsulating living cells," *Langmuir*, vol. 18, no. 7, pp. 2459–2462, 2002.
- [141] D. R. Albrecht, V. L. Tsang, R. L. Sah, and S. N. Bhatia, "Photo-and electropatterning of hydrogel-encapsulated living cell arrays," *Lab on a Chip*, vol. 5, no. 1, pp. 111–118, 2005.
- [142] K. T. Nguyen and J. L. West, "Photopolymerizable hydrogels for tissue engineering applications," *Biomaterials*, vol. 23, no. 22, pp. 4307–4314, 2002.
- [143] J. A. Stolwijk, K. Matrougui, C. W. Renken, and M. Trebak, "Impedance analysis of gpcr-mediated changes in endothelial barrier function: overview and fundamental considerations for stable and reproducible measurements," *Pflügers Archiv-European Journal of Physiology*, vol. 467, no. 10, pp. 2193–2218, 2015.
- [144] M. Odijk, A. D. van der Meer, D. Levner, H. J. Kim, M. W. van der Helm, L. I. Segerink, J.-P. Frimat, G. A. Hamilton, D. E. Ingber, and A. van den Berga, "Measuring direct current trans-epithelial electrical resistance in organ-on-a-chip microsystems," *Lab on a Chip*, vol. 15, no. 3, pp. 745–752, 2014.
- [145] K. Benson, S. Cramer, and H.-J. Galla, "Impedance-based cell monitoring: barrier properties and beyond," *Fluids and Barriers of the CNS*, vol. 10, no. 1, p. 5, 2013.
- [146] S. Yee, "In vitro permeability across caco-2 cells (colonic) can predict in vivo (small intestinal) absorption in man-fact or myth," *Pharmaceutical research*, vol. 14, no. 6, pp. 763–766, 1997.
- [147] S. Grimnes and O. Martinsen, "Bioimpedance and bioelectricity basics," *Bioimpedance and Bioelectricity Basics.*, 2008.
- [148] "Units of enzyme activity," *Eur. J. Biochem.*, vol. 97, no. 2, p. 319–20, 1979.
- [149] "Kisslicer." www.kisslicer.com. Accessed: May-2017.
- [150] "Repetier-host." <https://www.repetier.com>. Accessed: May-2017.
- [151] D. Giavarina, "Understanding bland altman analysis," *Biochemia medica*, vol. 25, no. 2, pp. 141–151, 2015.
- [152] M. Morel, J. C. Galas, M. Dahan, and V. Studer, "Concentration landscape generators for shear free dynamic chemical stimulation," *Lab Chip*, vol. 12, no. 7, pp. 1340–1346, 2012.
-

- [153] J. Y. Park, S. K. Kim, D. H. Woo, E. J. Lee, J. H. Kim, and S. H. Lee, “Differentiation of neural progenitor cells in a microfluidic chip-generated cytokine gradient,” *Stem cells*, vol. 27, no. 11, pp. 2646–2654, 2010.
- [154] B. Mosadegh, W. Saadi, S. J. Wang, and N. L. Jeon, “Epidermal growth factor promotes breast cancer cell chemotaxis in cxcl12 gradients,” *Biotechnology and bioengineering*, vol. 100, no. 6, pp. 1205–1213, 2008.
- [155] S. Nandagopal, D. Wu, and F. Lin, “Combinatorial guidance by ccr7 ligands for t lymphocytes migration in co-existing chemokine fields,” *PLoS One*, vol. 6, no. 3, 2011.
- [156] Physics, “Shape of the ”flow head” in Laminar flow in pipe.” <https://physics.stackexchange.com/questions/98608/shape-of-the-flow-head-in-laminar-flow-in-pipe>. [Online; accessed 02-June-2017].
- [157] A. G. Toh, Z. P. Wang, C. Yang, and N. T. Nguyen, “Engineering microfluidic concentration gradient generators for biological applications,” *Microfluidics and nanofluidics*, vol. 16, no. 1-2, pp. 1–18, 2014.
- [158] M. Autolab, “User Manual of NOVA 2.1.2.” http://www.ecochemie.nl/download/NovaSoftware/NOVA_2.1.2_User_Manual.pdf. [Online; accessed 04-April-2017].
- [159] A. A. Akhtar, S. Sances, R. Barrett, and J. J. Breunig, “Organoid and organ-on-a-chip systems: New paradigms for modeling neurological and gastrointestinal disease,” *Current Stem Cell Reports*, vol. 3, no. 2, pp. 98–111, 2017.
- [160] J. Fogh and G. Trempe, *Human tumor cells in vitro*. 1975.
- [161] M. Pinto, S. Robineleon, and M. Appay, “Enterocyte-like differentiation and polarization of the human colon carcinoma cell line caco-2 in culture,” *Biol Cell.*, vol. 47, pp. 323–330, 1983.
- [162] I. J. Hidalgo, I. J., T. J. Raub, and R. T. Borchardt, “Characterization of the human colon carcinoma cell line (caco-2) as a model system for intestinal epithelial permeability,” *Gastroenterology*, vol. 96, no. 3, pp. 736–749, 1989.
- [163] M. Natoli, B. D. Leoni, I. D’Agnano, F. Zucco, and A. Felsani, “Good caco-2 cell culture practices,” *Toxicology in Vitro*, vol. 26, no. 8, pp. 1243–1246, 2012.
- [164] Y. Sambuy, I. D. Angelis, G. Ranaldi, M. L. Scarino, A. Stamatii, and F. Zucco, “The caco-2 cell line as a model of the intestinal barrier: influence of cell and culture-related factors on caco-2 cell functional characteristics,” *Cell biology and toxicology*, vol. 21, no. 1, pp. 1–26, 2005.
- [165] P. Artursson, “Epithelial transport of drugs in cell culture. i: A model for studying the passive diffusion of drugs over intestinal absorptive (caco-2) cells,” *Journal of pharmaceutical sciences*, vol. 79, no. 6, pp. 476–482, 1990.

- [166] P. Artursson and J. Karlsson, "Correlation between oral drug absorption in humans and apparent drug permeability coefficients in human intestinal epithelial (caco-2) cells," *Biochemical and biophysical research communications*, vol. 175, no. 3, pp. 880–885, 1991.
- [167] D. Discher, D. Mooney, and P. Zandstra, "Growth factors, matrices, and forces combine and control stem cells," *Science*, vol. 324, pp. 1673–1677, 2009.
- [168] T. F. S. Logo, "Phalloidin Conjugates For Staining Actin." <https://www.thermofisher.com/dk/en/home/life-science/cell-analysis/cell-structure/cytoskeleton/phalloidin-and-phalloidin-conjugates-for-staining-actin.html>. [Online; accessed 11-May-2017].
- [169] H. Jin and Y. Yu, "A review of the application of body-on-a-chip for drug test and its latest trend of incorporating barrier tissue," *Journal of laboratory automation*, vol. 21, no. 5, pp. 615–624, 2016.
- [170] S. Breslin and L. O'Driscoll, "Three-dimensional cell culture: The missing link in drug discovery," *Drug Discov. Today*, vol. 18, no. 5-6, pp. 240–249, 2013.
- [171] J. Odum and T. Green, "The metabolism and nephrotoxicity of tetrafluoroethylene in the rat," *Toxicology and Applied Pharmacology*, vol. 76, pp. 306–318, 1984.
- [172] I. Maschmeyer, A. K. Lorenz, K. Schimek, T. Hasenberg, A. P. Ramme, J. Hubner, M. Lindner, C. Drewell, S. Bauer, A. Thomas, N. S. Sambo, F. Sonntag, R. Lauster, and U. Marx, "A four-organ-chip for interconnected long-term co-culture of human intestine, liver, skin and kidney equivalents," *Lab Chip*, vol. 15, pp. 2688–2699, 2015.
- [173] C. Zhang, Z. Zhao, N. A. Rahim, A. van D.Noort, and H. Yu, "Towards a human-on-chip: culturing multiple cell types on a chip with compartmentalized microenvironments," *Lab Chip*, vol. 9, pp. 3185–3192, 2009.
- [174] K. Schimek, M. Busek, S. Brincker, B. Groth, S. Hoffmann, R. Lauster, and H. Walles, "Integrating biological vasculature into a multi-organ-chip microsystem," *Lab on a Chip*, vol. 13, no. 18, pp. 3588–3598, 2013.